Thermohaline feedbacks
in ocean-climate models of varying complexity

Matthijs den Toom

Thermohaline feedbacks
in ocean-climate models of varying complexity

Thermohaliene terugkoppelingsprocessen
in oceaanmodellen van verschillende complexiteit

(met een samenvatting in het Nederlands)

PROEFSCHRIFT

ter verkrijging van de graad van doctor aan de Universiteit Utrecht
op gezag van de rector magnificus, prof. dr. G. J. van der Zwaan,
ingevolge het besluit van het college voor promoties
in het openbaar te verdedigen op

woensdag 20 maart 2013 des middags te 12.45 uur

door

Matthijs den Toom

geboren op 26 juli 1984 te Ridderkerk

Promotor: Prof. dr. ir. H. A. Dijkstra

Contents

Samenvatting

Het woord "klimaat" is afgeleid van een oud-Grieks woord dat "helling" of "regio" betekent. De oorsprong van de term stemt dus overeen met de meest gangbare definitie van klimaat als het gemiddelde weer in een bepaald gebied. Sinds de opkomst van de westerse wetenschap is evenwel steeds duidelijker geworden dat het klimaat niet alleen verschilt per locatie, maar ook varieert in de tijd. Een tot de verbeelding sprekend voorbeeld van klimaatvariabiliteit is de afwisseling van ijstijden en warmere periodes. Een ander bekend terugkerend klimatologisch fenomeen is El-Niño, waardoor het zeewater voor de kust van Peru elke 3 tot 7 jaar abnormaal warm wordt. Anders dan bij bijvoorbeeld seizoensvariaties, die direct te relateren zijn aan veranderingen in de hoeveelheid zonlicht die op een bepaalde plek op aarde valt, is voor de meeste klimaatschommelingen de oorzaak niet direct terug te voeren op veranderingen in externe factoren. In de meeste gevallen liggen interne terugkoppelingsprocessen aan de basis van de variaties: het klimaat is een niet-lineair systeem.

Dit proefschrift gaat in op het niet-lineaire gedrag van de grootschalige circulatie in de oceaan. Het gaat hier om het circulatiepatroon waardoor de verschillende bekkens aan het oppervlak en op grotere diepte als een soort lopende band met elkaar verbonden zijn. Om dit patroon in modellen en observaties te identificeren wordt het begrip meridionale "over-turning"[#] circulatie (MOC) gebruikt. De MOC wordt per bekken bepaald door uit te rekenen hoeveel water er boven een bepaalde diepte naar het noorden stroomt. De Atlantische Oceaan kenmerkt zich door de merkwaardige situatie dat zowel op het noordelijk als op het zuidelijk halfrond water tussen de oppervlakte en een diepte van ongeveer 1 km gemiddeld naar het noorden stroomt. De Atlantische MOC is dus asymmetrisch ten opzichte van de evenaar. In totaal bedraagt het transport boven 1 km diepte zo'n 20 miljoen kubieke meter per seconde. In de noordelijke delen van het bekken het water naar beneden, zodat er een even groot netto transport naar het zuiden is in het gedeelte tussen 1 km diepte en de bodem. De terugkeer van het water naar de bovenlaag vindt plaats in de Zuidelijke Oceaan en in de Stille Oceaan.

Aangezien oceaanwater aan het oppervlak warmer is dan op diepte, is de Atlantische MOC verantwoordelijk voor transport van energie (warmte). Dit transport is van dezelfde orde van grootte als het transport door de atmosfeer en draagt indirect bij aan het relatief milde klimaat van west Europa. De MOC is dus een belangrijke speler in het klimaatsysteem.

Eenvoudige, conceptuele modellen geven echter aan, dat dit mogelijk niet de enige verschijningsvorm van de Atlantische MOC is. In deze modellen komt de huidige toestand overeen met een sterke MOC en bestaat er daarnaast een stabiele toestand met een zwakke, omgekeerde MOC, waarbij het transport van energie veel geringer is. Dergelijke meervoudige evenwichten zouden het gevolg zijn van een wisselwerking die de zout-advectie-

---

[#]Voor deze Engelse term is geen adequate Nederlandse vertaling beschikbaar. In het vervolg van deze tekst wordt de afkorting MOC aangehouden.

terugkoppeling genoemd wordt. Een cruciale aanname die hierbij gemaakt wordt, is dat de Atlantische MOC wordt aangedreven doordat water in het noorden en in het zuiden van het bekken een verschillende dichtheid heeft. Als het water in het noorden een hogere dichtheid heeft dan dat in het zuiden, resulteert dit in een sterke MOC, zoals in het huidige klimaat het geval is. Is het verschil in dichtheid omgekeerd, dan is de MOC zwak en omgekeerd. Het verschil in dichtheid is evenwel niet onafhankelijk van de MOC. Een sterke MOC transporteert zout water uit de subtropen naar het noorden en draagt zo bij aan het creëren van een hoge dichtheid in het noorden. Andersom zorgt een zwakke, omgekeerde MOC voor een lagere dichtheid in het noorden. Overigens heeft de sterkte van de MOC niet alleen invloed op het zoutgehalte in het noorden en het zuiden, maar ook op de temperatuur. Deze invloed is echter veel kleiner, doordat warmte-uitwisseling met de atmosfeer grote temperatuurvariaties onmogelijk maakt. Warmer water verliest immers meer warmte, terwijl zouter water niet per sé meer neerslag ontvangt.

Een mogelijk gevolg van het bestaan van meervoudige evenwichten is het optreden van sterke, abrupte veranderingen in de intensiteit van de Atlantische MOC. Stel bijvoorbeeld dat de huidige, sterke MOC door een willekeurige oorzaak wordt afgezwakt. Als gevolg daarvan zou er minder zout naar het noorden getransporteerd worden. Hierdoor zou de dichtheid in het noorden afnemen en zwakt de MOC verder af. Deze wisselwerking zou in een periode van enkele tientallen jaren leiden tot een transitie van een toestand met een sterke MOC naar een toestand met een zwakke MOC. Het is vanzelfsprekend van belang te weten of dit proces ook in het echte klimaatsysteem een rol speelt. Indirecte observaties van de temperatuur op Groenland en Antarctica gedurende de laatste ijstijd laten variaties zien die consistent zijn met abrupte veranderingen van de Atlantische MOC. Maar voor die variaties zijn ook andere oorzaken te bedenken. Er zijn bovendien geen directe observaties van de sterkte van de MOC die sluitend bewijs leveren, dat de MOC abrupte veranderingen kan ondergaan. Dit betekent het fenomeen alleen met numerieke modellen nader onderzocht kan worden.

Een van de grootste problemen in de oceanografie is, dat bij het opstellen van een numeriek model een groot deel van de te modelleren processen vereenvoudigd moet worden weergegeven. Zo moeten alle processen die op een kleinere schaal spelen dan de roosterafstand van het model, geparametriseerd worden. Daarbij wordt de roosterafstand vaak bepaald door de beschikbare hoeveelheid rekentijd; hoe fijner het grid, hoe meer rekentijd nodig is. Ook ten aanzien van de uitwisseling van impuls, warmte en zoet water met de atmosfeer en zee-ijs moeten aannames gemaakt worden om te voorkomen dat het model te veelomvattend (en dus te rekenintensief) wordt. Om toch vertrouwen te putten uit de resultaten van numerieke modellen, moet daarom onderzocht worden wat de consequenties zijn van het aanbrengen van dergelijke vereenvoudigingen. In dit proefschrift wordt van vier aspecten die met de complexiteit van een oceaanmodel samenhangen, bestudeerd hoe ze van invloed zijn op de simulatie van het niet-lineaire gedrag van de MOC.

Een krachtige methodiek voor het bestuderen van niet-lineaire problemen is numerieke bifurcatieanalyse. Hiermee is het mogelijk van een model de evenwichtstoestanden uit te rekenen als functie van een parameter. Meervoudige evenwichten kunnen zo op een efficiënte manier worden aangetoond. Op het Instituut voor Marien en Atmosferisch Onderzoek Utrecht (IMAU) is een oceaanmodel ontwikkeld waarin deze methodiek is geïmplementeerd. Deze code wordt het ThermoHaliene Circulatie Model (THCM) genoemd. Bij het werk dat in hoofdstukken 2, 3 en 4 gepresenteerd wordt, is gebruikgemaakt van THCM.

Hoofdstuk 2 gaat in op de representatie van processen die tot diffusie van temperatuur- en saliniteitsgradiënten leiden. In de oceaan verlopen dergelijke mengprocessen bijzonder efficiënt langs vlakken van gelijke dichtheid (isopycnen), maar relatief moeizaam in de richting loodrecht (diapycnisch) daarop. Dit wordt tot uitdrukking gebracht in het gebruik van twee verschillende mengcoëfficiënten, een isopycnische en een diapycnische diffusiviteit. De laatste is mogelijk van belang voor de sterkte van de MOC. Door aan te nemen dat temperatuur- en zouttransport door de MOC in evenwicht zijn met diapycnische menging, kan de zogenaamde "klassieke" schalingsrelatie worden afgeleid. Deze houdt in dat de sterkte van de MOC evenredig is met de diapycnische diffusiviteit tot de macht 2/3. De relatie geeft bovendien aan dat de MOC met het noord-zuid dichtheidsverschil tot de macht 1/3 schaalt. Dit ondersteunt dus de aanname die voor het zout-advectie-terugkoppelingsmechanisme gemaakt wordt, zoals hierboven besproken is.

De aanleiding voor het werk in hoofdstuk 2 is het resultaat van een tweetal studies, waaruit blijkt dat de schaling van de MOC verschillend is voor de Atlantische Oceaan en de Stille Oceaan. De suggestie die gewekt wordt, is dat de klassieke schaling alleen van belang is voor de Stille Oceaan. Bij de studie waaruit dit resultaat het meest overtuigend naar voren komt, is gebruik gemaakt van THCM. Een probleem van THCM is echter dat het model het verschil tussen (sterke) isopycnische en (zwakke) diapycnische menging benadert door sterke horizontale menging en zwakke verticale menging voor te schrijven. De oriëntatie van dichtheidsvlakken in de oceaan is weliswaar bijna horizontaal, maar niet precies. In hoofdstuk 2 wordt daarom gekeken of het verschil in schaling een robuust resultaat is. Dit blijkt niet het geval. In het geïdealiseerde geval waarin geen windforcering wordt opgelegd, is de schaling in beide bekkens in overeenstemming met de klassieke relatie, ongeacht hoe de mengprocessen gerepresenteerd worden. Is er wel windforcering, dan maakt de representatie van menging uit voor het resultaat. In dat geval zorgt de onnauwkeurige horizontaal/verticaal parametrisatie van menging (zoals in THCM) voor een verschil in schaling dat niet bestaat als een isopycnisch/diapycnisch schema gebruikt wordt.

In hoofdstuk 3 staat een ander mengproces centraal: dat ten gevolge van verticale convectie. Dit proces speelt op een schaal van ongeveer 1 km. Het zorgt voor een sterke verticale menging, zodra water een dichtheid krijgt die groter is dan die van het water dat zich eronder bevindt. Van convectie wordt aangenomen dat het een belangrijke rol speelt in de niet-lineaire dynamica van de Atlantische MOC, omdat convectieve processen mede de dichtheid in het noorden van het bekken bepalen. Voor de representatie van convectie wordt vaak een schema gebruik dat "convectieve aanpassing" (CA) heet. Dit schema maakt simpelweg de verticale mengcoëfficiënt heel groot, zodra zich zwaar water boven lichter water bevindt. Op basis van resultaten uit THCM en de analyse van een eenvoudig eendimensionaal model blijkt echter dat CA verantwoordelijk is voor het bestaan van artifiële meervoudige evenwichten. Hoewel dit tegenintuïtief klinkt, wordt aangetoond dat het aantal evenwichtstoestanden toeneemt als de verticale roosterafstand verkleind wordt. Op basis van deze studie is duidelijk dat grote voorzichtigheid betracht moet worden bij het analyseren van de relatie tussen de MOC en verticale convectie.

Hoofdstuk 4 gaat over de representatie van de atmosfeer in een oceaanmodel. De uitwisseling van impuls, warmte en zoet water tussen de oceaan en de atmosfeer is op verschillende manieren afhankelijk van de temperatuur van het water aan het oppervlak. Zoals hierboven al aangegeven, is er een directe relatie tussen de uitwisseling van warmte en de watertempera-

tuur. Voor de sterkte van de wind en de uitwisseling van zoetwater is deze relatie niet direct[#]. In oceaanmodellen wordt dit onderscheid meestal op tamelijk rigide wijze gemaakt door aan te nemen dat wind en de uitwisseling van zoet water geheel onafhankelijk zijn van de watertemperatuur. Nu zijn in dergelijke modellen meervoudige evenwichten ten gevolge van de zout-advectie-terugkoppeling al veelvuldig aangetoond. Daartegenover staat dat in de meest geavanceerde klimaatmodellen nog geen aanwijzingen gevonden zijn dat meervoudige evenwichten daadwerkelijk bestaan. Uit deze tegenstelling is de hypothese voortgekomen dat de interactie tussen oceaan en atmosfeer *te* eenvoudig wordt weergegeven in de oceaanmodellen.

In hoofdtuk 4 wordt deze hypothese getoetst door het oceaanmodel THCM uit te breiden met een zogenaamd statistisch atmosfeermodel. Dit is een representatie van de atmosfeer op basis van een statistische analyse van de uitkomsten van een geavanceerd klimaatmodel. De analyse is op zo'n manier gedaan, dat de uitwisseling van impuls, warmte en zoet water tussen oceaan en atmosfeer wordt uitgedrukt als functie van de temperatuur van het water aan het oppervlak. Het was al bekend dat in THCM meervoudige evenwichten bestaan. In tegenspraak met de hierboven gestelde hypothese blijken deze nog steeds te bestaan nadat het model is uitgebreid met het statistische atmosfeermodel.

In hoofdstuk 5 wordt ingegaan op de rol die de horizontale roosterafstand van een model speelt bij de representatie van transportprocessen in de oceaan. Er worden twee modellen met elkaar vergeleken. In de één is de roosterafstand 1°, in de ander 0.1°. Het belangrijkste verschil hiertussen is, dat in het tweede geval wervels ("eddies") expliciet worden opgelost, terwijl ze in het eerste geval geparametriseerd worden. De modellen die in de hiervoor besproken hoofdstukken gebruikt zijn, werkten ook op basis van een parametrisatie voor wervels. Wervels representeren echter een dominante vorm van oceanische variabiliteit die alleen gesimuleerd wordt door ze expliciet op te lossen. Bovendien zijn wervels van groot belang voor het transport van bijvoorbeeld energie en zout.

De vraag die in hoofdstuk 5 gesteld wordt, is of de zout-advectie-terugkoppeling een verschillend karakter heeft in de twee modellen. De analyse in dit hoofdstuk suggereert dat dit inderdaad het geval is. De resultaten van het model met een roosterafstand van 1° lijken goed in overeenstemming met de aannames die gemaakt worden bij het zout-advectie-terugkoppelingsmechanisme. In het model dat wervels oplost, is dat niet zo. Zo gaat een afname van de MOC in dit model gepaard met een toename van het noord-zuid dichtheidsverschil. Verder lijkt de afname van de MOC geen significante invloed te hebben op het transport van zout naar het noorden.

Op basis van de resultaten die in dit proefschrift gepresenteerd zijn, lijdt het geen twijfel dat de dynamica van de MOC niet-lineair is. Hoe deze eigenschap zich in werkelijkheid manifesteert is echter nog niet duidelijk. Om dit probleem verder te kunnen onderzoeken is het van het grootste belang dat observationeel onderzoek voortgang vindt, zodat er meer gegevens beschikbaar komen om modellen aan te toetsen. Daarnaast is ook de methodiek die in dit proefschrift gevolgd is, vruchtbaar gebleken. Door op systematische wijze het gesimuleerde gedrag van de MOC te vergelijken tussen modellen waarin een bepaald proces op verschillende wijze wordt voorgesteld, is het mogelijk de betrouwbaarheid van de uitkomsten uit die modellen af te schatten.

[#]Merk evenwel op dat verdamping wel van de watertemperatuur afhangt.

1

Introduction

Traditionally, the word "climate" refers to the typical weather conditions of a particular region on Earth, consistent with its ancient Greek origin, *Klima*, meaning "slope" or "region". It is now well established, however, that climate is not simply a function of location, but that variability occurs at a multitude of temporal and spatial scales. As illustrated qualitatively in the composite spectrum in Fig. 1.1, there are several frequency ranges for which the variance exceeds the background (red) noise variance. Although some periods, such as 1 day and 1 year, are obviously imposed by the variation in external forcing, most of the peaks are the result of intrinsic, internal variability, indicating that the underlying system is fundamentally nonlinear (Dijkstra and Ghil, 2005).

In order to explain the full range of variability, it is not sufficient to only consider the atmosphere, but one also has to take into account the hydrosphere (all liquid water), the cryosphere (all frozen water), the biosphere (all living organisms), and the upper lithosphere (the uppermost layer of the solid Earth). Together, these "spheres" make up the climate system. Although the system is, in principle, governed by well-known physical laws, such as Newton's laws of motion, its size and complexity prohibit the construction of a single model that accounts for the dynamics of all components at all spatial and temporal scales. Therefore, if one sets out to investigate the sensitivity to changes in external conditions, or to predict the future state of the climate system over a certain time frame, one has to decide which aspects of the system must be included in the model, and how they need to be represented.

This problem is a strong motivation for research aimed at understanding observed climate phenomena, such as the El Niño-Southern Oscillation (ENSO; Philander, 1990; Dijkstra, 2006) or the Atlantic Multidecadal Oscillation (AMO; Enfield et al., 2001). A fundamental approach is to search for the simplest possible physical representation of a particular phenomenon that still reproduces the observed characteristics in a qualitative way. Once available, such a "minimal" model may provide guidelines for what behavior to expect in
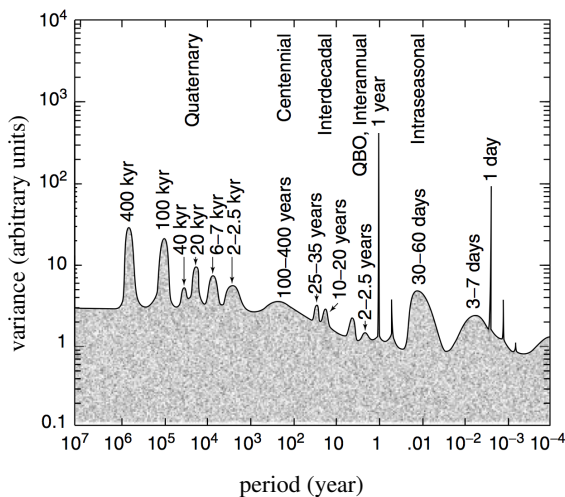
Figure 1.1: Artist's rendering of the power spectrum of climate variability, based on information from various observational records. From Dijkstra and Ghil (2005).

more realistic models. For example, the minimal model of the AMO discussed by Dijkstra et al. (2008) indicates that this mode of variability is only recovered in a climate forecast simulation if the damping of sea surface temperature anomalies is sufficiently weak .

In many cases, however, observational records are too short or have insufficient spatial coverage to allow a comprehensive qualitative comparison between real world phenomena and the features of a model. A necessary complementary approach to evaluate which elements are essential in a model is therefore to systematically vary the complexity of the model. The basic idea behind this approach is to evaluate if the features of a model are robust to an improvement of the model (for example, if a coupled ocean-atmosphere model is considered instead of an ocean-only model). Only if the behavior of the model changes in a qualitative sense, the added complexity should be regarded as an essential element of the model. The studies presented in this thesis, which are introduced below, are all based on this strategy.

The subject of this thesis is the large-scale ocean circulation, which has an important role in shaping the current climate, as will be reviewed in section 1.1. Specifically, the research presented here is concerned with phenomena that have their origin in so-called thermohaline feedbacks, a concept that will be explained in section 1.2. The main focus is on the possibility of an abrupt reorganization of the large-scale circulation as a result of the system being forced across a threshold, which is a timely issue to tackle in view of anthropogenic climate change. The presence of thresholds is suggested by numerical ocean-climate models (Bryan, 1986; Rahmstorf et al., 2005), and would also partially explain the abrupt climate transitions inferred from ice core records from the last glacial period (Ganopolski and Rahmstorf, 2001; Clark et al., 2002; Alley et al., 2003). The theory is, however, far from complete. The work presented here aims to make progress in this matter by systematically analyzing models of the large-scale circulation, exploring a different aspect of model complexity in each chapter. In chapters 2, 3, and 4 the analysis relies on the technique of numerical steady-state contin-
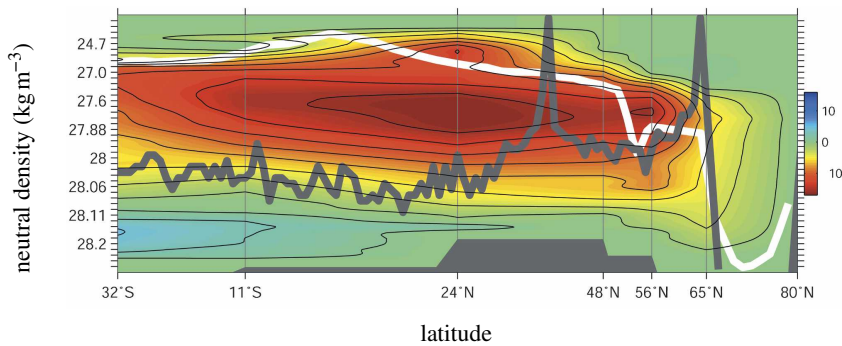
Figure 1.2: Stream function (every 2 Sv contoured) of the overturning circulation in the Atlantic Ocean, as estimated from the inversion of observational data. From Lumpkin and Speer (2007), to which I refer for further details.

uation, which will be introduced in section 1.3. Section 1.4 then concludes this introductory chapter with the formulation of the problem and an overview of the material covered by this thesis.

1.1 The role of the large-scale ocean circulation in the climate system

The world ocean comprises the bulk of the hydrosphere, but its impact goes beyond that of reservoir in the hydrological cycle. Due to the large mass of the oceans and the high heat capacity of water compared to that of air and soil, the world ocean has an important moderating effect on global air temperature. It additionally leads to the introduction of memory into the climate system (Hasselmann, 1976). Furthermore, the capacity of water to dissolve chemical compounds causes the ocean to have impact on the composition of the atmosphere, and, since some compounds serve as nutrients to organisms, allows the biosphere to extend below the ocean surface.

Besides its function as reservoir, the ocean participates in the global redistribution of freshwater, heat, and chemical compounds. Measurements taken along basin-wide sections, such as done, for example, during the World Ocean Circulation Experiment (WOCE) field program, reveal patterns of salinity, temperature, and biogeochemical tracers that extend over the entire basin (Van Aken, 2007). Based on these patterns, water masses with common characteristics have been identified that are labelled according to their region of formation. A prominent example is North Atlantic Deep Water (NADW), which can be traced throughout the Atlantic and into the Southern Ocean. These observations have led to the idea that there is a more or less coherent, global-scale system of currents, enabling interhemispheric and interbasin exchange of tracers (Gordon, 1986; Zika et al., 2012).

A useful way of portraying the large-scale circulation is by calculating the stream function of the zonally integrated meridional flow. Owing to the fact that the flow is in approximate geostrophic balance at the temporal and spatial scales of interest, the meridional transport
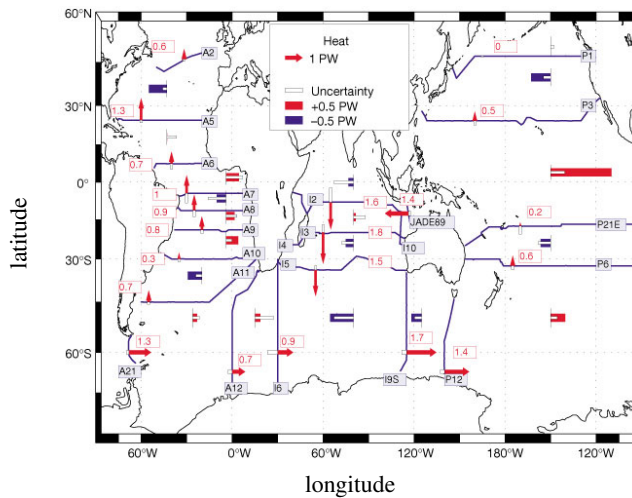
Figure 1.3: Estimated heat transports across WOCE sections, indicated by arrows and red numbers (positive northward/eastward), where $1\,\mathrm{PW} = 10^{15}\,\mathrm{W}$. The white box at the tail end of each arrow is the one-standard-deviation uncertainty. Between sections, ocean-atmosphere heat transfers are indicated by the zonal length of the colored boxes (blue for ocean cooling; red for ocean heating), with the length of the white box inside indicating the uncertainty. From Ganachaud and Wunsch (2000).

can be reconstructed from observations (Lumpkin and Speer, 2007; Kanzow et al., 2007). Figure 1.2 shows that the result for the Atlantic Ocean is a basin-scale overturning circulation characterized by a net downward flux of about $16\,\mathrm{Sv}$ ($1\,\mathrm{Sv} = 10^6\,\mathrm{m}^3\,\mathrm{s}^{-1}$) at high latitudes. Only part of the compensating upwelling occurs within the Atlantic, the remaining part taking place in the Southern Ocean and in the Pacific Ocean. Clearly, the Meridional Overturning Circulation (MOC) is asymmetric with respect to the equator. In addition, the Atlantic MOC is very different from that in the Pacific, where there is no deep water formation (Warren, 1983).

As illustrated in Fig. 1.3, these geographic asymmetries are reflected in the section-wide heat transports calculated by Ganachaud and Wunsch (2000) for the WOCE sections. In the Atlantic, heat transports are to the North throughout the basin, while the combined heat transport of the Pacific and Indian Oceans is poleward in both hemispheres. A model experiment in which the Atlantic MOC is artificially shut down suggests that Northern Hemispheric temperatures could be 1-2°C lower in absence of the MOC induced heat transport (Vellinga and Wood, 2002). Through its effect on temperature, the heat transport by the MOC is also likely to control large-scale patterns of evaporation and precipitation, winds, the extent of sea ice, and the geographical distribution of ocean-dwelling organisms. So, even though this overview cannot be comprehensive, it is clear that the presence of a large-scale overturning circulation has a distinct impact on climate and as such is of great social, economical, and ecological significance.

1.2   Thermohaline feedbacks

The thermohaline feedbacks introduced here involve the presence in the ocean of the tracers temperature ("thermo-") and salinity ("-haline"), which (together with pressure) determine the density of ocean water. The density distribution in the ocean is thus in part governed by heat and salt advection by ocean currents. In turn, the density field affects the ocean's flow field through its effect on horizontal pressure gradients. Here, I sketch how this nonlinear interaction plays a role in the dynamics of the large-scale overturning circulation.

1.2.1   Low order models

In a scaling analysis of the problem the strength of the MOC (Ψ) may be regarded as proportional to some characteristic horizontal velocity V, a length scale L, and a depth scale δ, i.e.

$$\Psi \sim VL\delta. \tag{1.1}$$

The scale V is assumed representative for both zonal (u) and meridional (v) velocities, which may be related to density (ρ) by the thermal wind balance,

$$-f\frac{\partial v}{\partial z} = \frac{g}{\rho_0 r_0 \cos\phi}\frac{\partial \rho}{\partial \lambda}, \qquad f\frac{\partial u}{\partial z} = \frac{g}{\rho_0 r_0}\frac{\partial \rho}{\partial \phi}, \tag{1.2}$$

where λ is longitude, ϕ latitude, z the vertical direction (positive upwards), r_0 the radius of Earth, f a characteristic value of the Coriolis parameter, g is the standard gravity, and ρ_0 a reference density. Denoting typical horizontal density variations by $\Delta\rho$, the scaling for V is given by

$$V \sim \frac{g}{\rho_0 fL}\Delta\rho\,\delta, \tag{1.3}$$

which combined with Eq. (1.1) yields

$$\Psi \sim \frac{g}{\rho_0 f}\Delta\rho\,\delta^2. \tag{1.4}$$

In this relation, $\Delta\rho$ and δ should in principle be considered as unknowns, because they may be determined in part by Ψ.

First, however, assume that $\Delta\rho$ is a fixed external parameter. An estimate for δ may then be obtained by assuming that there is a balance between vertical (in fact, diapycnal) advection and diffusion of density in the ocean interior (Munk and Wunsch, 1998), which is expressed as

$$w\frac{\partial \rho}{\partial z} = K_V\frac{\partial^2 \rho}{\partial z^2}, \tag{1.5}$$

where w is the vertical velocity and K_V the vertical diffusion coefficient. Denoting the characteristic vertical velocity by W and using the continuity equation ($U/L \sim W/\delta$), the scaling of the MOC strength can be written as

$$\Psi \sim WL^2 \sim K_V L^2 \frac{1}{\delta}. \tag{1.6}$$

Equating the relations in Eq. (1.4) and Eq. (1.6), and reorganizing the result, finally gives

$$\Psi \sim \left(\frac{L^4 g}{\rho_0 f} \right)^{1/3} \left(K_V^2 \Delta \rho \right)^{1/3}, \tag{1.7}$$

which is sometimes referred to as the *classical scaling* relation (Park and Bryan, 2000). So, under the assumptions made in this paragraph the thermohaline feedback is manifest as a nonlinear dependence of Ψ on the model parameter K_V and the external forcing parameter $\Delta \rho$. The classical scaling relation is the starting point for the work presented in chapter 2.

The assumption of constant $\Delta \rho$ is often motivated by the fact that there is a strong, negative feedback between sea surface temperature variations and the surface heat flux, as a result of which the impact of ocean currents on the upper ocean temperature field is only of second order importance. There is, however, no relation between sea surface salinity and the surface freshwater flux, so that ocean currents are of first order importance for determining salinities in the upper ocean. This asymmetry between the two tracers gives rise to the so-called *salt-advection feedback*, which has been hypothesized to lead to a strong sensitivity of the MOC to changes in the freshwater flux across the surface. To understand in a conceptual way how the feedback may affect the Atlantic MOC (Fig. 1.2), assume a freshwater perturbation is applied in the northern part of the basin. As a result of such perturbation, the water column will locally become less dense. If, then, density (and pressure) gradients are affected in such a way that the strength of the overturning decreases, the surface branch of the MOC would transport less salt from the equatorial region to the north, and the original freshwater perturbation would be amplified.

The salt-advection feedback was investigated in a seminal paper by Stommel (1961). Here, we present the slightly modified version of his model due to Marotzke (1990). It consists of two boxes of equal volume (Fig. 1.4a), each containing well mixed water of temperature T_i and salinity S_i ($i = 1, 2$). The exchange between the boxes, which is positive for deep flow from box 1 to box 2, is given by

$$q = -K \Delta \rho = K \left(\alpha_T \Delta T - \alpha_S \Delta S \right), \tag{1.8}$$

where $K > 0$ is a constant, $\Delta X = X_2 - X_1$ for $X = T, S, \rho$, and α_T and α_S are the thermal expansion and haline contraction coefficients, respectively. The meridional transport is represented by the symbol q instead of Ψ in order to signify the difference with the scaling approach followed above. Specifically, note that the vertical structure of the ocean is not taken into account in this model (the two approaches can be reconciled by assuming that depth scale δ in Eq. (1.4) is not influenced by Ψ; Rahmstorf, 1996). The temperatures are held constant, with $\Delta T > 0$, while the temporal (t) evolution of the salinities is given by

$$\frac{dS_1}{dt} = |q| (S_2 - S_1) - H_S, \qquad \frac{dS_2}{dt} = |q| (S_1 - S_2) + H_S. \tag{1.9}$$

Here, H_S represents a "salinity flux", as a model for atmospheric freshwater exchange.

Figure 1.4b shows that in this conceptual model the salt advection feedback leads to the presence of multiple steady states for a certain range of the forcing parameter H_S. In the solutions with $q > 0$ the driving is dominated by the imposed thermal gradient ΔT [see Eq. (1.8)]. In the solutions with $q < 0$, on the other hand, the driving is dominated by the
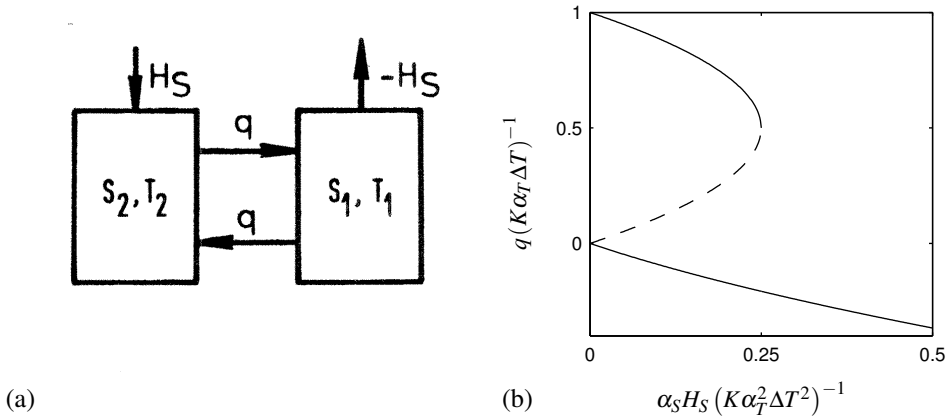
Figure 1.4: (a) Two box model due to Marotzke (1990). (b) Nondimensional equilibrium solutions of the model. The solid parts of the curve mark linearly stable solutions, while the dashed part indicates the unstable regime.

salinity gradient ΔS, which is large enough to do so because q is small. The multiple equilibria regime arises because the temperature driven circulation can be maintained provided that $H_S \leq H_S^{crit}$, where $H_S^{crit} = K\alpha_T^2\Delta T^2/4\alpha_S > 0$, while the salinity driven circulation is possible provided that $H_S \geq 0$. Within the parameter range $[0, H_S^{crit}]$ transitions from one stable state to the other may be induced by a temporary perturbation of the freshwater forcing H_S. Consider, for example, a linearly stable steady state with $q > 0$. The positive feedback loop explaining a possible transition to a state with $q < 0$ is then as follows: A positive perturbation of H_S causes ΔS to increase [Eq. (1.9)], leading to a reduction of q [Eq. (1.8)]. This, in turn, results in a further increase of ΔS. The presence of multiple steady states and the possibility of abrupt transitions of the oceanic circulation as a result of the salt-advection feedback is considered further in chapters 3, 4, and 5.

In the configuration discussed above, the box model is meant to represent the overturning circulation, and the different equilibria would correspond to different large-scale circulation patterns. It has been proposed that a mechanism similar to the salt-advection feedback is relevant for oceanic convection, although the scale of this process is much smaller, being on the order of 1 km (Jones and Marshall, 1993). Based on a model consisting of two stacked boxes, exchanging properties at a rate dependent on the vertical density gradient, Welander (1982) and Lenderink and Haarsma (1994) suggested that there is a *convective feedback*, which may also be responsible for multiple equilibria (as well as intrinsic variability), but in this case corresponding to different convection patterns. The representation of the convective feedback in ocean models is the topic of the work presented in chapter 3.

The simple models discussed here are meant as an illustration of the possible role of thermohaline feedbacks in the large-scale circulation. Although the approach of low order models may be pursued by combining the thermohaline feedbacks described above in a single model (Wunsch, 2005; Colin de Verdière et al., 2006), the relevance of these feedbacks for the real world may only be assessed with more complete models of the overturning circulation.

1.2.2 Numerical model results

The results of Park and Bryan (2000) suggest that the classical scaling relation in Eq. (1.7) holds for thermally driven flows in a single-hemispheric basin. In more complex models of the global ocean, however, other pathways than diffusion driven upwelling [Eq. (1.5)] may be important for returning deep waters to the surface. Specifically, it has been suggested that Southern Ocean wind stress and eddies play a crucial role in maintaining an inter-hemispheric deep overturning circulation independent of diapycnal mixing (Toggweiler and Samuels, 1998; Gnanadesikan, 1999; Wolfe and Cessi, 2011). Establishing whether the main driver of the overturning is diapycnal mixing or wind stress is an important issue, because the two processes could imply a different sensitivity to external parameters, such as the atmospheric freshwater forcing. The study in chapter 2 follows up on two studies that indicate that the overturning circulations in the Atlantic and Pacific are governed by different dynamics, as witnessed by a different sensitivity of their strength to the vertical diffusion coefficient K_V.

Starting with the results of Bryan (1986), numerous models have been shown to feature multiple equilibria as a result of to the salt advection feedback. Multiple steady states are present in two- (Cessi and Young, 1992), and three-dimensional ocean-only models (Marotzke, 1991; Weijer and Dijkstra, 2001), and in Earth System Models of Intermediate Complexitiy (EMICS; Rahmstorf et al., 2005). Multiple equilibria have not yet been found in the most advanced climate models, such as those used in the fourth assessment report of the Intergovernmental Panel on Climate Change (IPCC; Meehl et al., 2007). There is no permanent transition of the MOC in the future projections discussed by Schmittner et al. (2005), or in the experiments described by Stouffer et al. (2006), in which the high latitude freshwater flux is temporarily perturbed. These findings are often thought to indicate that multiple equilibria are an artifact of simpler (ocean-only) models. In this view, the salt-advection feedback would be counteracted by changes in atmospheric forcing that arise as the MOC changes (Yin et al., 2006). However, a systematic investigation of the effect of such atmospheric feedbacks on the stability of the MOC is still lacking. This problem will be considered in chapter 4.

The formulation of the box model of Marotzke (1990) suggests that there can only be a large-scale salt-advection feedback provided that the overturning strength is proportional to a meridional density contrast. Such relation is supported by the scaled thermal wind equations [Eq. (1.4); Marotzke, 1997] and may indeed be established in three-dimensional ocean models (Rahmstorf, 1996). Based on the results from a high resolution, eddy-resolving model, however, no relation between overturning strength and density contrast could be found, despite the fact that the MOC in such a model turns out to be more sensitive to freshwater than in coarse resolution models (Weijer et al., 2012). Understanding the sensitivity to freshwater perturbations of the MOC in an eddying ocean is therefore another important open issue, which will be addressed in chapter 5.

1.3 Numerical steady-state continuation

Numerical steady-state continuation is a tool that makes it feasible to explore and understand the qualitative behavior of a discretized model. It may be used as an efficient way to explore a large range of parameter values, such as in chapter 2, but it is particularly powerful when used to perform bifurcation analysis, as in chapters 3 and 4.

Bifurcation analysis is a concept from nonlinear dynamical systems theory, whose strength lies in the fact that it links changes in the qualitative behavior of a system to the properties of its mathematical formulation (Seydel, 1988). Abrupt transitions, the presence of intrinsic variability, or chaotic model behavior can all be neatly explained by identifying the so-called bifurcation points that are responsible for these phenomena. A bifurcation point is defined by a change in the topology of the model trajectories in phase space that occurs as a result of the variation of a parameter (the bifurcation parameter). For the scope of this thesis an important bifurcation is the *saddle-node* bifurcation, which is characterized by the fact that one one side of the bifurcation two equilibria exist, while on the other side these two equilibria have disappeared. The multiple equilibria regime in the two-box model of Marotzke (1990) discussed above is indeed defined by two saddle-node bifurcations. With numerical bifurcation analysis, regimes of multiple equilibria may also be found efficiently in numerical ocean-climate models.

1.3.1 Mathematical description

To set the stage, suppose that a system of autonomous partial differential equations is nondimensionalized and discretized in space, resulting in a set of N ordinary differential equations of the form

$$\mathsf{M}\frac{\mathrm{d}\mathbf{x}}{\mathrm{d}t} = \mathscr{F}(\mathbf{x}, \gamma). \tag{1.10}$$

Here, $\mathbf{x}$ is the N-dimensional state vector, t is time, M is a diagonal matrix and $\mathscr{F}(\mathbf{x}, \gamma) : \mathbb{R}^{N+p} \to \mathbb{R}^N$ is a smooth (sufficiently differentiable) vector field. The integer p indicates the number of adjustable parameters, but in Eq. (1.10) only the dependence on the bifurcation parameter γ is made explicit. A solution $\bar{\mathbf{x}}$ is a fixed point if

$$\mathscr{F}(\bar{\mathbf{x}}, \gamma) = \mathbf{0}. \tag{1.11}$$

The stability of such a fixed point can be analyzed by considering the evolution of $\mathbf{x} = \bar{\mathbf{x}} + \mathbf{y}$, where $\mathbf{y}$ is a small perturbation. Linearization of Eq. (1.10) around $\bar{\mathbf{x}}$ then gives

$$\mathsf{M}\frac{\mathrm{d}\mathbf{y}}{\mathrm{d}t} = \Phi(\bar{\mathbf{x}}, \gamma)\mathbf{y}. \tag{1.12}$$

Here, Φ is the $N \times N$ Jacobian matrix, whose columns are formed by the derivatives of $\mathscr{F}$ with respect to the entries of $\mathbf{x}$. Substitution of $\mathbf{y} = \hat{\mathbf{y}}e^{\sigma t}$ leads to a generalized eigenvalue problem for the growth factor σ,

$$\sigma\mathsf{M}\hat{\mathbf{y}} = \Phi(\bar{\mathbf{x}}, \gamma)\hat{\mathbf{y}}. \tag{1.13}$$

Equation (1.12) defines the local topology of trajectories close to $\bar{\mathbf{x}}$. So, if one or more eigenvalues σ cross the imaginary axis as γ is varied, the behavior of the system changes in a qualitative sense. This means that the occurrence of a (local) bifurcation is related to the Jacobian matrix Φ being singular. The eigenvalue problem in Eq. (1.13) may be solved numerically, for example by the Jacobi-Davidson QZ method (Sleijpen and Van der Vorst, 2000), but a discussion of this matter is outside the scope of this chapter.

Fixed points can be followed in parameter space using a numerical continuation algorithm. Here, the pseudo-arclength method (Keller, 1977) is discussed, which relies on the introduction of an additional parameter s to parameterize a branch of solutions $\Upsilon(s) = (\bar{\mathbf{x}}(s), \gamma(s))$. The set of equations is closed by adding an equation of the form

$$r(\bar{\mathbf{x}}, \gamma) = \dot{\mathbf{x}}_0^T (\bar{\mathbf{x}} - \mathbf{x}_0) + \dot{\gamma}_0 (\gamma - \gamma_0) - \Delta s = 0. \tag{1.14}$$

The subscripts 0 are used to denote a previous (known) solution on the branch, dots indicate the derivative with respect to s, and Δs is the step size of the arclength parameter. Solutions of the augmented system of equations [Eqs. (1.11) and (1.14)] are found by Newton's method. Starting from an initial guess Υ^0 the Newton updates $\Upsilon^{k+1} - \Upsilon^k$ of each iteration (with counter k) are found from

$$\begin{pmatrix} \Phi(\mathbf{x}^k, \gamma^k) & \partial\mathscr{F}(\mathbf{x}^k, \gamma^k)/\partial\gamma \\ \dot{\mathbf{x}}_0^T & \dot{\gamma}_0 \end{pmatrix} \begin{pmatrix} \mathbf{x}^{k+1} - \mathbf{x}^k \\ \gamma^{k+1} - \gamma^k \end{pmatrix} = \begin{pmatrix} -\mathscr{F}(\mathbf{x}^k, \gamma^k) \\ -r(\mathbf{x}^k, \gamma^k) \end{pmatrix}. \tag{1.15}$$

So, in each iteration a linear system of equations must be solved. A new steady state is found when the Newton process has converged up to a prescribed tolerance.

1.3.2 Application to large-scale ocean modelling

Following the fixed points of an ocean-climate model in parameter space is a computationally intensive task if a conventional time stepping method is used. For the computation of each subsequent steady state, the model must be run to equilibrium. A faster, but less accurate method is sometimes adopted in which the bifurcation parameter is slowly varied in time, based on the expectation that the transient model state remains close to the true equilibrium state at all times. In the following I compare this approach to the method of numerical continuation as an illustrative example of the power of the latter.

As an example problem, I consider the sensitivity of the MOC to perturbations of the surface freshwater flux in the two-dimensional (latitude/depth) double-hemisphere model discussed in section 3.2, to which I refer for further details. The model captures the salt advection feedback discussed in the previous section and, as a result, features multiple equilibria. This is illustrated by using the amplitude of a freshwater perturbation as the bifurcation parameter.

The black line in Fig. 1.5 corresponds to the bifurcation diagram computed by pseudo-arclength continuation. It shows the exact boundaries of the multiple equilibria regime. Approximations of these boundaries may be found in hysteresis experiments. Here, I perform three of such simulations, starting from the fixed point indicated in Fig. 1.5. First, the amplitude of the freshwater perturbation is increased slowly from 0 up to 100 mSv, then it is decreased down to -100 mSv, and finally it is increased up to 0. The colored lines in Fig. 1.5 correspond to the hysteresis loops for different rates of change of the freshwater perturbation amplitude. When using a rate of 200 mSv kyr^{-1}, the simulation takes only 2000 model years to complete, but it results in a rather poor approximation of the bifurcation diagram. The result is better for a rate of 50 mSv kyr^{-1} (such as used in Rahmstorf et al., 2005), but only for a rate of 10 mSv kyr^{-1} the point of strong MOC reduction corresponds closely to the upper boundary of the multiple equilibria regime. However, in that case the entire hysteresis

experiment would take 40 kyr to complete (I stopped after 10 kyr). The hysteresis approach compares even less favorably to the continuation method if not only its ability to identify the multiple equilibria regime is taken into account, but also the accuracy of approximating the steady state MOC strength.
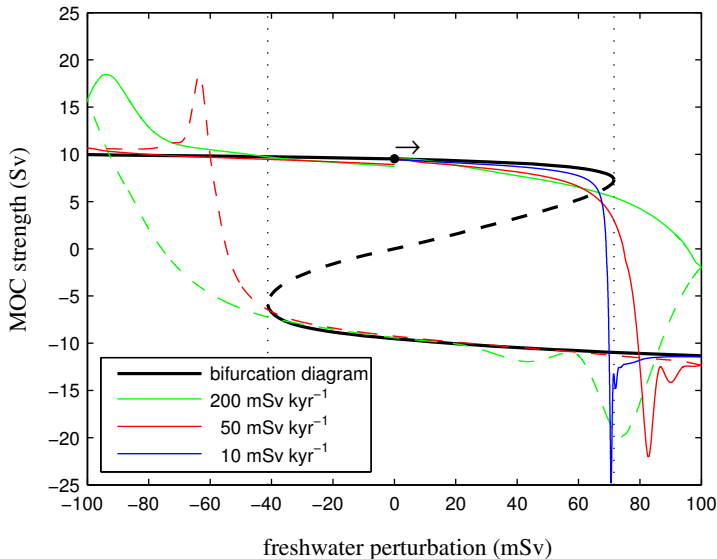

Figure 1.5: Comparison of an exact bifurcation diagram with approximating hysteresis curves. The bifurcation diagram (black line) shows linearly stable states as solid lines, while unstable states are indicated by the dashed line. All hysteresis curves (colored lines) start from the fixed point indicated by the black dot, but the change of the bifurcation parameter in time is different for each curve.

1.3.3 Challenges

When using numerical continuation techniques to explore the parameter space of an ocean-climate model, considerable challenges arise due to the dimension of the system. For a typical coarse-resolution, global configuration $N = \mathcal{O}\left(10^6\right)$. The linear system in Eq. (1.15) can therefore not be solved by Gauss elimination. Instead, the application of iterative solution techniques is required, along with the use of adequate preconditioning to speed up the convergence of the iterative procedure (Saad, 1996). Although these methods may also be implemented in existing ocean models (Bernsen et al., 2008), the Institute for Marine and Atmospheric research Utrecht (IMAU) of Utrecht University has invested in the development of an ocean model tailored for numerical bifurcation analysis since the end of the 1990s. This code is referred to as the ThermoHaline Circulation Model (THCM). It is based on the three-dimensional hydrostatic primitive equations in spherical coordinates, includes temperature and salinity as active tracers, and allows the specification of realistic bottom topography. For problems with sizes up to $N \approx 10^5$, corresponding to a global model with a 4° horizontal

resolution and about 20 layers in the vertical, the code can be run on a single processor. Recent advances allow the use of parallel computing (Thies et al., 2009), so that investigating problems with several million degrees of freedom is in principle feasible.

There are, however, several obstacles for the application of numerical bifurcation analysis to ocean models that are not directly related to N. One is the emergence of wiggles in the solution, which may occur if an Arakawa C-grid is used for the horizontal discretization, as in the version of THCM described by Weijer et al. (2003, referred to as THMC-C). These wiggles result from lateral Ekman layers being unresolved and can only be damped by adopting a (unrealistically) large lateral friction coefficient (Wubs et al., 2006). This problem was solved by De Niet et al. (2007), who developed an Arakawa B-grid version of the model (referred to as THCM-B).

A second shortcoming of THCM is its difficulty to operate with a parameterization of tracer mixing by mesoscale eddies and other subgrid scale motions (Redi, 1982; Gent and McWilliams, 1990) that is more realistic than simple horizontal mixing (see chapter 2 for a longer discussion). Such parameterization is not implemented in THCM-C, and although it is part of THCM-B (Den Toom et al., 2009), it turns out that it cannot be used in general due to ill convergence of the iterative solver. The reason for this behavior is currently unknown. Therefore, the effect of this deficiency is assessed in chapter 2.

A third problem is related to the need for a procedure to remove (non-physical) static instabilities, which arise because convection is typically not resolved. Such procedures often involve rules that are not differentiable. Hence, no representation of convection is included in THCM-C. Weijer et al. (2003) show that the model is still useful for studying the large-scale circulation, despite the need of using a large friction coefficient and the absence of a representation of convection. However, if the friction coefficient is set to a more realistic value, as is done in THCM-B, unrealistic flow patterns result without a procedure to remove static instabilities (Marotzke and Scott, 1999). Therefore, a continuous version of the often used convective adjustment (CA) scheme is included in THCM-B. De Niet et al. (2007) illustrate that it can be used successfully for problems in which there is effectively only one active tracer. However, the model becomes very inefficient if different boundary conditions are used for temperature and salinity, which is needed to model the salt advection feedback. This problem is investigated further in chapter 3. Because there is currently no physically acceptable solution for this issue, the study presented in chapter 4 relies on THCM-C instead of the more recent version, THCM-B.

1.4   Problem formulation and thesis overview

In short, each of the studies presented in this thesis aims to contribute to the understanding of the following problem:

> To what degree is the behavior of the global ocean circulation determined
> by thermohaline feedbacks?

Theories of the way the large-scale circulation works are relatively ill constrained by observations. While the ocean surface can be surveyed by satellites, information from the deep

ocean is only available in the form of point-wise measurements, which at best provide a picture of the zonally integrated circulation. In addition, the length of observational records is often short compared to the centennial to millennial timescale typical for the variability of the global overturning circulation. In this thesis, therefore, progress in this problem is made by systematically analyzing numerical ocean-climate models of different complexity. The aim of this analysis is to test the robustness of numerical model results that are used to estimate the sensitivity of the overturning circulation to changes in external conditions.

The following four subproblems are considered in this thesis:

1. The study presented in **chapter 2** builds on papers by Dalan et al. (2005) and Dijkstra (2008) that indicate that in global ocean models the MOC in Pacific and the Atlantic Ocean is governed by different dynamics, as witnessed by a different sensitivity of the MOC strength to the vertical diffusion coefficient K_V. The Pacific MOC appears to follow the classical scaling law [Eq. (1.7)], but the sensitivity to vertical diffusivity is weaker for the Atlantic MOC. The question is whether this result reflects an intrinsic property of the present-day global-scale circulation. Is it the consequence of deep water formation being present in the Atlantic and absent in the Pacific? Or does the result depend on model boundary conditions and parameterizations? In particular, we examine the role of wind stress and evaluate if the results are sensitive to the choice of the parameterization of lateral mixing of tracers. This way, we can assess for which type of problems TCHM can be applied reliably, despite the model's poor representation of mesoscale eddies.

2. In **chapter 3** we critically analyze the performance of the so-called convective adjustment (CA) scheme, which is commonly used in ocean-climate models to eliminate static instabilities that arise because convection is not resolved. It has been claimed that convective dynamics are a potential source of multiple equilibria due to the convective feedback (Lenderink and Haarsma, 1994), which may be particularly important when the MOC is primarily driven by wind instead of by diffusion (Hofmann and Rahmstorf, 2009). The problems with the use of CA in the THCM-B model (De Niet et al., 2007) motivate to extend the analysis of Vellinga (1998), and to further investigate the origin of the multiple equilibria related to CA.

3. As reviewed above, multiple equilibria due to the salt advection feedback (Fig. 1.4) are found in a hierarchy of models. In **chapter 4** we consider the suggestion that atmospheric feedbacks tend to oppose the oceanic salt feedback (Yin et al., 2006), rendering multiple equilibria an artifact of ocean-only models. We investigate this idea by using a hybrid coupled model, which is based on the THCM-C model (Weijer et al., 2003), and an empirical description of the atmospheric fluxes (Cimatoribus et al., 2012). The advantage of this approach is that atmospheric feedbacks can be switched on and off at will. The aim is to compare the size of the multiple equilibria regime with and without an atmosphere present, and to explain the differences.

4. Observations indicate that the strength of the MOC is highly variable (Cunningham et al., 2007) and that the deep pathways of water are rather erratic (Bower et al., 2009).

Such features can only be reproduced in a high resolution, eddy resolving model. Building on the preliminary results of Weijer et al. (2012), we investigate in **chapter 5** whether the characteristics of the salt advection feedback known from coarse-resolution models also apply to a strongly eddying model of the large-scale circulation.

Chapter 6 closes the thesis with an assessment of the role of thermohaline feedbacks for the large-scale circulation and an outlook on further steps of model development.

2

Scaling of the strength of the meridional overturning with vertical diffusivity in an idealized global geometry

An important expression of the nonlinear character of the ocean's meridional overturning circulation (MOC) is the scaling of its amplitude with the magnitude of the vertical mixing coefficient (diffusivity) of heat and salt. In this chapter we extend work that indicates that the Atlantic and Pacific MOC exhibit different scaling behavior. An idealized two-basin model configuration is used to study the meridional overturning circulation under restoring boundary conditions. In particular, the effects of wind forcing and the choice of the parameterization of lateral mixing are examined.

Without wind, the scaling is similar in the two basins and consistent with theoretical predictions, provided that the diffusivity is small enough. Towards higher diffusivities the scaling of the overturning diverges. With nonzero wind, the sensitivity is strongly determined by the choice of the lateral mixing scheme. In case of traditional horizontal diffusion, the scaling behavior is asymmetric due to spurious diapycnal mixing. With the Gent-McWilliams parameterization, the scaling is symmetric for the lower range of diffusivities, where results agree partly with theoretical scaling relations. In all cases considered, the pycnocline depth has the same sensitivity to diffusivity in both basins, implying that there is no universally valid relation between overturning strength and pycnocline depth.

2.1 Introduction

In this chapter, we extend the process-oriented studies of Dalan et al. (2005) and Dijkstra (2008) that show that the scaling of the strength of the Meridional Overturning Circulation (MOC) with vertical (or diapycnal) diffusivity (K_V) is different between the Pacific and Atlantic Ocean. The question of the circulation's sensitivity to K_V is rooted in the now long standing thermocline problem (Welander, 1959; Robinson and Stommel, 1959; Welander, 1971). A complete theory for the observed structure of oceanic density profiles would greatly advance our understanding of the deep circulation and its sensitivity to external parameters. It is still not clear, however, to what extent the MOC is governed by adiabatic dynamics, or, phrased differently, how important irreversible mixing is for bringing deep water to the surface (Kuhlbrodt et al., 2007).

Unfortunately, the available observational data are not yet comprehensive enough to be conclusive. Assuming that, on a global scale, the density tendency due to upwelling (vertical advection) is balanced solely by vertical mixing, a vertical diffusivity of about $1\,\mathrm{cm^2\,s^{-1}}$ is inferred from density profiles (Munk, 1966). This number is about one order of magnitude larger than the value suggested by direct measurements in the main thermocline (Ledwell et al., 1993). Mixing rates, however, have a high degree of spatial variability, with estimates for K_V ranging from $0.1\,\mathrm{cm^2\,s^{-1}}$ for the interior ocean over smooth abyssal plains to larger than $10\,\mathrm{cm^2\,s^{-1}}$ over rough topography (Toole et al., 1994; Polzin et al., 1997). The "canonical" diffusivity found by Munk (1966) may therefore be reinterpreted as a surrogate for a small number of concentrated source regions of intense mixing (Munk and Wunsch, 1998). Yet, as long as the sparsity of direct measurements precludes a direct test of this idea, studies addressing the scaling of the overturning with vertical diffusivity remain valuable.

Among the simplest three-dimensional models of the ocean are those that consider buoyancy-driven flows in an idealized North Atlantic basin. Results for this configuration have often been compared to the classical scaling laws (section 1.2; Lineikin, 1955; Robinson and Stommel, 1959; Bryan and Cox, 1967). Those are obtained by assuming that the flow is in geostrophic and hydrostatic balance and that an upwelling-diffusion balance controls the depth of the thermocline. In case of restoring surface conditions and a linear equation of state there is effectively one tracer and the classical scaling relations are given by

$$V \quad \sim \quad \frac{g\Delta\rho}{\rho_0 f L}\delta_\rho, \quad W \sim \frac{K_V}{\delta_\rho}, \quad \Psi \sim V\delta_\rho L \sim WL^2, \tag{2.1a}$$

$$\delta_\rho \quad \sim \quad \left(\frac{\rho_0 f L^2}{g}\right)^{1/3}\left(\frac{K_V}{\Delta\rho}\right)^{1/3}, \tag{2.1b}$$

$$\Psi \quad \sim \quad \left(\frac{L^4 g}{\rho_0 f}\right)^{1/3}\left(K_V^2\Delta\rho\right)^{1/3}. \tag{2.1c}$$

Here, V (W) is the characteristic horizontal (vertical) velocity, Ψ is the strength of the MOC, and δ_ρ is a measure of the pycnocline depth. In addition to K_V, the independent parameters are g, the acceleration due to gravity, $\Delta\rho$, the equator-to-pole density difference, ρ_0, a reference density, f, a characteristic value of the Coriolis parameter, and L, a characteristic horizontal length scale. Park and Bryan (2000) established a good agreement between these relations and their model results, and were able to explain the deviations from classical

scaling found in earlier studies (Bryan, 1987; Colin de Verdière, 1988; Hu, 1996; Marotzke, 1997).

In the presence of wind stress the depth scale of the main thermocline may be controlled by the Ekman pump velocity W_E. As a result, the sensitivity of the overturning circulation reduces to an approximate $K_V^{1/2}$-dependence for small vertical diffusivities (Vallis, 2000). The effect of wind may even be more profound when the basin is extended to include both hemispheres and a zonally periodic channel, as a model for the Antarctic Circumpolar Current. Because no net geostrophic transport is possible across the unblocked latitudes of Drake Passage, the wind driven surface flow may induce a large-scale deep return flow, even in the absence of vertical mixing ("Drake Passage effect"; Toggweiler and Samuels, 1998). Gnanadesikan (1999) constructed a simple model for the pycnocline that incorporates this process, as well as the partially counteracting effect of the return flow induced by mesoscale eddies. Several flow regimes predicted by the model of Gnanadesikan (1999) have been shown to occur, both in a *z*-coordinate and an isopycnal ocean model, for a double-hemispheric basin with a southern channel (Klinger et al., 2003).

As a final extension, (semi-) realistic multi-basin geometries can be considered. The sensitivity of the overturning circulation to K_V was studied in an idealized two-basin configuration by Dalan et al. (2005), using a coupled ocean-atmosphere model. Their results show that the Atlantic MOC (Ψ_A) scales with K_V with a power of 0.44, while the Southern Pacific MOC (Ψ_P) scales with a power of 0.63. The power law exponent for the Pacific overturning is thus quite close to the classical value of 2/3, but the exponent for Ψ_A is clearly smaller. More recently, Dijkstra (2008) analyzed the scaling behavior of the MOC in a fully-implicit global ocean-only model. Using restoring conditions for salinity and a simple energy balance atmospheric model to control upper ocean temperatures, he found that Ψ_A scales as $K_V^{1/3}$, whereas Ψ_P scales as $K_V^{2/3}$.

Dijkstra (2008) proposed the following tentative explanation for this asymmetry in scaling. His results suggest that the depth of the Atlantic pycnocline (δ_A) hardly changes with K_V, because it is controlled by advection, while the depth of Pacific pycnocline (δ_P) is determined by classical scaling. In addition, he argued that the connection of the Pacific and Atlantic basins through the Southern Ocean implies that there is a single characteristic horizontal velocity (V) that applies to the entire domain. Provided that V scales as $K_V^{1/3}$, the relations $\Psi_A \sim V\delta_A$ and $\Psi_P \sim V\delta_P$ result in the observed MOC scaling.

A crucial element in this idea is that the surface boundary conditions allow variations in the Atlantic surface density. With reference to Eq. (2.1), this means that $\Delta\rho$ cannot be considered an external parameter. The same implication holds for the suggestion of Dalan et al. (2005) that the difference in scaling is the result of their use of "mixed" boundary conditions.

The main goal of the present work is explore the scaling behavior of a multi-basin model for the contrasting case in which the surface density is (nearly) fixed, akin to the classical single-hemisphere experiments. The question we pose is if the difference in scaling between the Pacific and Atlantic is a robust feature of the "global" overturning that may also be caused by other factors than $\Delta\rho$ being part of the solution. The results of Wright and Stocker (1992), who used a simplified model consisting of interconnected zonally averaged ocean basins, show that the scaling can also be asymmetric when restoring boundary conditions apply for

both temperature and salinity. Here, we examine the problem in a full three-dimensional model and focus on (1) the effect of wind stress and (2) the parameterization of lateral mixing by mesoscale eddies. We simplify the problem by using a highly idealized model geometry that ignores the contrast in size and latitudinal extent between the basins of the world ocean.

As reviewed above, the presence of wind stress complicates the dynamics of the oceanic flow. We believe that by presenting the scaling behavior for the cases with and without wind we provide important links between the results already available in the literature. This is also true for exploring different parameterizations of lateral mixing, which affect the K_V-dependence through the amount of (spurious) cross-isopycnal mixing implied by the scheme of choice. Knutti et al. (2000) concluded that the scaling behavior is essentially unaffected when the horizontal mixing scheme used by Wright and Stocker (1992) is replaced by a more physical representation of mesoscale eddies, in which the isopycnal formulation of Redi (1982) is combined with the scheme of Gent and McWilliams (1990). Here, we evaluate if the same holds true if the flow has zonal structure.

In contrast to most other studies, in which only a few quasi-steady solutions are computed, the implicit model approach used by Dijkstra (2008) allows to determine scaling relations based on many exact steady solutions. Currently, an important limitation of this method is that it can only be used efficiently with horizontal tracer mixing. We therefore combine the implicit approach with traditional explicit time stepping and thus attain a more complete picture than would have been possible with each of the individual approaches.

This chapter is organized as follows. Section 2.2 contains the model formulation and an introduction to the experiments performed for this study. Section 2.3 presents the scaling results, which we analyze in more detail in section 2.4. The relevance of the results is discussed in section 2.5, followed by the conclusion in section 2.6.

2.2 Model formulation and experiments

In this section, we describe the idealized ocean model (subsection 2.1) and the methodology used to determine the scaling behavior (subsection 2.2).

2.2.1 The two-basin ocean model

We use a highly idealized geometry (Fig. 2.1a), similar in design to that of several other process-oriented studies (Marotzke and Willebrand, 1991; Von der Heydt and Dijkstra, 2007). It consists of two inter-hemispheric basins connected in the south by a zonally periodic channel. As such it captures the elementary geometrical characteristics of the World Ocean. Both basins extend from 52°S to 68°N and are 60° wide, and we hereafter refer to the left (right) basin as "Pacific" ("Atlantic") Ocean. The channel ("Southern Ocean") extends from 68°S to 52°S. The ocean has a uniform depth $D = 4500$ m except for two sills in the channel. At the sill with the Pacific (Atlantic) to its west the depth is approximately 2400 m (3400 m). The sills are introduced to slow down the simulated Antarctic Circumpolar Current, which would otherwise be unrealistically vigorous. In addition, the sill with the Pacific to its west is required to model the Drake Passage effect (Toggweiler and Samuels, 1998). We shortly address the effect of the sills on the scaling behavior in subsection 2.4.1.
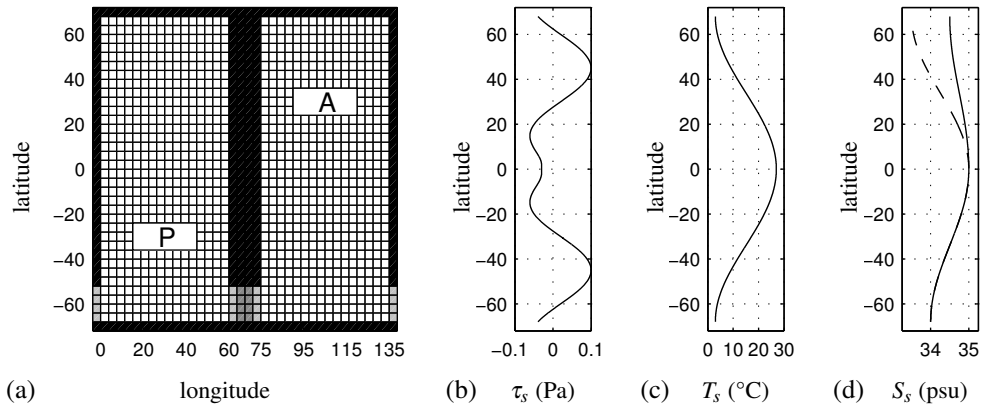
Figure 2.1: (a) Model geometry. Intersections of grid lines define velocity points on the Arakawa B grid. The shading indicates depth, where white represents 4500 m, light grey 3400 m, and dark grey 2400 m. The boxes labeled P and A indicate the regions in the Pacific and Atlantic across which the area-mean pycnocline depth is calculated. (b) Zonal wind stress. (c) Reference surface temperature. (d) Reference surface salinity in the Pacific (dashed line) and Atlantic (drawn line).

For our calculations we use two distinct numerical codes. Details will be given in section 2.2.2, where we describe the different cases that will be explored. Both programs, however, represent the same ocean model, i.e. the hydrostatic primitive equations subject to a rigid lid condition at the sea surface. The equations are expressed in pseudo-spherical (λ, ϕ, z) coordinates and discretized onto an Arakawa staggered B grid. The resolution is coarse, $3.75°$ zonally by $4°$ meridionally. In the vertical, there are 15 layers that increase in thickness from 53 m at the surface to 547 m near the bottom.

Turbulent transfer of momentum is represented by the usual second-order operator with horizontal viscosity $A_H = 2.8 \times 10^5$ m^{2}s^{-1} and vertical viscosity $A_V = 1.0 \times 10^{-3}$ m^{2}s^{-1}. Free slip conditions are prescribed at the bottom boundary, while no-slip conditions apply on the lateral walls. In the experiments where a wind stress is imposed, its zonal component is given by the idealized profile introduced by Bryan (1987, Fig. 2.1b):

$$\tau_S(\phi) = \tau_0 \Big(0.5 \big(\tanh(5\pi - 10|\phi|) + \tanh(10|\phi|) \big) - 0.8 \big(\sin(6|\phi|) + 1 \big) \Big), \qquad (2.2)$$

where $\tau_0 = 0.1$ Pa is a reference amplitude. The meridional wind stress is zero in all experiments.

There is, effectively, a single active tracer (density, ρ), which is subject to restoring boundary conditions at the sea surface. The relaxation time scale is 30 days, which ensures that deviations of the surface density from the target field remain small. The target surface density is different between the Pacific and Atlantic so as to create a typical overturning pattern with inter-basin exchange. This difference is more easily appreciated by specifying the target field in terms of temperature T and salinity S, and relating those to density through a linear equation of state,

$$\rho = \rho_0 \big(1 - \alpha_T (T - T_0) + \alpha_S (S - S_0) \big). \qquad (2.3)$$

19

Here, $\rho_0 = 1035$ kgm^{-3}, $T_0 = 15°$C and $S_0 = 15$ psu are reference quantities and $\alpha_T = 1.0 \times 10^{-4}$ K^{-1} is the thermal expansion coefficient and $\alpha_S = 7.6 \times 10^{-4}$ psu^{-1} the haline contraction coefficient. The target surface temperature (Fig. 2.1c) is a function of latitude only,

$$T_S(\phi) = 15 + 12\cos\left(\pi\frac{\phi}{\phi_N}\right), \tag{2.4}$$

where $\phi_N = 68°$N. To mimic real-world conditions, the reference surface salinity (Fig. 2.1d) is different between the Pacific and Atlantic. It is given by

$$S_S(\phi) = 35 + \chi\left(\cos\left(\pi\frac{\phi}{\phi_N}\right) - 1\right), \tag{2.5}$$

where $\chi = 0.50$ for the Southern Hemisphere, $\chi = 0.75$ for the North Pacific and $\chi = 0.25$ for the North Atlantic. This way, the forcing is sufficiently asymmetric to ensure that Northern Hemispheric deep water formation is confined to the Atlantic in all model runs. Note that the scaling behavior of the Pacific and Atlantic would be nearly identical if χ would be uniform.

We explore two different parameterizations of tracer mixing by subgrid-scale motions. The first scheme uses the traditional anisotropic Fickian diffusion along horizontal/vertical directions. In the second scheme the diffusion tensor is rotated to align the dominant diffusive fluxes along the local isopycnal directions (Redi, 1982), which eliminates the strong lateral diffusion of density. Instead, the effect of mesoscale eddies on the density field is represented by the Gent and McWilliams (1990, GM) scheme. For the horizontal, isoneutral and GM diffusivity we use $K = 1.0 \times 10^3$ m^{2}s^{-1} throughout, but the latter two are tapered to zero in regions of steep isoneutral slopes using the scaling proposed by Gerdes et al. (1991). Tracer advection is discretized with a second order centered difference scheme. Convection is parameterized by employing a strongly enhanced vertical diffusivity ($K_V^c = 1.0$ m^{2}s^{-1}) at interfaces across which the density gradient is statically unstable. Lateral walls and bottom are assumed insulating.

2.2.2 Experiments

We perform four scaling experiments that differ from each other by the use of *HOR*izontal or *GM* tracer mixing, and by the absence (-*NW*) or presence of wind stress: HOR-NW, HOR, GM-NW and GM. The HOR-NW and HOR experiments are performed with the B-grid version of the ThermoHaline Circulation Model (THCM-B; De Niet et al., 2007), which is a fully-implicit model capable of computing branches of exact steady states using continuation methods (section 1.3). The relatively low computational cost of implicit modeling allows to explore a very wide range of vertical diffusivities in an efficient manner. However, THCM-B only operates effectively when using a horizontal tracer mixing scheme.

For the GM-NW and GM experiments, in which we reevaluate the scaling behavior using the isopycnal/GM tracer mixing scheme, we therefore resort to the familiar GFDL Modular Ocean Model (MOM), version 3.1 (Pacanowski and Griffies, 2000). With MOM, (approximate) steady states are obtained by integrating forward in time until the basin averaged surface heat flux drops below 10^{-3} Wm^{-2}. The typical equilibration time is determined by the

ratio of the depth scale squared to diapycnal diffusivity, which amounts to $\mathcal{O}(10^4)$ years. Obviously, the large computational expense limits the number of equilibrium solutions that can be found. In the GM-NW and GM experiments nine points are computed with diffusivities varying over two orders of magnitude, ranging from $K_V = 0.053\,\mathrm{cm^2\,s^{-1}}$ to $K_V = 5.3\,\mathrm{cm^2\,s^{-1}}$.

2.3 Scaling behavior

In this section we focus on measures of the overturning rate Ψ and pycnocline depth δ_ρ in order to assess the scaling behavior of the circulation in the simple global geometry. The overturning rate is monitored separately for the Atlantic and Pacific by determination of the maximum (absolute value of the minimum) of the stream function in the Atlantic (Pacific). The stream function is calculated with z as a vertical coordinate. In the cases where a wind stress is imposed only the extrema occurring below a depth of 500 m are considered so that contributions from the shallow wind-driven cells are excluded.

Similar to Dijkstra (2008), the measure of the pycnocline depth is determined by calculating the depth where the difference between in-situ and surface density is equal to a fraction η of the difference between bottom and surface density:

$$\rho(z = \delta_\rho \cdot \log(1 - \eta)) - \rho_S = \eta \cdot (\rho_B - \rho_S), \tag{2.6}$$

where ρ_s (ρ_B) is the density of the surface (bottom) grid cell. The sensitivity of δ_ρ to K_V was shown to be independent of the value of η (Dijkstra, 2008) and here we choose $\eta = 0.75$. Note that the resulting depth is rescaled by $\log(1 - \eta)$, so that δ_ρ is equal to the e-folding length scale in case the density profile is exponential and $\delta_\rho/D \ll 1$. Obviously, the choice of the measure of the pycnocline depth is not unique. For example, Park and Bryan (2000) used an integral measure. However, several tests have indicated that the use of their depth scale instead of δ_ρ as defined in Eq. (2.6) does not alter our results significantly. In the following, we present area-averaged pycnocline depths for two regions (each 30° in longitude × 12° in latitude), one centered in the South Pacific and the other in the North Atlantic subtropical gyre (Fig. 2.1a).

Anticipating power law scaling behavior, the response of the solution to changing vertical diffusivity is quantified by the logarithmic sensitivity λ, which for a metric X, is defined as

$$\lambda = \frac{\partial \log X}{\partial \log K_V} = \frac{K_V}{X} \frac{\partial X}{\partial K_V}. \tag{2.7}$$

In the following "sensitivity" should be interpreted with reference to λ.

2.3.1 HOR-NW experiment

Without wind forcing ($\tau_0 = 0.0$ Pa), the structure of the overturning circulation is controlled only by the upper boundary condition for density [Eq. (2.4, 2.5)]. As shown in Fig. 2.2 for $K_V = 0.53\,\mathrm{cm^2\,s^{-1}}$, it crudely resembles the global "conveyor" circulation seen in more advanced models and is typical for this geometry (Von der Heydt and Dijkstra, 2007). The flow in the Atlantic is characterized by a net downward motion between 50°N and 68°N,
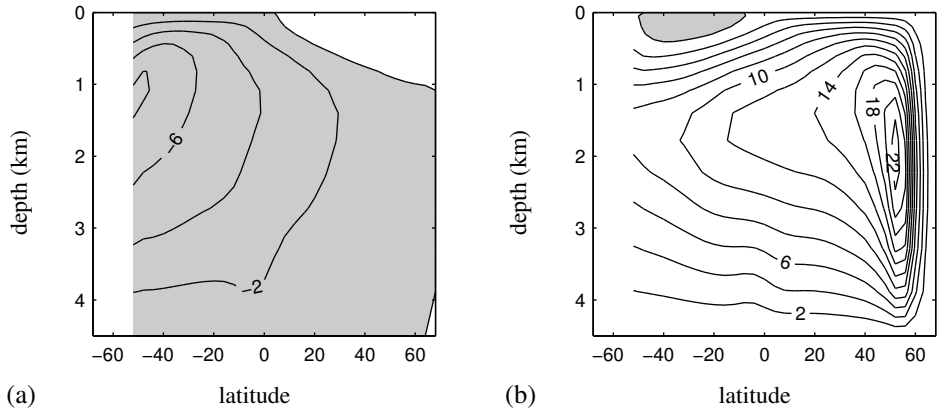
Figure 2.2: Contour plots of the (a) Pacific and (b) Atlantic meridional overturning stream functions for $K_V = 0.53\,\mathrm{cm^2\,s^{-1}}$ in the HOR-NW experiment. The contour interval is 2 Sv and shading indicates negative values.

which is compensated for by the sum of net upwelling within the basin and transport across the southern boundary. In the Pacific the zonally integrated motion is upward throughout the basin for depths below 1 km.

Using THCM-B a branch of steady states is computed for diffusivities ranging from $K_V = 0.0053\,\mathrm{cm^2\,s^{-1}}$ to $K_V = 5.3\,\mathrm{cm^2\,s^{-1}}$, i.e. K_V is varied over three orders of magnitude. In both basins the scaling behavior is close to the classical predictions for the lower range of diffusivities: the sensitivity of the overturning rates is 2/3, while the pycnocline depths show a 1/3-power law dependence (Fig. 2.3). For higher diffusivities the results deviate from these relations. The Atlantic overturning strength is clearly less sensitive for diffusivities larger than about $0.1\,\mathrm{cm^2\,s^{-1}}$ and follows an approximate 1/3-dependence for the upper range of diffusivities. Although only slightly, the scaling of the Pacific overturning rate and the pycnocline depths also depart from the classical behavior for $K_V \gtrsim 1.0\,\mathrm{cm^2 s^{-1}}$.

2.3.2 HOR experiment

Starting from a HOR-NW solution we can easily find a corresponding solution with full wind forcing by continuation in τ_0 from 0.0 to 0.1 Pa. At $K_V = 0.53\,\mathrm{cm^2\,s^{-1}}$ the result is a linear increase in the pycnocline depths, which is in contrast with the scaling relations for a single-hemispheric basin put forward by Welander (1971) and Vallis (2000) that predict a square root dependence. The Atlantic overturning strength also increases with wind strength, but without an evident relation between the two, while the Pacific overturning rate remains almost constant. The resulting overturning pattern mainly differs from that in the HOR-NW case by the presence of shallow (less than 500 m deep) Ekman cells.

Using the full wind forcing [Eq. (2.2)], we again compute a branch of steady solutions with K_V as control parameter. Fig. 2.4 shows that the scaling behavior in the HOR experiment differs significantly from that in the HOR-NW experiment. The solution's sensitivity to K_V
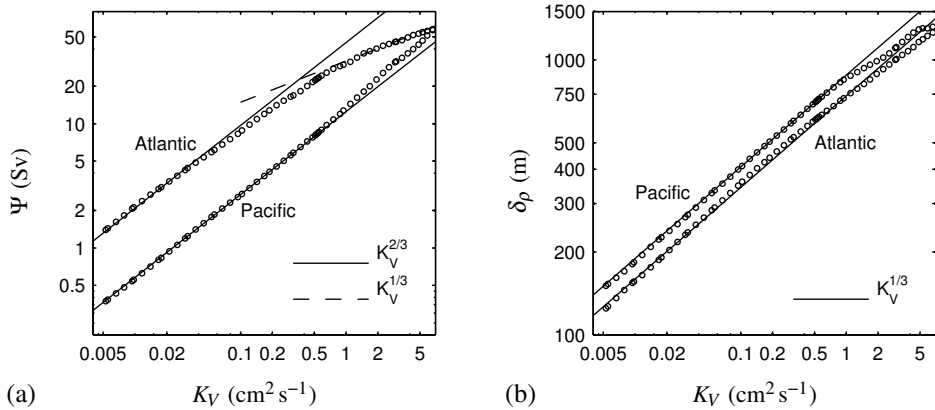
Figure 2.3: Scaling behavior in the HOR-NW experiment. Each symbol corresponds to an exact steady state obtained with THCM-B. The lines are drawn for reference only and do not correspond to regressions. (a) Overturning strength. (b) Pycnocline depth.

is very small in the lower diffusivity range. With increasing diffusivity the sensitivity of the overturning strength increases to about $1/3$ for the Atlantic and to somewhat more than $2/3$ for the Pacific. At higher diffusivities the sensitivity of the pycnocline depth is slightly larger than $1/6$ for both the Atlantic and the Pacific. So, similar to the results of Dijkstra (2008), the scaling exponents for Ψ_A and Ψ_P are different across a large part of the range of diffusivities. The sensitivity to K_V of the pycnocline depth, however, is the same in the Pacific and the Atlantic.

Anticipating the use of MOM for the GM-NW and GM experiments, we point out that results from THCM-B are consistent with results from MOM. Superimposed on the exact steady states from THCM-B, Fig. 2.4 shows four larger symbols corresponding to MOM solutions for the HOR case (for $K_V = 0.53, 0.95, 1.7$ and $3.0 \, \text{cm}^2 \, \text{s}^{-1}$). In addition to the good agreement between the results, we note that the K_V-spacing (an quarter of an order of magnitude) between the successive MOM solutions is sufficient to detect changes in the sensitivity.

2.3.3 GM-NW experiment

The typical pattern of the overturning circulation in the GM-NW experiment is presented in Fig. 2.5a-b, which shows the circulation for $K_V = 0.53 \, \text{cm}^2 \, \text{s}^{-1}$. Compared to the HOR-NW case there is a strong reduction in Eulerian-mean overturning in the North Atlantic, while the export across the southern boundary is almost unaltered (Fig. 2.5c). The change in overturning is rather small in the Pacific and therefore not shown. In addition to the Eulerian-mean overturning there is a significant eddy-induced component (Fig. 2.5d), although it is largely confined to the surface. The eddy-induced circulation is most pronounced in the Southern Ocean and in the North Atlantic.

The scaling plots for this experiment are presented in Fig. 2.6. The left panel shows the
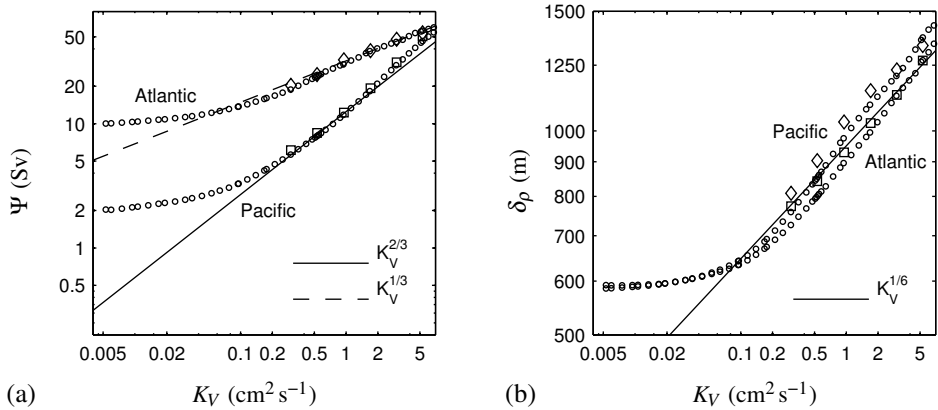
Figure 2.4: Scaling of the (a) overturning strength and (b) pycnocline depth in the HOR experiment. The small symbols represent THCM-B solutions, while the four larger symbols correspond to solutions from MOM.

overturning rate based on Eulerian-mean transports as well as with the eddy-induced component included. The Eulerian-mean and residual MOC strength are nearly identical for the Pacific. For the Atlantic the difference between the two is small, because there is no significant eddy-induced transport at the depth of maximum Eulerian-mean transport (compare Fig. 2.5b and d), and the sensitivity to changes in K_V is the same. The scaling of both overturning strength and pycnocline depth is only weakly affected by the change from the horizontal to the isopycnal/GM representation of lateral mixing. As in the HOR-NW experiment the results depart from the classical scaling relations only for the higher range of diffusivities. Yet, the diffusivity up to which classical scaling holds, appears to be higher for GM-NW than for HOR-NW.

2.3.4 GM experiment

Similar to the result in the case of horizontal mixing, comparison of GM-NW and GM solutions indicates that the presence of wind forcing leads to an increase in pycnocline depth. Except for the emergence of shallow Ekman cells, the pattern of the overturning circulation is not significantly altered. At $K_V = 0.53 \, \text{cm}^2 \, \text{s}^{-1}$ the difference between the HOR and GM solution is comparable to the difference between the HOR-NW and GM-NW solution (Fig. 2.5c). As in the GM-NW case (Fig. 2.5d), the eddy-induced circulation is most intense close to surface and mainly present in the Southern Ocean and North Atlantic.

Fig. 2.7 shows the scaling behavior for this experiment. The sensitivity to K_V of the Pacific overturning strength appears to be constant across the range of diffusivities and is somewhat larger than $2/3$. The sensitivity of the Atlantic overturning is similar for low diffusivities, but decreases as K_V increases. The pycnocline depth is again of comparable magnitude in the two basins. The sensitivity of δ_ρ to changes in K_V increases with increasing K_V, but remains clearly smaller than $1/3$. Comparison of Fig. 2.6 and Fig. 2.7 demonstrates
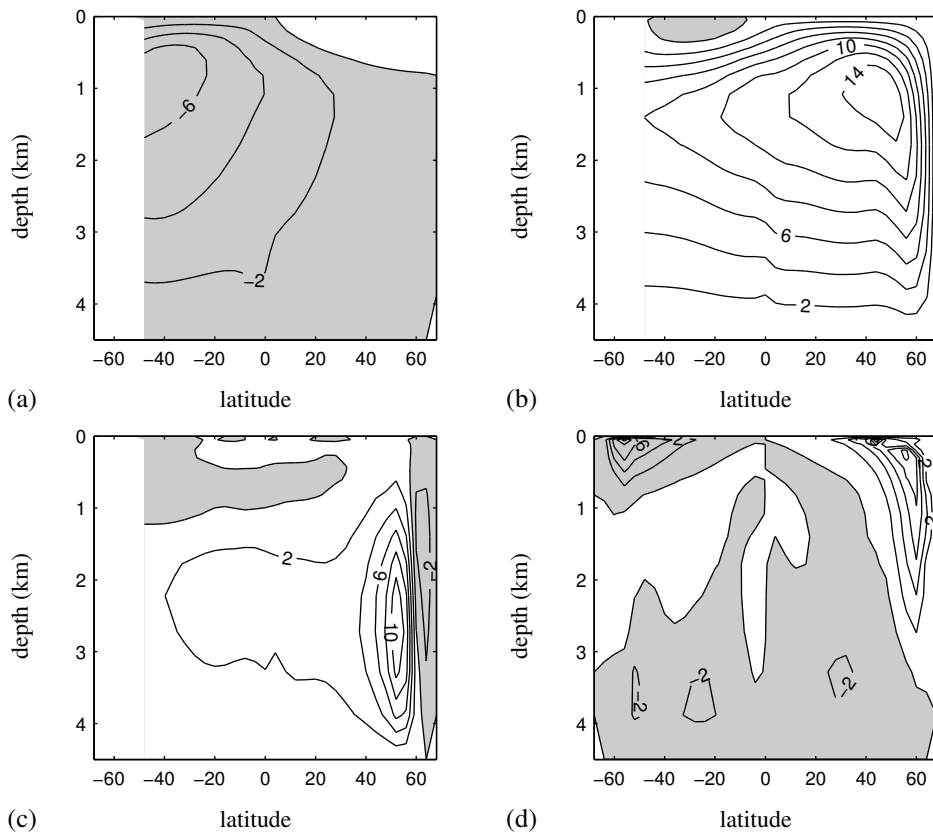
Figure 2.5: (a,b) Contour plots of the (a) Pacific and (b) Atlantic (Eulerian-mean) meridional overturning in the GM-NW experiment. (c) Difference in Atlantic meridional overturning circulation between HOR-NW and GM-NW. (d) Eddy-induced global overturning in the GM-NW experiment. All plots are for $K_V = 0.53\,\text{cm}^2\,\text{s}^{-1}$ and have a contour interval of 2 Sv.

that the scaling of the overturning strength is much less affected by the change from horizontal to isopycnal/GM mixing in absence of wind stress than in presence of wind stress. The scaling of the pycnocline depth is strongly influenced by the presence of wind for both representations of lateral mixing.

2.4 Analysis

In the following we analyze the results of section 2.3 more closely with the help of two questions: (1) What explains the departure from the classical scaling relations in the experiments without wind? and (2) Why does the representation of lateral mixing have so much impact on the scaling when wind is present?
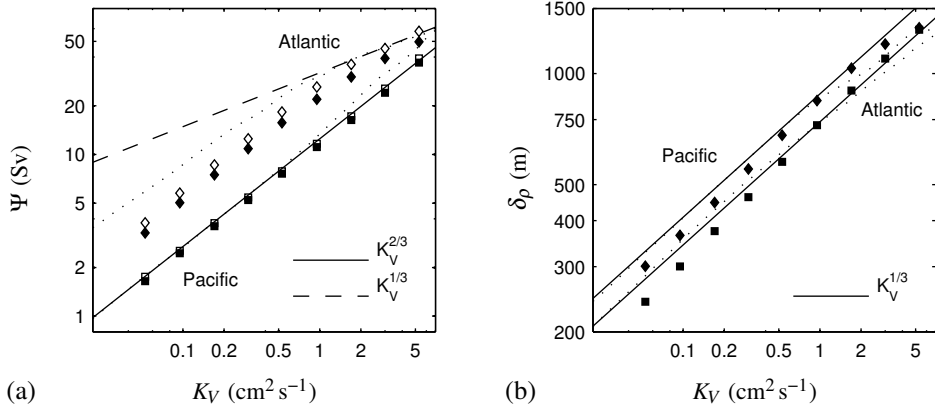
Figure 2.6: Scaling behavior in the GM-NW experiment. The symbols represent (quasi-)steady states obtained with MOM. For comparison, the dotted lines show the results from the HOR-NW experiment. (a) Eulerian-mean (solid symbols) and residual (open symbols) overturning strength. (b) Pycnocline depth.

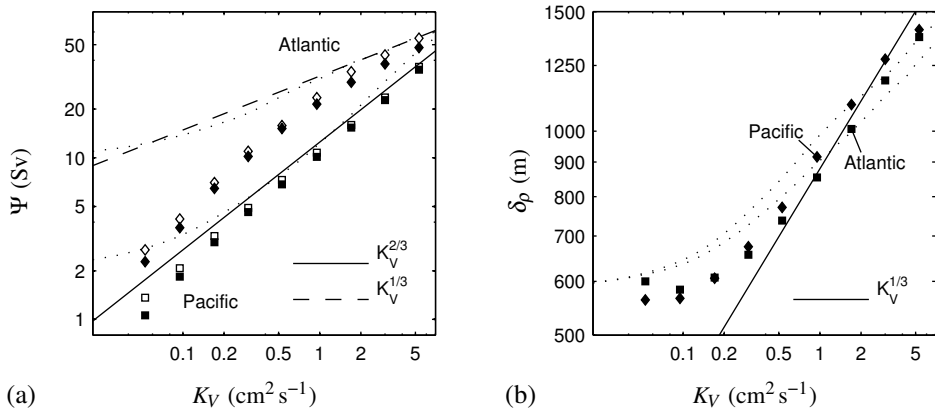*Figure 2.7:* Scaling behavior as in Fig. 2.6, but now for the GM experiment. Here, the dotted lines show the results from the HOR experiment.
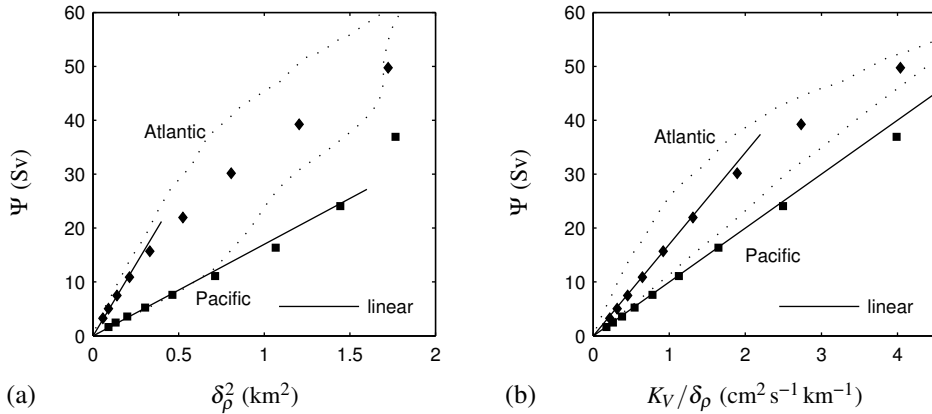
Figure 2.8: Comparison of the results of the "no wind" experiments with predictions from the (a) "thermal wind" and (b) "advection-diffusion balance" scaling relation. Dotted lines represent HOR-NW and symbols GM-NW.

2.4.1 Deviations from classical scaling in the absence of wind

The results from both the HOR-NW and GM-NW experiments indicate that, at least for larger diffusivities, the relation between overturning strength and pycnocline depth is not the same for the Pacific and Atlantic system. Two possible relations between Ψ and δ_ρ are suggested by classical scaling theory, the first expressing the thermal wind balance ($\Psi \propto \delta_\rho^2$) and the second the vertical advection-diffusion balance ($\Psi \propto K_V/\delta_\rho$). The classical scaling laws hold provided that both relations are satisfied simultaneously [Eq. (2.1)], which is indeed the case for small overturning rates (small K_V, Fig. 2.8). For higher diffusivities both relations predict stronger Atlantic overturning than observed in the model. The Pacific overturning is consistent with the advection-diffusion balance relation across the entire range of K_V, but at higher diffusivities stronger than predicted by the thermal wind relation. It is remarkable that the HOR-NW solutions for which classical scaling holds, overlap with the GM-NW solutions in the Ψ vs. δ_ρ^2-plane, but indicate a stronger derivative in the Ψ vs. $K_V\delta_\rho^{-1}$-plane. This suggests that in absence of wind the effect of spurious diapycnal mixing due to horizontal diffusion is in some sense equivalent to enhancing vertical diffusion by multiplication of K_V with a certain factor.

While it is true that (locally) the stratification is also determined by processes other than vertical advection and diffusion, the results above do not mean that the large-scale flow is no longer in geostrophic and hydrostatic balance as the scaling starts to depart from the classical relations. Instead, the "thermal wind relation" between Ψ and δ_ρ does not adequately capture that the flow is in thermal wind balance. So far, however, the analysis failed to take into account that the density contrast $\Delta\rho$ in Eq. (2.1) may depend on K_V. Even if using strong restoring conditions, slight variations in the surface density field occur due to changes in surface advection. Park and Bryan (2000) showed that the scaling behavior of single-hemispheric flows is closer to the classical relations when the results are corrected for this effect.
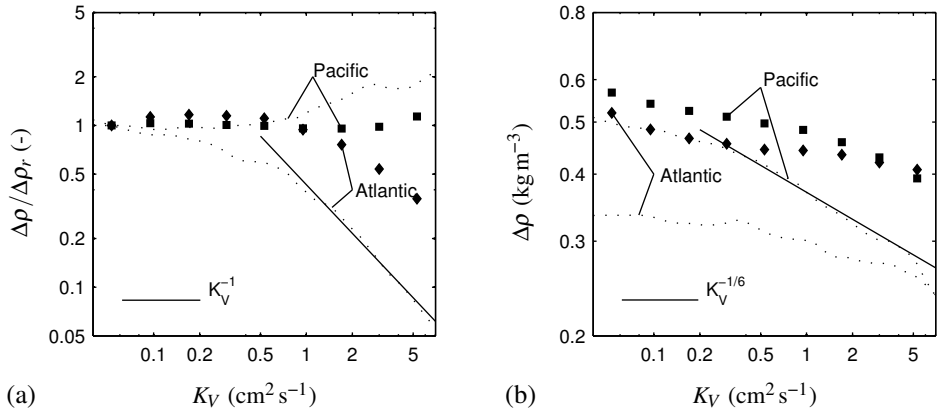
Figure 2.9: Variations in the density contrast $\Delta\rho$ in the HOR-NW (dotted lines) and GM-NW (symbols) experiments. (a) Density contrast required to account for the difference between the actual scaling of the overturning rate and the classical 2/3-dependence. The results are normalized by a reference contrast $\Delta\rho_r = \Delta\rho(K_V = 0.053 \text{ cm}^2\text{s}^{-1})$. (b) Density contrast, as determined by division of the basin-wide equatorial buoyancy transport $B^{0°}$ by the overturning strength Ψ.

We first apply this idea inversely, by calculating the variation in $\Delta\rho$ required to compensate for the departure from classical scaling. The strongest variations in the required (compensating) density contrast are found when it is calculated from the overturning strength as

$$\Delta\rho \propto \Psi^3 K_V^{-2}. \tag{2.8}$$

As expected, the Atlantic overturning rate in the HOR-NW experiment requires the largest variation in $\Delta\rho$ (Fig. 2.9a): between $K_V = 0.053$ and $5.3\,\text{cm}^2\,\text{s}^{-1}$ the density contrast should decrease by one order of magnitude to account for the departure of the scaling of Ψ_A from the classical relations. At high diffusivities the required sensitivity of $\Delta\rho$ in the Atlantic is about -1 for both HOR-NW and GM-NW. Such variations are much larger than can be realized when using strong restoring conditions. Compensation of the scaling of the Pacific overturning is only needed in the HOR-NW experiment. In that case a small positive sensitivity of $\Delta\rho$ would be required.

It is not straightforward to determine the *actual* variation in density contrast. When using the difference between section-averaged densities at two latitudes, as in Dijkstra (2008), the result is very sensitive to the choice of latitudes and the depth range over which the average is calculated. We found that a more robust measure of $\Delta\rho$ can be determined from the basin-wide meridional buoyancy transport

$$B^{\phi_S} = \iint_{\phi_S} v\rho \, \mathrm{d}\lambda\mathrm{d}z, \tag{2.9}$$

where the integral is taken across a zonal section at latitude ϕ_S. We then define the actual

density difference as the ratio of equatorial buoyancy transport and overturning strength,

$$\Delta\rho = -\frac{B^{0°}}{\Psi}. \tag{2.10}$$

The result can be thought of as the effective density contrast carried by the overturning and is plotted in Fig. 2.9b. The strongest variations in the actual density contrast are found in the HOR-NW experiment. In the Pacific $\Delta\rho$ decreases by a factor two between $K_V = 0.053$ and $5.3\,\text{cm}^2\,\text{s}^{-1}$; at high diffusivities the sensitivity is about $-1/6$. In the GM-NW experiment the sensitivities are even smaller (less negative). These results imply that only a fraction of the departure from classical scaling of the Atlantic overturning strength can be compensated for by accounting for variations in the density contrast. For the Pacific compensation by $\Delta\rho$ would even cause a stronger departure from classical scaling.

The break down of the scaling thus has a more fundamental cause. One of the assumptions in classical scaling theory is that the ocean is very deep compared to the characteristic depth scale of the stratification. Obviously, the validity of this assumption decreases as K_V increases. We therefore examine changes in the vertical structure of the flow. Fig. 2.10a shows the meridional overturning in the Atlantic at $K_V = 5.3\,\text{cm}^2\,\text{s}^{-1}$ in the GM-NW experiment. It is clear that the depth scale of the flow is increased compared to the solution at $K_V = 0.53\,\text{cm}^2\,\text{s}^{-1}$ (Fig. 2.5b). To allow a more quantitative analysis we define the flow-based depth scale δ_v as the depth where the zonally integrated velocity vanishes, i.e. the depth of maximal (in absolute sense) overturning. We calculate δ_v at 30°S in the Pacific and at 30°N in the Atlantic and compare the result to the pycnocline depth scale δ_ρ (Fig. 2.10b). In the Pacific the agreement between the two depth scales is very good, especially in the GM-NW experiment. In the Atlantic, however, there is only a linear relation between the two scales for low diffusivities, in which case the flow based depth scale is much larger than the pycnocline depth. With increasing diffusivity the increase in δ_ρ is stronger than the increase in δ_v.

The divergence of the two depth scales is associated with changes in the depth-zonal structure of the meridional velocity (Fig. 2.10c-e). For all diffusivities, the northward surface transport is carried by a strong western boundary current, while the return transport at depth is associated with weaker velocities. For small values of K_V the zonal structure of the meridional velocities is relatively simple; across the largest part of the depth range they change sign only once between west and east. With increasing diffusivities the velocity pattern deepens and the zonal structure becomes more complicated. The surface western boundary current connects with a deep patch of northward velocities, which is present to the east of the deep western boundary current. The southward velocities to the east of the surface boundary current are also part of a patch that extends to the bottom. These results suggest that the divergence of δ_ρ and δ_v in the Atlantic is symptomatic for changes in the zonal structure of the solution. Classical scaling theory, however, does not account for such changes.

When comparing the Atlantic overturning in the GM-NW experiment between $K_V = 0.53\,\text{cm}^2\,\text{s}^{-1}$ (Fig. 2.5b) and $K_V = 5.3\,\text{cm}^2\,\text{s}^{-1}$ (Fig. 2.10a), the increase in depth scale appears to be stronger in the southern part than in the northern part of the basin. As a result, the fraction (in a zonally integrated sense) of the the Atlantic deep water that is transported across the southern boundary changes as the scaling starts to deviate from the classical relations. For diffusivities up to $K_V = 0.53\,\text{cm}^2\,\text{s}^{-1}$ about 52% of the deep water is exported. This fraction decreases towards higher diffusivities and equals about 38% for $K_V = 5.3\,\text{cm}^2\,\text{s}^{-1}$. Similar
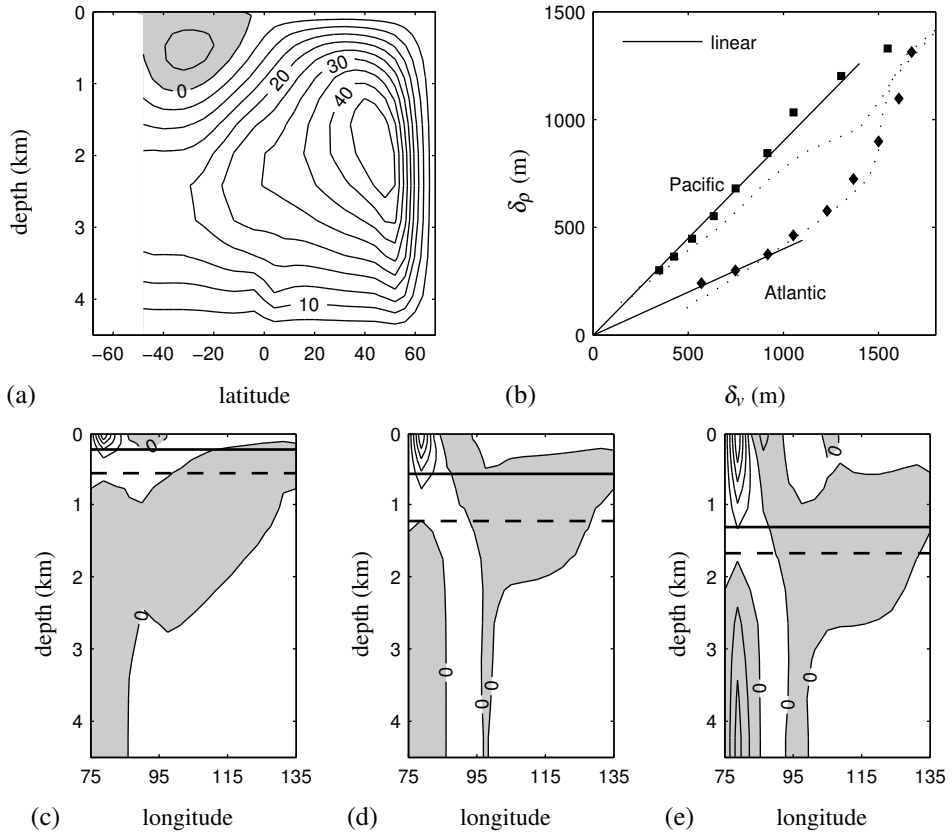
Figure 2.10: Analysis of changes in the structure of the meridional velocity. (a) Contour plot (interval 5 Sv) of the Atlantic meridional overturning for $K_V = 5.3 \, \text{cm}^2 \, \text{s}^{-1}$ in the GM-NW experiment. (b) Comparison of the flow-based depth scale δ_v to the pycnocline depth δ_ρ in the HOR-NW (dotted lines) and GM-NW (symbols) experiments. (c-e) Zonal cross-sections at 30°N of Atlantic meridional velocity for (c) $K_V = 0.053$, (d) 0.53, and (e) 5.3 $\text{cm}^2 \, \text{s}^{-1}$ in the GM-NW experiment. The velocities are normalized by the maximum value in each section. Shading indicates southward flow and the contour interval is 0.2. The drawn (dashed) line represents the level of the pycnocline depth δ_ρ (flow based depth scale δ_v).
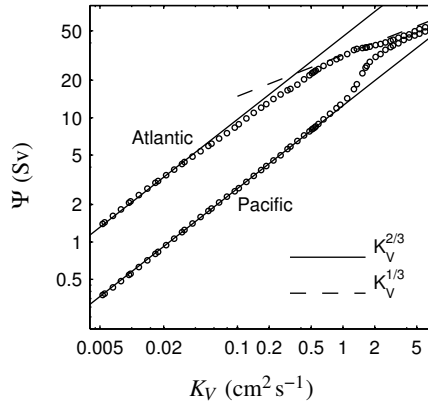
Figure 2.11: Scaling of the overturning strength in an experiment with the same configuration as HOR-NW, but without sills in the Southern Ocean.

changes occur in the HOR-NW experiment, in which the exported fraction of Atlantic deep water varies between 30% and 40% up to $K_V \approx 2\,\mathrm{cm^2\,s^{-1}}$, but decreases sharply to below 20% at $K_V = 5.3\,\mathrm{cm^2\,s^{-1}}$. In this case, there are also changes in the structure of the Pacific overturning. For diffusivities larger than about $1\,\mathrm{cm^2\,s^{-1}}$ a part of the upwelled water sinks at the southern edge of the Pacific (about 20% in a zonally integrated sense at $K_V = 5.3\,\mathrm{cm^2\,s^{-1}}$). So, in general, the inter-basin exchange tends to decrease with increasing K_V, because the typical "conveyor" circulation cannot be maintained in the diffusive limit.

A natural question is if the presence of sills in the Southern Ocean interferes with this exchange as the depth scale of the flow increases, thereby changing the scaling behavior. Using THCM-B we therefore repeat the HOR-NW experiment, but without sills. Fig. 2.11 shows that the break down of the scaling of the Atlantic overturning strength is hardly affected if the sills are removed. Yet, different from the case with sills (Fig. 2.3a), the Pacific and Atlantic overturning strength converge rapidly for diffusivities larger than about $1\,\mathrm{cm^2\,s^{-1}}$. As a result, the sensitivity of Ψ_P to changes in K_V is about $1/3$ for the highest diffusivities considered, implying that the scaling of the Pacific and Atlantic overturning strengths is again almost symmetric. In this regime, however, the export (in a zonally integrated sense) of Atlantic deep water to the Southern Ocean has vanished. The pattern of the overturning circulation is fundamentally different from the typical solutions considered so far and is characterized by a roughly equatorially symmetric circulation in each basin. The scaling being similar is therefore probably not explained by enhanced inter-basin exchange, but rather by the similarity of the circulation pattern. The departure of the pycnocline scaling from the classical $1/3$-dependence is still present in the absence of sills. So, in the HOR-NW experiment, and probably also in GM-NW, the scaling is not affected by the presence of the sills, except when approaching a regime that is irrelevant to oceanographic modeling.

2.4.2 Impact of spurious diapycnal mixing in presence of wind

In order to evaluate if parts of the classical scaling theory still hold in presence of wind stress, Fig. 2.12 presents the thermal wind and advection-diffusion relations between Ψ and δ_ρ. In contrast to the "no wind" case, the relations differ markedly between the two parameteriza-
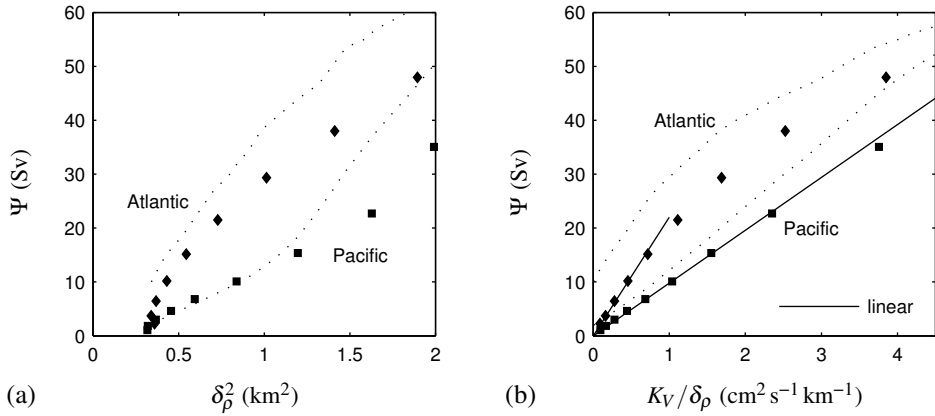
Figure 2.12: Same as Fig. 2.8, but for the experiments with nonzero wind, HOR and GM.

tions of lateral mixing, especially in the Atlantic. Before exploring this difference in more detail, let us shortly discuss the GM results. As in GM-NW, the advection-diffusion balance relation is well satisfied at all diffusivities for the Pacific, and also shows consistency for the Atlantic at low diffusivities. However, the results are inconsistent with the thermal wind relation in both basins. This finding disagrees with the thermocline theory of Gnanadesikan (1999), who assumed that the rate of deep water formation is proportional to the square of the thermocline depth.

The difference between HOR and GM is most apparent in the difference in Ψ at low diffusivities. The rather large overturning rate in HOR can be understood by inspection of the circulation pattern for $K_V = 0.0053\,\mathrm{cm}^2\,\mathrm{s}^{-1}$ (Fig. 2.13). At this diffusivity, only the Atlantic exhibits a deep basin-wide overturning circulation. In a zonally integrated sense about $10\,\mathrm{Sv}$ of deep water is formed at high latitudes. This is partly compensated for by upwelling outside the Atlantic and subsequent transport by the Ekman flow at the southern margin of the basin, but most of the upwelling takes place north of the equator and is concentrated in a narrow patch adjacent to the western boundary. This strongly suggests that the net upward motion is due to false diapycnal fluxes induced by horizontal diffusion across the sloping isopycnals of the boundary current ("Veronis effect"; Veronis, 1975). When using the isopycnal/GM formulation of lateral mixing, the western boundary upwelling does not vanish. The Veronis (1975) effect is absent, however, because the upwelling cancels exactly with its companion interior downwelling upon integration over the basin width and hence does not project onto the MOC (Lazar et al., 1999).

It is clear that the MOC scaling in the HOR experiment is strongly influenced by the incorrect representation of mixing processes. Yet, it was noted above that the spurious mixing does not preclude classical scaling behavior if the wind forcing is zero. In that case the flow is entirely buoyancy-driven. If wind is present, on the other hand, Ekman pumping additionally drives gyre circulations that are intensified close to the western boundary. Although density and wind-driven motions interact with each other, the strength of the gyres is to a certain extent independent of vertical diffusivity. We therefore hypothesize that the wind-driven cir-
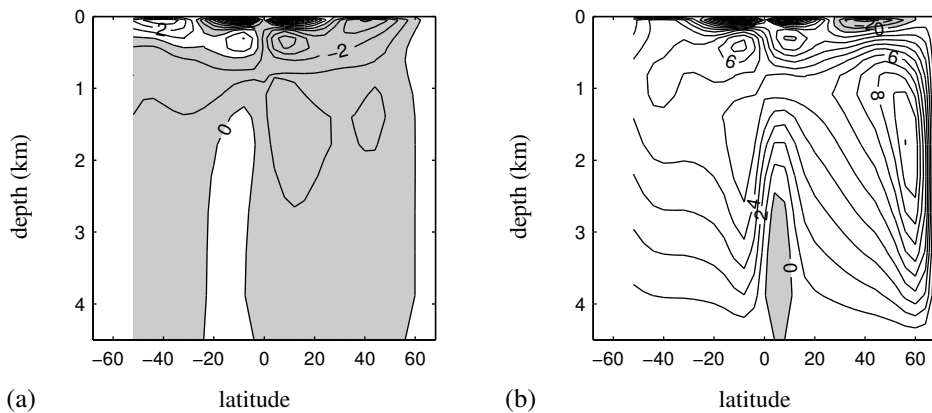
Figure 2.13: Contour plots (interval 1 Sv) of the (a) Pacific and (b) Atlantic meridional overturning for $K_V = 0.0053 \, \text{cm}^2 \, \text{s}^{-1}$ in the HOR experiment.

culation imposes additional external constraints on the density field, which prevents the effect of spurious mixing from being expressed as the equivalent of enhanced vertical diffusivity.

As an aside, we note that Fig. 2.13 also reveals another artificial feature of the circulation, which is related to the vertical resolution of the model. As demonstrated by Weaver and Sarachik (1990), the cells that occur to the north and south of the equator represent a numerical artifact that is present when the stability conditions on the vertical grid Reynolds and Péclet numbers are violated. Indeed, their amplitude diminishes with increasing K_V (decreasing Péclet number) up to about $0.015 \, \text{cm}^2 \, \text{s}^{-1}$, where their signature is no longer visible. This artifact is not seen in the HOR-NW experiment.

Additional to the differences in the scaling of the overturning strength, the sensitivity of the pycnocline depth also changes between HOR and GM. We address this point by investigating what processes determine the steady-state balance of density in the two regions where δ_ρ is calculated (Fig. 2.1). The effect of the deepening of the pycnocline with increasing K_V is visualized by presenting the results for four diffusivities ($K_V = 0.53$-$3.0 \, \text{cm}^2 \, \text{s}^{-1}$).

The density balance in the upper 1500 m is very similar in each of the four cases shown in Fig. 2.14 and 2.15. The surface balance is between horizontal (mainly meridional) advection and vertical advection induced by Ekman downwelling. Below about 500 m the contribution of horizontal advection decreases, which is accompanied by an increase in the density tendency due to lateral mixing. The latter is dominant between 1000 m and 1500 m. Within this interval the contribution of vertical advection decreases while the effect of vertical diffusion increases (both in absolute sense).

In the South Pacific (Fig. 2.14) vertical diffusion is the dominant contribution to the balance at depths below about 1500 m. In both HOR and GM it is to leading order balanced by vertical advection in the depth range between 1700 m and 3200 m. Below 3200 m, the tendency due to vertical advection decreases downward due to the no normal flow condition at the bottom. Zonal and meridional advection tend to compensate each other between 1500 m and 3000 m, but have a net effect below this depth interval (especially in HOR). It
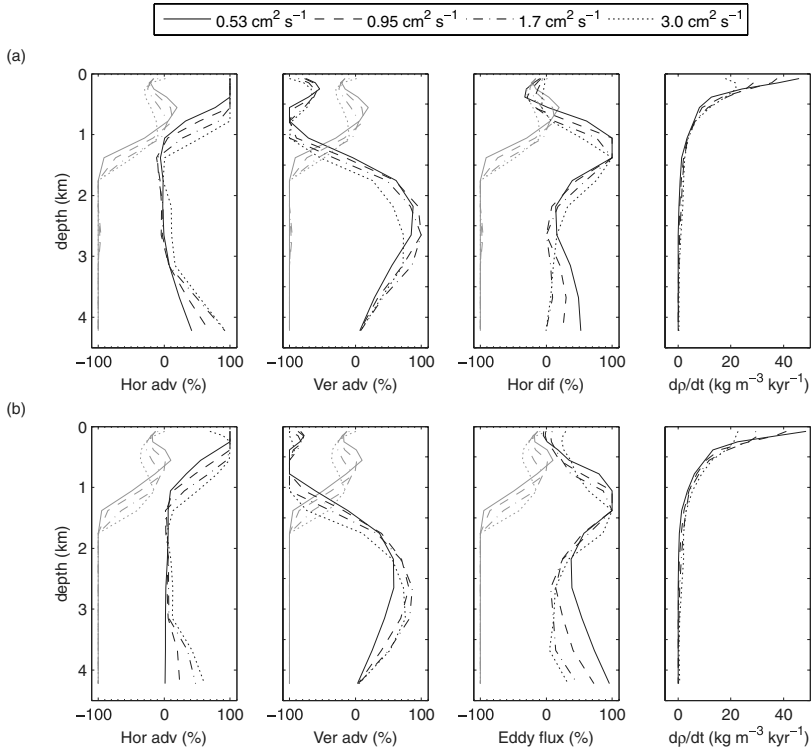
Figure 2.14: Normalized density tendencies as function of depth for the center of region P in (a) HOR and (b) GM. The line style indicates the value of the diffusivity. The contribution of vertical diffusion is shown in each of the first three panels by grey lines. From left to right the black lines represent the contributions of horizontal advection, vertical advection and (a) horizontal diffusion or (b) parameterized mesoscale eddies. Convection does not contribute to the balances in any of the results shown. The profiles are normalized at each depth by the contribution that is largest in absolute value (shown in rightmost panel). Since the total density tendency is negligible, the contributions indicated by the grey line and the three black lines sum to zero for a given depth and K_V.
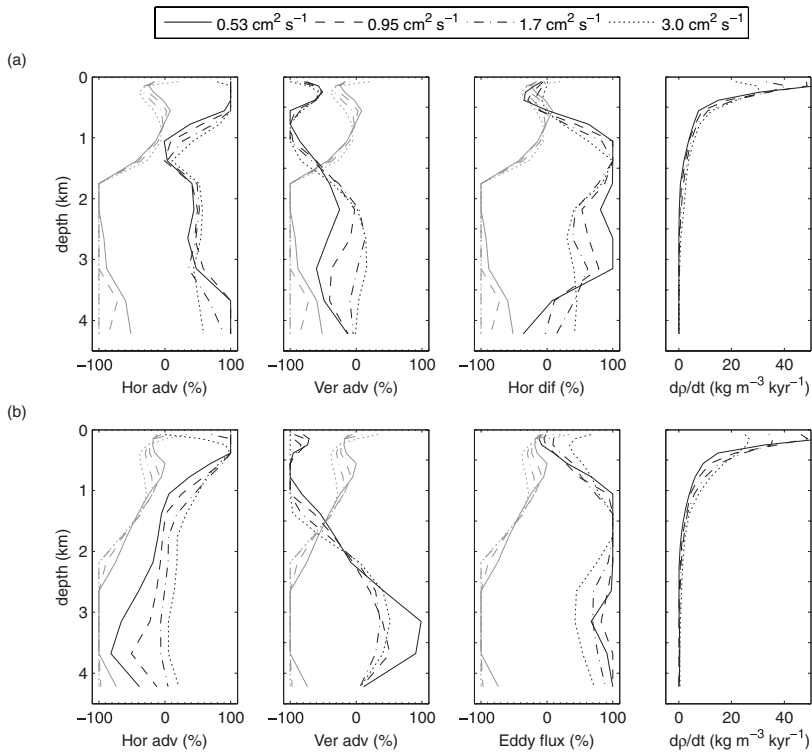
Figure 2.15: Contributions to the density tendency as in Fig. 2.14, but now for the center of region A.

is interesting to note the similarity between the profiles of horizontal diffusion in HOR and the effect of eddy stirring in GM. In both experiments the effect of lateral mixing is small in the depth range where the advection-diffusion balance dominates, especially for the higher diffusivities.

In the North Atlantic the changes in density balance (Fig. 2.15) with vertical diffusivity are more difficult to interpret. Moreover, there is a clear difference between the results from the HOR and GM experiments. In the HOR experiment vertical diffusion is dominant below about 1700 m. The contribution of vertical advection is either weakly compensating or of the same sign as vertical diffusion. The net negative tendency due to vertical advection and diffusion is balanced by both horizontal diffusion and net horizontal advection. Compared to HOR, the depth below which vertical diffusion dominates shifts downward in GM. Yet, in this case vertical advection is (weakly) compensating for all diffusivities. The dominant compensating contribution, however, is the mesoscale eddy flux, which is large at all depths below 1000 m. The dominance of the eddy contribution can be understood from the fact that the deep western boundary current, and thus the eddy activity associated with it, is particularly intense close to the source of deep water. The effect of horizontal advection is difficult to assess, due to the change in sign with increasing diffusivity. At small diffusivities, where the sign is opposite to that in the HOR experiments, the contribution appears to be non negligible.

2.5   Discussion

In this chapter, we revisited the problem of the scaling behavior of the global circulation versus vertical diffusivity. Previous studies (Wright and Stocker, 1992; Knutti et al., 2000; Dalan et al., 2005; Dijkstra, 2008) suggested that the scaling relations are different between the Pacific and Atlantic. Here, we tested the robustness of that result, using restoring conditions on density and an idealized model configuration. In particular, we evaluated if the scaling depends on (1) the presence of wind stress; and (2) the choice between horizontal or GM mixing to represent the effect of mesoscale eddies. We found that for each of the four cases considered, there is a range of diffusivities where the scaling is different between the Pacific and Atlantic.

Our results indicate that the asymmetry in scaling behavior is only manifest in the overturning rate and not in the pycnocline depth. This finding is in contrast with the results of Dijkstra (2008), who observed that the pycnocline depth in the Atlantic is less sensitive to changes in K_V than that in the Pacific. He suggested that this difference is responsible for the asymmetry in the scaling of the MOC by arguing that the ratio of Ψ and δ_ρ, which is proportional to the characteristic velocity scale V in Eq. (2.1), has the same sensitivity in both basins. Instead, the results presented here imply that the asymmetry in scaling is due to the relation between overturning rate and pycnocline depth being different for the Pacific and Atlantic.

The mechanism proposed by Dijkstra (2008) assumes that the geostrophic relation $V \propto \Delta\rho\,\delta_\rho$ [Eq. (2.1)a] holds. This means that, if the scaling of V is to be the same in both basins, while the scaling of δ_ρ differs, the typical density contrast $\Delta\rho$ is required to vary as function of K_V. Although the use of restoring conditions does not prevent changes in the typical density contrast, we demonstrated for the "no wind" case that the actual sensitivity of $\Delta\rho$ is rather

weak. This implies that the mechanism of Dijkstra (2008) cannot operate in the experiments performed in this study. Furthermore, it should be noted that the results of Dijkstra (2008) were obtained using nonzero wind and horizontal tracer mixing, i.e. the equivalent of the HOR case presented here, for which we showed that the asymmetry in the scaling of the overturning is for a large part related to the impact of spurious diapycnal mixing.

We have not been able to formulate an alternative theory that explains all aspects of the difference in scaling between Pacific and Atlantic. Yet, our results are consistent with some characteristics of the simple pycnocline model of Gnanadesikan (1999): firstly, a single depth scale is sufficient to describe the global dynamics; and secondly, the effects of southern ocean winds and eddies are important for the scaling behavior. However, the closure assumption used by Gnanadesikan (1999) for the North Atlantic Deep Water formation ($\Psi_A \propto \delta_\rho^2$) is not supported by our results from the experiments with nonzero wind (HOR and GM). At higher diffusivities the thermal wind relation also breaks down in the experiments without wind (HOR-NW and GM-NW).

Wright and Stocker (1992) suggested that a reduction in sensitivity to K_V of the Atlantic overturning compared to the predicted 2/3-dependence may be a simple consequence of the presence of deep convection, which represents an additional vertical mixing process not included in the classical scaling theory. They also noted, though, that such reduced sensitivity does not occur when a single basin is considered, despite the vicinity of a convective region. We therefore emphasize that in the configuration under study the overturning strength either measures the net upwelling (Ψ_P) or the net downwelling (Ψ_A) in a basin, rather than both up- and downwelling as in a single basin. We showed that, in all experiments, Ψ_P is accurately predicted by the scaling law that represents the vertical advection-diffusion balance. For the HOR and GM experiments we demonstrated that this result is compatible with the actual density balances. For these experiments we also showed that other processes than vertical advection and diffusion dominate the density balance in the Atlantic. Still, this only partly explains the departure from the advection-diffusion relation in the Atlantic, because Ψ_A measures downwelling, rather than upwelling. For the HOR-NW and GM-NW experiments it was noted that the fraction that upwells within the Atlantic varies with K_V, as a result of changes in the meridional velocity structure at higher diffusivities. The changes coincide with the divergence of δ_ρ and the flow-based depth scale δ_v, which for the GM-NW results was shown to be diagnostic of an increasing complexity of the zonal structure of the meridional velocity, which is not accounted for in classical scaling theory. So, the reduced sensitivity to K_V of the Atlantic overturning is probably not solely related to the presence of convection, as was put forward by Wright and Stocker (1992). Rather, we conclude that the asymmetry in scaling is the signature of a fundamental break down of the classical scaling laws.

The results from the HOR-NW and GM-NW experiments show that in absence of wind forcing the scaling is only weakly affected by the choice of the mixing scheme. This suggests that when the implicit model THCM-B (De Niet et al., 2007) is used to study the dynamics of buoyancy-driven flows, the results have validity beyond the scope of horizontal tracer mixing (to the use of which the model is presently limited). In presence of wind, however, the results become strongly influenced by the spurious cross-isopycnal mixing. This finding is in contrast with the conclusion reached by Knutti et al. (2000) on the basis of their results with a model consisting of interconnected zonally averaged basins. The difference is partly explained by the absence of the Veronis (1975) effect in two-dimensional simulations. In

addition to changes in the MOC scaling we found that the use of GM instead of horizontal diffusion results in a significant increase of the sensitivity of δ_ρ to K_V. The analysis in subsection 2.4.2 suggests that this can be attributed to changes in the processes that control the steady state balance of density in the Atlantic. In particular we note the reverse in sign of the contribution due to vertical advection.

Although the idealized two-basin formulation used here already captures several important characteristics of the real-world ocean, the scaling relations have been obtained using rather severe restrictions. To begin with, the properties of the overturning circulation considered in this work are strongly determined by the configuration. We expect the results would change if a realistic global geometry would be used, in which there is a considerable difference in relative area and latitudinal extent of the Atlantic and (Indo-)Pacific basins (Dalan et al., 2005). Our results do not allow to speculate about the effect of prescribing a strongly asymmetric geometry, but it is more likely to enhance the asymmetry in scaling than to reduce it. Another natural extension of this study would be the use of more realistic boundary conditions for temperature and salinity. In reality, these tracers interact with the atmosphere in a fundamentally different way, thus allowing the surface density field to be much stronger influenced by the flow than is possible with restoring boundary conditions. As suggested by Dalan et al. (2005), this may lead to different scaling behavior. Furthermore, with the use of more realistic boundary conditions, it would be useful to adequately relate temperature and salinity to density through a nonlinear equation of state, which would probably also affect the results. We finally note that, in reality, vertical mixing is a strongly inhomogeneous process, which is determined by mixing efficiency and energy constraints (Munk and Wunsch, 1998). By using a constant value of K_V these inhomogeneities were not adequately captured. Still, despite the relative simplicity of our model, we believe our configuration is able to provide new insights in the dynamics of the global overturning circulation, and is worth exploring further to obtain a more complete understanding of the results.

2.6   Conclusion

In summary, our results demonstrate that a difference between the Pacific and Atlantic in the scaling behavior with vertical diffusivity is not a robust feature of multi-basin overturning circulations. In absence of wind and at sufficiently low diffusivity, the scaling is in accordance with the classical scaling relations in both basins, regardless of which alternative of the mesoscale eddy parameterization is employed. Only at higher diffusivities the results start to deviate from the classical relations in such a way that the scaling of the overturning strength becomes asymmetric. In presence of wind, the choice of the mixing scheme has a large impact on the results. With horizontal mixing, the scaling is different between the Pacific and Atlantic across the entire range of diffusivities under consideration, but this can to a large degree be attributed to the effect of false diapycnal fluxes. With GM, the scaling is the same at lower values of K_V, but with increasing diffusivity the sensitivity of the overturning strength in the Atlantic is reduced compared to that in the Pacific. The scaling of the pycnocline depth is similar in the two basins, irrespective of the absence or presence of wind forcing and of the choice of the lateral mixing scheme. In contrast to previous work (Dijkstra, 2008), the occurrence of asymmetric scaling can not be explained by a simple relation

between overturning strength and pycnocline depth. The scaling behavior of the overturning in a two-basin (global) ocean model is thus much more complicated than that of buoyancy-driven flows in a single hemispheric model (Park and Bryan, 2000). Therefore, a continued systematic investigation of the processes that determine the pycnocline depth, and of its relation to the overturning strength, is needed to obtain a more complete picture of the dynamics of the global overturning circulation.

3

Spurious multiple equilibria introduced by convective adjustment

The application of bifurcation analysis to ocean climate models is substantially hampered by difficulties associated with the use of convective adjustment, i.e. a parameterization of convection in which the vertical diffusion of heat and salt is greatly enhanced whenever the water column becomes statically unstable. When tracking steady solutions of these models in parameter space, problems arise due to the occurrence of a multitude of saddle-node bifurcations, each of which is related to a minor reorganization of convection. In this chapter, the origin of the multiple steady states is analyzed in detail using a one-dimensional column model. By analytical evaluation of the eigenvalue problem conditions are formulated under which bifurcations may occur. Using numerical continuation methods a regime of multistability is identified and it is shown that the number of coexisting steady states increases with increasing resolution, while the extent of parameter space in which they occur decreases. A comparison of the numerical results to corresponding analytical solutions reveals that the multiple equilibria are inherent to the discretization and hence artificial. Apparently, successful application of convective adjustment requires knowledge of subgrid-scale tracer fields. Two alternative convective adjustment schemes are proposed that (partially) overcome these problems. Results from a fully implicit model based on the two-dimensional primitive equations indicate that the physically relevant phenomena due to the nonlinear character of large-scale oceanic flow, notably the bifurcations related to the salt advection feedback, are preserved under the alternative formulations.

3.1   Introduction

The possibility of a rapid reduction in strength of the Atlantic meridional overturning circulation (MOC) as a consequence of anthropogenic greenhouse forcing represents a crucial uncertainty in predicting the future climate (Meehl et al., 2007). Although some paleoclimatological data suggest that the last glacial period witnessed a series of major reorganizations of the Atlantic circulation (Clark et al., 2002), only with models one can assess if these are an intrinsic property of the climate system. To do so, these models need to adequately capture the relevant nonlinear behavior of the ocean circulation. In the present work we demonstrate the difficulty of faithfully representing the effect of the small-scale nonlinear process of convection in models that simulate the (Atlantic) MOC.

As discussed in section 1.2, the large-scale ocean circulation may be sensitive to perturbations of the hydrological cycle as a result of the salt advection feedback (Stommel, 1961; Bryan, 1986). It has been proposed that a similar positive feedback is associated with convection (Rahmstorf, 1999). The convective feedback was first studied by Welander (1982) and subsequently by Lenderink and Haarsma (1994) using a simple box model, consisting of a surface box that is in contact with the atmosphere, and a box representing the deep ocean, where temperature and salinity are fixed. They parameterized the effect of convection by a diffusive exchange of water properties, using a diffusivity that is small when the water in the upper box is less dense than that in the deep box, but takes a very large value in convective conditions. Welander (1982) demonstrated that the model may show spontaneous oscillations due to the system switching between convective and non-convective conditions before reaching either of the corresponding fixed points. The analysis of Lenderink and Haarsma (1994) shows that there also exist parameter regimes where the convective and the non-convective state co-exist as stable steady states. Unfortunately, we are not aware of studies that examine the relevance of the convective feedback mechanism in models that resolve the convective dynamics, nor of supporting observations.

A particularly insightful way to study feedbacks in ocean models is the application of numerical bifurcation analysis (Dijkstra and Ghil, 2005). Using special techniques (section 1.3; Seydel, 1988), it is possible to follow branches of steady states in parameter space and evaluate the linear stability of those states. These methods thus allow for a more systematic investigation of the origin of multiplicity and intrinsic variability than would be be possible with traditional time stepping. When this approach is used to study the salt advection feedback, however, its effectiveness is severely limited due to the parameterization of convection.

Oceanic convection can only be resolved numerically if a very fine horizontal resolution ($< 1 \, \mathrm{km}$) is employed (Jones and Marshall, 1993), which is not (yet) possible in models that are used to study large-scale dynamics. Without a parameterization of convection, such models may admit solutions in which statically unstable density stratification prevails, and associated flow patterns are unrealistic (Marotzke and Scott, 1999). One of the simplest remedies is to implement a scheme that causes strong vertical mixing of temperature and salinity when the stratification across an interface is unstable. This method is called *convective adjustment* (CA) and is in fact very similar to the inter-box exchange in the box model of Welander (1982) and Lenderink and Haarsma (1994). In conventional time-marching codes two different approaches are used (Marotzke, 1991): 1) complete removal of static instabilities at the end of each time step in an iterative procedure; and 2) reduction of positive density gradients

by greatly enhanced vertical diffusion. Since our interest is in numerical bifurcation analysis, for which the model equations need to be continuous in time, we focus on the second method. It should be noted, though, that the first approach can be thought of as a limit case of the second, in which the convective diffusivity tends to infinity (Schmidt and Mysak, 1996).

Convective adjustment is known to have serious deficiencies. To begin with, Hughes et al. (2009) noted that it disrupts the coupling between the evolution of basin integrated kinetic and potential energy. In addition, it falsely reduces the available potentially energy production from the surface buoyancy flux. Even if consistent energy fluxes are not required, CA may give rise to artificial model behavior due to the strong vertical coupling between grid points it implies. Cessi (1996) and Cessi and Young (1996) investigated the interaction of CA and horizontal diffusion by coupling an array of boxes similar to the "flip-flop" model of Welander (1982). They demonstrate analytically that when mixing is applied instantaneously, the scheme leads to the spontaneous emergence of the smallest resolved horizontal scale. Numerical simulations may not reveal this grid-scale instability, though, because of errors due to the finite size of the time step, or roundoff. It has been suggested that these problems may be avoided when the convective diffusivity is finite and smaller than some critical value (Cessi, 1996; Cessi and Young, 1996).

Even so, there appears to be yet another deficiency of the CA method, which is less easily perceived when using the conventional time-stepping approach. In determining bifurcation diagrams of zonally averaged ocean models using continuation methods, Vellinga (1997, Chapter 4) found a multitude of saddle-node bifurcations, despite the use of a moderate intensity of convection (corresponding to a timescale of convective mixing of about 3 years). The bifurcations were absent in the model without CA. In a further investigation of their origin, Vellinga (1998, hereafter "V98") used a one-dimensional column model with only temperature as an active tracer to study the behavior of CA in isolation. He concluded that the regular occurrence of saddle-node bifurcations does not reflect a real physical process but is caused by the way in which convection is treated in ocean models.

As will be discussed in section 3.3.2, the analysis of V98 suggests a simple workaround for the problem of spurious multiple equilibria. It turns out, however, that this solution is not effective in cases with two active tracers, temperature and salinity. This means that the analysis of V98 is incomplete. The fact that the saddle-node bifurcations due to CA are so numerous that the effectiveness of numerical continuation methods is severely compromised, is a strong motivation to reexamine the problem. We want to stress, though, that the peculiarities of CA discussed in this chapter are not unique to the steady state modeling approach, but also apply to time-stepping methods.

In the present work we extend the V98 analysis by including both temperature and salinity in his one-dimensional column model. Numerical results, in conjunction with an analytical examination of the linear stability of steady states, demonstrate that the convective feedback (Welander, 1982; Lenderink and Haarsma, 1994) operates on the grid scale. In addition, we provide analytical solutions of the model and compare them to corresponding numerical results, which allows us to firmly establish the artificial nature of the multiple equilibria associated with CA. Finally, we propose alternative formulations to eliminate, or at least reduce, their occurrence.

To illustrate the problem that motivates this study, we show in section 3.2 what the effect of CA is on the equilibria of a two-dimensional primitive equation model. The main anal-

ysis of CA using the one-dimensional column model is then presented in section 3 and the alternative CA schemes are discussed in section 4. A summary and discussion follows in section 5.

3.2 Spurious multiple equilibria in a two-dimensional ocean model

In this section, we aim to illustrate the problem of spurious multiple equilibria due to CA in a model that captures the salt advection feedback (Stommel, 1961). We therefore consider a two-dimensional (latitude/depth) configuration. Compared to the full three-dimensional case, it is much more tractable numerically, because the number of unknowns that must be solved for is typically one order of magnitude smaller. The model we use here is equivalent to the one analyzed for the case of no CA in section 3a of the paper by Weijer and Dijkstra (2001), and is very similar to the model studied by V98. We choose this particular model, because results presented in the subsequent sections of Weijer and Dijkstra (2001) demonstrate a close qualitative similarity between the bifurcation structure of two- and three-dimensional flows.

The experiments with the two-dimensional model are conducted with the B-grid version of the ThermoHaline Circulation Model (De Niet et al., 2007), which is a fully-implicit ocean-only model. It employs a pseudo-arclength continuation technique (Keller, 1977) to calculate branches of steady states, and uses the Newton-Raphson method to converge to individual solutions (section 1.3). In addition, the model implements the Jacobi-Davidson QZ method (Sleijpen and Van der Vorst, 2000) to solve eigenvalue problems. The large linear systems that arise from these techniques are solved iteratively using a tailored preconditioner, which is described in detail by De Niet et al. (2007).

3.2.1 Formulation

There are two active tracers: temperature T_* (stars indicate dimensional quantities) and salinity S_*, which are related to the density ρ_* by a linear equation of state

$$\rho_* = \rho_0 \left(1 - \alpha_T \left(T_* - T_0\right) + \alpha_S \left(S_* - S_0\right)\right), \tag{3.1}$$

where α_T and α_S are the thermal expansion and haline contraction coefficients, respectively, and ρ_0, T_0, and S_0 are reference quantities. The numerical values of these (and following) fixed model parameters are summarized in table 3.1.

In order to eliminate longitudinal dependence from the problem, we consider a purely buoyancy-driven flow on a non-rotating Earth and prescribe free-slip conditions at the lateral boundaries (which avoids the necessity of boundary layer formation). We furthermore assume that inertia can be neglected in the meridional momentum equation. The mixing of momentum and tracers due to eddies is parameterized by simple anisotropic diffusion. The equations for the meridional velocity v_*, vertical velocity w_*, pressure p_*, and the tracers T_*

Table 3.1: Fixed model parameters of the two-dimensional ocean model.

D	$=$	4.0×10^3	m	H_m	$=$	2.5×10^2	m
ϕ_N	$=$	$60°$		ρ_0	$=$	1.0×10^3	kg m^{-3}
r_0	$=$	6.371×10^6	m	T_0	$=$	15.0	°C
g	$=$	9.8	m s^{-2}	S_0	$=$	35.0	psu
A_H	$=$	2.2×10^{12}	m^2 s^{-1}	α_T	$=$	1.0×10^{-4}	K^{-1}
A_V	$=$	1.0×10^{-3}	m^2 s^{-1}	α_S	$=$	7.6×10^{-4}	psu^{-1}
K_H	$=$	1.0×10^3	m^2 s^{-1}	ε	$=$	2.0×10^3	
K_V	$=$	1.0×10^{-4}	m^2 s^{-1}	τ	$=$	75.0	days

and S_* are thus given by

$$0 = -\frac{1}{\rho_0 r_0}\frac{\partial p_*}{\partial \phi} + A_V \frac{\partial^2 v_*}{\partial z_*^2} + \frac{A_H}{r_0^2}\left(\frac{1}{\cos\phi}\frac{\partial}{\partial\phi}\left(\cos\phi\frac{\partial v_*}{\partial\phi}\right) + (1 - \tan^2\phi)\, v_*\right), \quad (3.2a)$$

$$0 = -\frac{1}{\rho_0}\frac{\partial p_*}{\partial z_*} + g\left(\alpha_T T_* - \alpha_S S_*\right), \quad (3.2b)$$

$$0 = \frac{1}{r_0\cos\phi}\frac{\partial v_*\cos\phi}{\partial\phi} + \frac{\partial w_*}{\partial z_*}, \quad (3.2c)$$

$$\frac{\partial T_*}{\partial t_*} + \frac{v_*}{r_0}\frac{\partial T_*}{\partial\phi} + w_*\frac{\partial T_*}{\partial z_*} = \frac{K_H}{r_0^2\cos\phi}\frac{\partial}{\partial\phi}\left(\cos\phi\frac{\partial T_*}{\partial\phi}\right) + K_V\frac{\partial^2 T_*}{\partial z_*^2} + \mathrm{CA}(T_*), \quad (3.2d)$$

$$\frac{\partial S_*}{\partial t_*} + \frac{v_*}{r_0}\frac{\partial S_*}{\partial\phi} + w_*\frac{\partial S_*}{\partial z_*} = \frac{K_H}{r_0^2\cos\phi}\frac{\partial}{\partial\phi}\left(\cos\phi\frac{\partial S_*}{\partial\phi}\right) + K_V\frac{\partial^2 S_*}{\partial z_*^2} + \mathrm{CA}(S_*). \quad (3.2e)$$

Here t_* is time, ϕ latitude, z_* the vertical coordinate, r_0 the radius of Earth, g the acceleration due to gravity, A_H (A_V) the horizontal (vertical) eddy viscosity, and K_H (K_V) the horizontal (vertical) eddy diffusivity. The term CA represents convective adjustment.

The equations are solved on an equatorially symmetric, flat-bottomed domain. The basin is bounded by latitudes $\phi = -\phi_N$ and $\phi = \phi_N$ and has depth D. In order to calculate transports, we assume it has a width of $64°$. The resolution is $3.75°$ in the horizontal and 250 m in the vertical. Free-slip conditions apply at the lateral walls and at the bottom. Rigid lid conditions are assumed at the surface and atmospheric pressure is neglected. The wind stress is zero everywhere, and "mixed" boundary conditions apply for temperature and salinity,

$$K_V\frac{\partial T_*}{\partial z_*} = \frac{H_m}{\tau}\left(\tilde{T}(\phi) - T_*\right) \qquad \tilde{T}(\phi) = 10.0\cos\left(\pi\phi/\phi_N\right), \quad (3.3a)$$

$$K_V\frac{\partial S_*}{\partial z_*} = S_0\tilde{Q}(\phi) \qquad \tilde{Q}(\phi) = \gamma\frac{\cos\left(\pi\phi/\phi_N\right)}{\cos\left(\phi\right)}. \quad (3.3b)$$

This formulation implies that temperatures in the upper model layer (of depth H_m) are relaxed to a prescribed profile $\tilde{T}$ at a rate τ^{-1}, while salinity is forced by a net freshwater flux $\tilde{Q}$, which is converted to an equivalent virtual salinity flux by multiplication with S_0. Although in a crude way, these equations express that ocean-atmosphere interaction affects temperature and salinity in a fundamentally different way. In the next subsection we present the results

of sensitivity experiments, in which the amplitude of the freshwater forcing γ is the control parameter.

The introduction of CA is the only change to the model analyzed in section 3a of the paper by Weijer and Dijkstra (2001). It acts solely on the tracers and is implemented as enhanced diffusion, which for a tracer C_* takes the form

$$\text{CA}(C_*) = K_V F_0 \frac{\partial}{\partial z_*} \left(\mathscr{F} \left(\frac{D}{\rho_0} \frac{\partial \rho_*}{\partial z_*} \right) \frac{\partial C_*}{\partial z_*} \right). \tag{3.4}$$

Here, F_0 is the efficiency of convection and $\mathscr{F}$ is a continuous approximation of the Heaviside step function (see Fig. 3.3),

$$\mathscr{F}(x) = \max \left(0, \tanh \left[(\varepsilon x)^3 \right] \right). \tag{3.5}$$

The steepness of the transition from 0 to 1 is determined by the selectivity ε; in the limit $\varepsilon \to \infty$ the function $\mathscr{F}$ tends to the step function. The actual value of ε is determined from experience. The use of a smooth function is required for the application of numerical bifurcation analysis, but the choice of which function is obviously not unique. We return to this issue in section 3.3.2, where we show that the shape of the function can influence the dynamical behavior of the model.

3.2.2 Results

We start with a brief recapitulation of the case without CA ($F_0 = 0$); a more extensive analysis is given in Weijer and Dijkstra (2001). The main characteristic of the model is that, as a result of the salt advection feedback (Stommel, 1961), there is a parameter regime in which equatorially asymmetric solutions exist despite the symmetry imposed by the geometry and forcing. The complex dynamical behavior of the model is best illustrated by the bifurcation diagram in Fig. 3.1a. For each value of the freshwater forcing strength γ there is a single equatorially symmetric solution, which is characterized by surface flow away from (towards) the equator for $\gamma \le (\ge)\ 0.17\,\text{myr}^{-1}$. The symmetric state is linearly stable, except for the part of the branch between the two pitchfork bifurcations at $\gamma = 0.04\,\text{myr}^{-1}$ and $\gamma = 0.35\,\text{myr}^{-1}$. The pitchfork bifurcations also connect two branches of equatorially asymmetric solutions. Each of these is linearly stable between the first pitchfork at $\gamma = 0.04\,\text{myr}^{-1}$ and the Hopf bifurcation at $\gamma = 0.44\,\text{myr}^{-1}$. At $\gamma = 0.46\,\text{myr}^{-1}$ linear stability changes again due to a saddle-node bifurcation. For a given γ the solution on one branch is the mirror image of the solution on the other branch. An example of an asymmetric solution with northward surface flow across the equator is shown in Fig. 3.1b. Evidently, the density stratification is statically unstable in a significant portion of the domain north of about 20°N.

If we start from the solution in Fig. 3.1b and increase the convective efficiency to $F_0 = 10^2$, the result is the solution shown in Fig. 3.2b. As expected, the application of CA reduces positive density gradients. The consequences are: a) steeper isopycnals in the northern part of the domain, b) increased bottom density, c) stronger stratification to the south of the overturning maximum, and d) a more vigorous meridional overturning circulation. The bifurcation diagram (Fig. 3.2a) shows that the dynamical behavior of the model is also changed due to the addition of CA. Although the overall structure is similar compared to the case without CA,
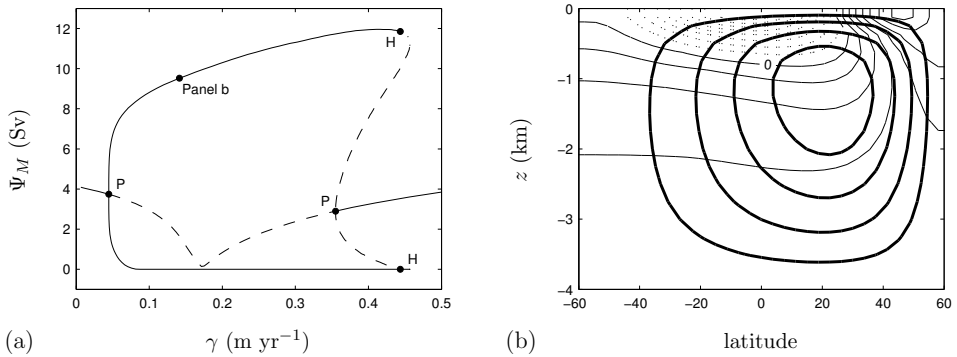
Figure 3.1: (a) Bifurcation diagram for the two-dimensional model without convective adjustment, using the freshwater forcing strength γ as control parameter. The plot shows the maximum of the meridional overturning stream function Ψ in Sverdrups ($1\,\mathrm{Sv} = 10^6\,\mathrm{m^3\,s^{-1}}$). Branches drawn as solid lines represent solutions that are linearly stable; dashed (dotted) lines indicate that one (two) of the eigenvalues is (are) positive. Pitchfork (P) and Hopf (H) bifurcations are marked in the diagram. (b) Meridional stream function (thick lines) and density relative to ρ_0 for the solution indicated in (a) by "Panel b". Contour interval is $2\,\mathrm{Sv}$ and $0.1\,\mathrm{kg\,m^{-3}}$, respectively.

a large number of additional saddle-node bifurcations has appeared, which, in the following section, will be shown to be artificial. The spurious saddle-node bifurcations define relatively narrow regions in parameter space where multiple steady states are present. Since our focus is on artificial multiple equilibria we have not calculated the linear stability of the steady states, which would have been very computationally expensive. The results of V98, however, show that apart from spurious saddle-node bifurcations, CA is also associated with complex intrinsic variability through the occurrence of numerous additional Hopf bifurcations.

3.3 Analysis

It is clear from the previous section that CA has a peculiar effect on the dynamics of simulated ocean flow, but the two-dimensional model is too complex to analyze the problem. We therefore turn to the one-dimensional column model introduced by V98, but instead of considering only temperature, we extend it to include salinity.
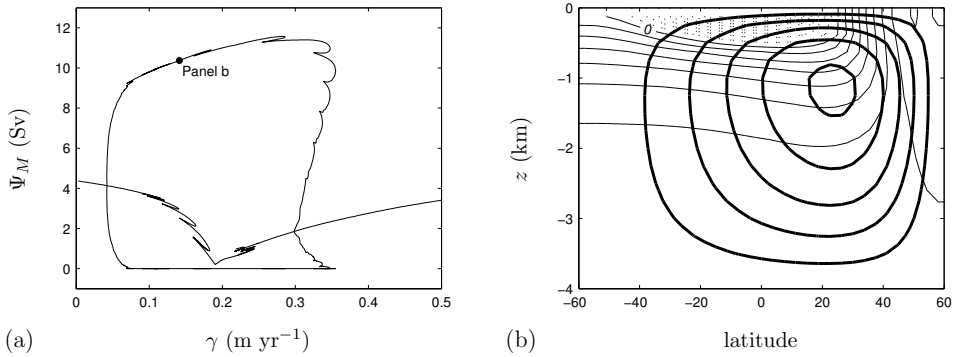
Figure 3.2: (a) Bifurcation diagram for the two-dimensional model with traditional convective adjustment and $F_0 = 10^2$. The linear stability of the steady states is not indicated. (b) Same as Fig. 3.1b.

3.3.1 Formulation of the one-dimensional model

The model consists of a column with depth D. On this domain we solve the vertical diffusion equation for the active tracers temperature and salinity:

$$\frac{\partial T_*}{\partial t_*} = K_V \frac{\partial}{\partial z_*} \left([1 + F_0 \mathscr{K}_{T_*}] \frac{\partial T_*}{\partial z_*} \right) - \kappa \left(\mathrm{i}_T^{\mathrm{res}} T_* - \tilde{T}_*(z_*) \right), \tag{3.6a}$$

$$\frac{\partial S_*}{\partial t_*} = K_V \frac{\partial}{\partial z_*} \left([1 + F_0 \mathscr{K}_{S_*}] \frac{\partial S_*}{\partial z_*} \right) - \kappa \left(\mathrm{i}_S^{\mathrm{res}} S_* - \tilde{S}_*(z_*) \right). \tag{3.6b}$$

At the surface ($z_* = 0$) and the bottom ($z_* = -D$) no-flux conditions apply. The functions $\mathscr{K}_T$ and $\mathscr{K}_S$ will be referred to as convective adjustment functions, whose form may differ between the cases considered. The forcing of the system is given by the rightmost term. For $\mathrm{i}^{\mathrm{res}} = 1$ it acts to relax the tracer to a prescribed profile at a rate κ, whereas for $\mathrm{i}^{\mathrm{res}} = 0$ it represents a fixed source of heat/salt. The density is computed from the linear equation of state given in Eq. (3.1).

The system in Eq. (3.6) is nondimensionalized by making the following substitutions:

$$t = \kappa t_*, \qquad\qquad\qquad z = D^{-1} z_*$$
$$T = \alpha_T (T_* - T_0), \qquad\qquad S = \alpha_S (S_* - S_0),$$

which gives

$$\frac{\partial T}{\partial t} = \frac{1}{P} \frac{\partial}{\partial z} \left([1 + F_0 \mathscr{K}_T] \frac{\partial T}{\partial z} \right) - \left(\mathrm{i}_T^{\mathrm{res}} T - \tilde{T}(z) \right), \tag{3.7a}$$

$$\frac{\partial S}{\partial t} = \frac{1}{P} \frac{\partial}{\partial z} \left([1 + F_0 \mathscr{K}_S] \frac{\partial S}{\partial z} \right) - \left(\mathrm{i}_S^{\mathrm{res}} S - \tilde{S}(z) \right). \tag{3.7b}$$

Here, $P = \frac{D^2 \kappa}{K_V}$, which may be interpreted as the vertical Péclet number if $\mathrm{i}^{\mathrm{res}} = 1$. With D and K_V as in table 3.1 and $\kappa^{-1} \approx 5\,\mathrm{yr}$, we get $P \equiv 10^3$. This value will be used throughout and corresponds to the "strong restoring" case considered by V98.

We use the same temperature forcing as V98,

$$\tilde{T}(z) = \cos\left(2\pi z\right),\tag{3.8}$$

which is such that it tends to stabilize (destabilize) the stratification above (below) $z = -0.5$. The salinity forcing is given by

$$\tilde{S}(z) = \gamma\cos\left(\pi z\right).\tag{3.9}$$

As in the experiments with the two-dimensional model, the salinity forcing strength γ is the control parameter for the sensitivity analysis presented in the next subsections. For negative (positive) γ the salinity forcing acts to stabilize (destabilize) the stratification in the entire column. So, by varying γ we can change the stratification. In addition, we may compare the behavior of CA in cases in which temperature and salinity gradients have an opposite effect on the density gradient to cases in which the effect is of the same sign.

In this section, we consider convective adjustment functions ($\mathcal{K}$) that only depend on the density gradient. It is therefore useful to reformulate Eqs. (3.7a) and (3.7b) in terms of density. The nondimensional form of the equation of state [Eq. (3.1)] is given by

$$\rho = \rho_0^{-1}\left(\rho_* - \rho_0\right) = S - T.\tag{3.10}$$

Because there are two independent variables in the original system (T and S), a complete description of the density evolution requires the definition of a complementary variable. It is convenient to use a quantity that is completely independent of density; we therefore define

$$\mu = S + T,\tag{3.11}$$

which is commonly referred to as "spiciness", being largest for hot and salty water (Flament, 2002). Obviously, a water mass characterized by a certain temperature and salinity may equivalently be described in terms of its density and spiciness. In a T versus S diagram the isolines of ρ and μ would appear as a set of perpendicular lines, tilted at a 45 degree angle with respect to the axes. Combining Eqs. (3.7a) and (3.7b) now gives the following alternative formulation of the problem:

$$\frac{\partial\rho}{\partial t} = \frac{1}{P}\frac{\partial}{\partial z}\left(\left[1 + F_0\mathcal{K}_\rho\right]\frac{\partial\rho}{\partial z}\right) - \left(\mathrm{i}_+^{\mathrm{res}}\rho + \mathrm{i}_-^{\mathrm{res}}\mu - \tilde{\rho}(z)\right),\tag{3.12a}$$

$$\frac{\partial\mu}{\partial t} = \frac{1}{P}\frac{\partial}{\partial z}\left(\left[1 + F_0\mathcal{K}_\mu\right]\frac{\partial\mu}{\partial z}\right) - \left(\mathrm{i}_-^{\mathrm{res}}\rho + \mathrm{i}_+^{\mathrm{res}}\mu - \tilde{\mu}(z)\right),\tag{3.12b}$$

where

$$\mathrm{i}_+^{\mathrm{res}} = \frac{\mathrm{i}_S^{\mathrm{res}} + \mathrm{i}_T^{\mathrm{res}}}{2}, \qquad\qquad \mathrm{i}_-^{\mathrm{res}} = \frac{\mathrm{i}_S^{\mathrm{res}} - \mathrm{i}_T^{\mathrm{res}}}{2},$$

and $\tilde{\rho}(z) = \tilde{S}(z) - \tilde{T}(z)$, $\tilde{\mu}(z) = \tilde{S}(z) + \tilde{T}(z)$. The transformation applied here also has other applications in oceanography. For example, it offers a meaningful way to examine the ubiquitous phenomenon of density compensation, which refers to the situation where temperature and salinity compensate in their effects on density. In that case all spatial thermohaline variability is projected onto spiciness.
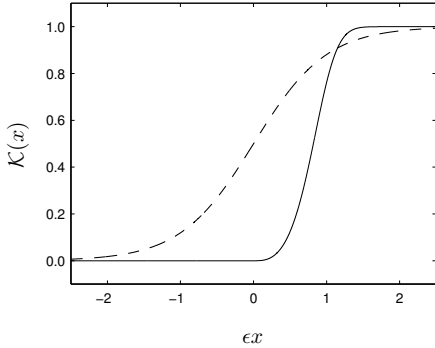
Figure 3.3: Convective adjustment functions $\mathscr{F}(x)$ (drawn) and $\mathscr{G}(x)$ (dashed).

3.3.2 The choice of convective adjustment function

Before turning to the problem of how CA introduces spurious additional multiple equilibria as in the results of section 3.2, we show why the analysis of the column model by V98 is incomplete. We therefore focus on the influence that the choice of convective adjustment function has on the model dynamics. The occurrence of bifurcations is associated with zero eigenvalues (λ) of the Jacobian matrix, which results from linearizing the model around a steady state. Hence, a central element in the analysis below is the evaluation of criteria under which zero eigenvalues can exist. In the following $\partial_z X$ means $\partial X / \partial z$.

As in V98 we consider a single active tracer (density). We therefore take $\mathrm{i}^{\mathrm{res}}_- = 0$, which means that temperature and salinity are either both relaxed towards a prescribed profile ($\mathrm{i}^{\mathrm{res}}_T = \mathrm{i}^{\mathrm{res}}_S = 1$), or both forced by a fixed source ($\mathrm{i}^{\mathrm{res}}_T = \mathrm{i}^{\mathrm{res}}_S = 0$). In both cases spiciness does not influence density, but rather adjusts passively to changes in the diffusivity implied by changes in density. Furthermore, again following V98, we define the convective adjustment functions as $\mathscr{K}_\rho = \mathscr{K}_\mu = \mathscr{G}(\partial_z \rho)$ with

$$\mathscr{G}(x) = \frac{1}{2}\left(1 + \tanh(\varepsilon x)\right). \tag{3.13}$$

The function $\mathscr{G}$ will be contrasted with the function $\mathscr{F}$ introduced in Eq. (3.5). As illustrated in Fig. 3.3 the most obvious difference between the two functions is $\mathscr{F}$ being zero for negative x, while $\mathscr{G}$ is not.

We first assume Eq. (3.12a) has a certain steady solution $\overline{\rho}$, and analyze what behavior can be expected if it is slightly perturbed: $\rho = \overline{\rho} + \Delta\rho$. After linearisation and substitution of solutions proportional to $e^{\lambda t}$ the following eigenvalue equation is found:

$$\lambda \Delta\rho = \frac{1}{P}\frac{\partial}{\partial z}\left(\left[1 + F_0\overline{\mathscr{G}} + F_0\overline{\mathscr{G}'}\frac{\partial\overline{\rho}}{\partial z}\right]\frac{\partial\Delta\rho}{\partial z}\right) - \mathrm{i}^{\mathrm{res}}_+\Delta\rho, \tag{3.14}$$

where $\overline{\mathscr{G}} = \mathscr{G}(\partial_z\overline{\rho})$ and the prime indicates differentiation. Next, we investigate whether the linear self-adjoint operator, implicitly defined in the right-hand side, is negative definite in the inner product

$$\int_{-1}^{0} \widehat{f} g \, \mathrm{d}z$$

on a space of functions $(f, g, \dots)$ for which the vertical derivative at bottom and top is zero ($\widehat{f}$ is the complex conjugate of f). The latter is equivalent to the statement that all eigenvalues of the operator are negative on the mentioned function space. Multiplying Eq. (3.14) by $\widehat{\Delta\rho}$ and integrating from $z = -1$ to $z = 0$ yields

$$\frac{1}{P} \int_{-1}^{0} \left(\left[1 + F_0\overline{\mathscr{G}} + F_0\overline{\mathscr{G}'}\frac{\partial\overline{\rho}}{\partial z} \right] \frac{\partial\widehat{\Delta\rho}}{\partial z} \frac{\partial\Delta\rho}{\partial z} \right) \mathrm{d}z = - \left(\mathrm{i}_+^{\mathrm{res}} + \lambda \right) \int_{-1}^{0} |\Delta\rho|^2 \, \mathrm{d}z, \qquad (3.15)$$

where we have used that $\partial_z\Delta\rho = 0$ at bottom and top.

Now suppose that

$$\Gamma_\rho^\rho \equiv \left[1 + F_0\overline{\mathscr{G}} + F_0\overline{\mathscr{G}'}\frac{\partial\overline{\rho}}{\partial z} \right] \geq 0 \; \forall \, z \in [-1, 0], \qquad (3.16)$$

and, additionally, that $\mathrm{i}_+^{\mathrm{res}} = 1$ (relaxation of T and S). In that case, Eq. (3.15) implies that the eigenvalues satisfy $\lambda \leq -1$, meaning that the steady state $\overline{\rho}$ is linearly stable. If instead $\mathrm{i}_+^{\mathrm{res}} = 0$ (fixed flux), density is only determined up to a constant, which results in a zero eigenvalue. This singularity is easily removed by imposing an additional integral constraint on both T and S.

So, for eigenfunctions with nonnegative eigenvalues to exist, it is required that $\Gamma_\rho^\rho < 0$ for some range of z. The only term in Γ_ρ^ρ that can be negative is $\overline{\mathscr{G}'}\partial_z\overline{\rho}$. In fact, it is negative when the stratification is stable, since $\mathscr{G}$ is a monotonically increasing function (Fig. 3.3) and hence $\overline{\mathscr{G}'}$ is always positive. Bifurcation points in this model are thus related to the following feedback: If at a certain point the stratification becomes weak, but remains statically stable, vertical diffusion is enhanced; this causes stratification to become weaker, which, in turn, results in even stronger vertical diffusion. It should be stressed that this mechanism is different from the convective feedback (Welander, 1982; Lenderink and Haarsma, 1994) discussed in the introduction. It does not depend on the presence of two active tracers (T and S), but rather is inherent to the shape of $\mathscr{G}$. In the following it will be referred to as "self-sustaining diffusion".

An analytical steady state solution of Eq. (3.12a) with $\mathscr{K} = \mathscr{G}$ is not available, so the "true" expression of the self-sustaining diffusion feedback is unknown. Therefore we turn to the discrete problem. We consider a discretization in which numerical solutions are calculated on an l-point equidistant grid, and derivatives are approximated by central differences. Repeating the steps that lead to Eq. (3.15), but now defining the inner product as a summation, leads to

$$\frac{l^2}{P} \sum_{k=1}^{l-1} \left(\left[1 + F_0\overline{\mathscr{G}}_+ + F_0\overline{\mathscr{G}'}_+ l \left(\overline{\rho}_{k+1} - \overline{\rho}_k \right) \right] \times |\Delta\rho_{k+1} - \Delta\rho_k|^2 \right) =$$

$$- \left(\mathrm{i}_+^{\mathrm{res}} + \lambda \right) \sum_{k=1}^{l} |\Delta\rho_k|^2, \quad (3.17)$$

where ρ_k is the density at level $k \in \{1, \dots, l\}$, and

$$\overline{\mathscr{G}}_+ = \mathscr{G} \left(l \left[\overline{\rho}_{k+1} - \overline{\rho}_k \right] \right).$$

Comparison of Eq. (3.15) and Eq. (3.17) shows that the latter may also be obtained directly from the former by replacing integrals withs sums and discretizing the derivatives. The feedback of self-sustaining diffusion is hence also present in the discrete model and, indeed, explains the occurrence of saddle-node bifurcations and multiple steady states in the one-dimensional model of V98 (his figures 11 and 12).

Yet, closer examination of Eq. (3.17) suggests that the stability properties of the discrete system may be different from the continuous system, and possibly depend on l. Even if the set $\overline{\rho}_k$ for $k = 1, \ldots, l$ closely resembled the (unknown) true solution at the levels of discretization, the result of the strongly nonlinear operator $\overline{\mathscr{G}}_+$ would depend on the resolution. Furthermore, the diffusion feedback may only operate at the level of the interfaces determined by the discretization. These notions form a provisional explanation for the observation of V98 that the multiplicity of steady states in a given parameter space depends on resolution.

When we contrast the function $\mathscr{G}$ with the function $\mathscr{F}$ [Eq. (3.5)] it is clear, though, that this analysis is not complete. Because $\overline{\mathscr{F}'}\partial_z\overline{\rho}$ is always nonnegative, using the latter function would eliminate the self-sustaining diffusion feedback. As a result, there would be no bifurcations (we have confirmed this for the discrete case). So, for $i^{\text{res}}_- = 0$ and using $\mathscr{F}$, we can prove that no unfavorable feedback can occur in the discrete system, where it can if we use $\mathscr{G}$. Nevertheless, we observe spurious multiple equilibria in the two-dimensional model computations using $\mathscr{F}$ (Fig. 3.2). The conclusion is therefore that it is not sufficient to consider only the case of a single active tracer ($i^{\text{res}}_- = 0$); we also have to consider the case with interaction between density and spiciness in order to understand the two-dimensional model results.

3.3.3 Mixed forcing

We examine the case of "mixed forcing" by taking $i^{\text{res}}_- \neq 0$. Furthermore, let $\mathscr{K}_\rho = \mathscr{K}_\mu = \mathscr{F}(\partial_z\rho)$. In the eigenvalue analysis we now need to include both the equations for density and spiciness and arrive at

$$
\int_{-1}^{0}\left[\frac{\Phi_\rho^\rho}{P}\frac{\partial\widehat{\Delta\rho}}{\partial z}\frac{\partial\Delta\rho}{\partial z} + \frac{\Phi_\mu^\mu}{P}\frac{\partial\widehat{\Delta\mu}}{\partial z}\frac{\partial\Delta\mu}{\partial z} + 2i^{\text{res}}_T|\Delta T|^2 + 2i^{\text{res}}_S|\Delta S|^2\right]\mathrm{d}z =
$$
$$
-\int_{-1}^{0}\left[\frac{\Phi_\rho^\mu}{P}\frac{\partial\widehat{\Delta\mu}}{\partial z}\frac{\partial\Delta\rho}{\partial z} + \lambda\left(|\Delta\rho|^2 + |\Delta\mu|^2\right)\right]\mathrm{d}z, \quad (3.18)
$$

where we used the following short-hand notations:

$$
\Phi_\rho^\rho - 1 \quad = \quad F_0\overline{\mathscr{K}_\rho} + F_0\overline{\mathscr{K}_\rho'}\frac{\partial\overline{\rho}}{\partial z} \quad = \quad F_0\overline{\mathscr{F}} + F_0\overline{\mathscr{F}'}\frac{\partial\overline{\rho}}{\partial z}, \quad (3.19a)
$$

$$
\Phi_\mu^\mu - 1 \quad = \quad F_0\overline{\mathscr{K}_\mu} \quad = \quad F_0\overline{\mathscr{F}}, \quad (3.19b)
$$

$$
\Phi_\rho^\mu \quad = \quad F_0\overline{\mathscr{K}_\mu'}\frac{\partial\overline{\mu}}{\partial z} \quad = \quad F_0\overline{\mathscr{F}'}\frac{\partial\overline{\mu}}{\partial z}. \quad (3.19c)
$$

Since $\Phi_\rho^\rho \geq 1$ and $\Phi_\mu^\mu \geq 1$, the integral on the left-hand side is nonnegative. The (real part of the) first term on the right-hand side, however, can have either sign, implying that the

eigenvalue λ is not necessarily negative. This notion is the mathematical expression of the convective feedback (Welander, 1982; Lenderink and Haarsma, 1994). It may result in the occurrence of bifurcations, even when using using $\mathscr{F}$ as convective adjustment function.

In the following, we consider the case $\mathrm{i}_T^{\mathrm{res}} = 1$ (relaxation of T) and $\mathrm{i}_S^{\mathrm{res}} = 0$ (fixed salinity source), which most closely corresponds to the situation in the real ocean. An intuitive explanation of how the convective feedback causes multiple equilibria in this case was provided by Lenderink and Haarsma (1994): Given that the temperature forcing acts to destabilize the stratification, while the salinity forcing acts to stabilize it, convection may become self-sustaining due to the fact that it has a stronger neutralizing impact on salinity than on temperature. If present, multiple equilibria are therefore expected for $\gamma < 0$ (stabilizing salinity forcing), and would be associated with a reorganization of the tracer distribution in the lower part of the column (where the temperature forcing is destabilizing).

For the discretized model we can verify this prediction, but it turns out that the bifurcation diagram is not robust to changes in resolution. Using $F_0 = 10^2$ and $\varepsilon = 10$ we perform two numerical experiments, one with with $l = 10$ (equidistant) levels, and one with $l = 20$ levels. Branches of steady states are calculated using a pseudo-arclength continuation algorithm (Keller, 1977). The linear systems are solved using the matrix division operator implemented in MATLAB. The results are shown in Fig. 3.4. The vertical axes of the bifurcation diagrams show the sum of $\mathscr{F}(\partial_z \rho)$ across all interfaces, which is a measure of the range across which convection operates. For values of γ smaller than about -4×10^{-2} solutions exist with stable stratification throughout the column, i.e. $\sum \mathscr{F} = 0$. For values of γ larger than about 1 stratification is statically unstable in the entire column, i.e. $\sum \mathscr{F} = l - 1$. The solutions on these two parts of the branch are linearly stable, while the part in between is characterized by a series of bifurcation points. For $\gamma > 0$ the bifurcations are Hopf bifurcations. Since we focus on the steady state dynamics, we have not quantitatively explored the intrinsic variability that originates from these singularities. For $\gamma < 0$ the bifurcations are saddle-nodes. When comparing the two experiments, the most striking result is that the number of bifurcations is determined by the resolution. For $l = 10$ there are 6 pairs of back-to-back saddle-nodes, while there are 12 pairs for $l = 20$. In addition, the width of the region in parameter space where multiple equilibria exist decreases with increasing resolution.

Fig. 3.5 presents the profiles of density, temperature and salinity from the experiment with $l = 20$ for two values of γ close to zero. CA acts on that part of the column where the density gradient is positive, i.e. $z < -0.375$ for $\gamma = -0.01$ and $z < -0.325$ for $\gamma = 0.01$. It is obvious that CA does not completely remove static instability: only in the limit $F_0 \to \infty$ the stratification becomes neutral. By virtue of the relatively small value of the convective efficiency ($F_0 = 10^2$) used here, the figure clearly illustrates the fact that CA has a much stronger impact on salinity than on temperature. It was explained above that multiple equilibria result from just this difference. For the discrete model it is clear, though, that the convective feedback mechanism operates on the grid scale, rather than independent of the discretization. The resulting multiple steady states are therefore artificial.

From Eq. (3.19c) one may expect that if F_0 or $\overline{\mathscr{F}'}$ is made sufficiently small, no spurious bifurcations occur. Indeed, for $l = 10$, there are no bifurcations if $F_0 < 1.41 \times 10^{-2}$, while keeping $\varepsilon = 10$, or if $\varepsilon < 7.09 \times 10^{-2}$, while keeping $F_0 = 10^2$. In both cases CA would be completely ineffective. Furthermore, even if there are no bifurcations, the number of positive excursions of the least negative eigenvalue still depends on resolution (not shown).
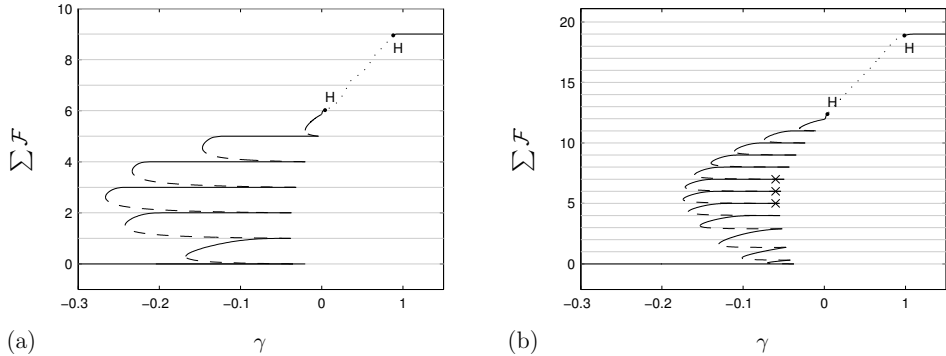
Figure 3.4: Bifurcation diagrams for the one-dimensional model with traditional convective adjustment, using the salinity forcing strength γ as control parameter (note the variation in scale on the horizontal axis). Plotted is the sum of $\mathcal{F}(\partial_z\rho)$ across all interfaces for a vertical resolution of (a) 10 layers / 9 interfaces and (b) 20 layers / 19 interfaces. Drawing conventions are as in Fig. 3.1a. The crosses in (b) indicate the solutions shown in Fig. 3.6b.

For the experiment with $l = 20$ the thresholds are only slightly larger: bifurcations disappear if $F_0 < 1.82 \times 10^{-2}$ or if $\varepsilon < 8.14 \times 10^{-2}$.

3.3.4 Analytical approach

We have shown for the discrete case that the bifurcation behavior that reflects the convective feedback, depends on resolution. Similar spurious behavior was noted by V98 regarding the self-sustaining diffusion feedback, for which case a tentative explanation could be deduced from Eq. (3.17). In case of the convective feedback, the explanation can be made more precise, because analytical steady solutions of Eq. (3.7) can be calculated, provided that the Heaviside step function is used as convective adjustment function for temperature and salinity,

$$\mathcal{K}_T = \mathcal{K}_S = \mathcal{H}\left(\frac{\partial\rho}{\partial z}\right). \tag{3.20}$$

As in the previous section, we use $F_0 = 10^2$, $i_T^{res} = 1$ and $i_S^{res} = 0$. We proceed by decoupling the intensity of convection from the stratification by introducing z_c, the shallowest level of convection, and substituting

$$\mathcal{H}\left(\frac{\partial\rho}{\partial z}\right) \to \mathcal{H}(z_c - z) \tag{3.21}$$

in Eq. (3.7). This implication is that the diffusivity equals 1 for $z > z_c$ and $1 + F_0$ for $z < z_c$. The next step is to solve the diffusion equations for both parts of the domain and to match them afterwards. The complete solution is presented in the Appendix. By combining the results for T and S, the analysis gives a solution $\rho = \rho(z, z_c, \gamma)$. Now, we consider the function
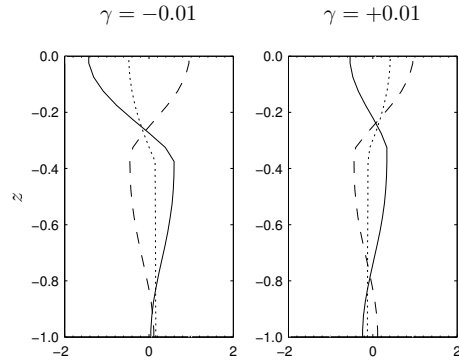
Figure 3.5: Profiles of density (drawn), temperature (dashed) and salinity (dotted) from the experiment with $l = 20$ for two values of γ. The profiles for $\gamma = -0.01$ correspond to the solution with $\sum \mathscr{F} \approx 12$.

$\partial_z \rho \left(z, z_c, \gamma\right)$ and try to find z_c such that it is positive for $z < z_c$ and negative for $z > z_c$, because only then is the substitution defined by Eq. (3.21) appropriate. In the following, such values of z_c are referred to as "consistent".

Fig. 3.6a demonstrates that consistent values of z_c exist for all values of γ, except for a window between 0.024 and 0.800. It should be noted that a solution is linearly stable for a fixed value of z_c, because the governing equations are linear. A proper analysis of the stability properties of this system would hence require considering perturbations in z_c, which turns out to be tedious. The stability indicated in Fig. 3.6a is therefore simply inferred from the fact that a change in linear stability is a generic feature of a saddle-node bifurcation. The main result of this exercise is that there is only a single pair of saddle-node bifurcations in the continuous model. These represent the "true" expression of convective feedback in the column model.

When treating this problem numerically, there are two fundamental limitations that cause multiple equilibria due to CA to be artificial. The first limitation is that z_c may only be taken from a finite discrete set of values. Mesh size convergence is only achieved if z_c equals one of the levels z_k at which the discrete tracers are calculated. For the l-point equidistant grid used in the analysis above these are given by

$$z_k = \frac{1}{l} \left(k - l - \frac{1}{2}\right) \qquad\qquad k = 1, \ldots, l. \qquad\qquad (3.22)$$

In general, the consistent value of z_c will not coincide with any z_k.

As an example, we consider $\gamma = -0.06$, in which case the consistent $z_c = -0.478$ for the convecting, linearly stable solution (Fig. 3.6a). In the experiment with $l = 20$ (Fig. 3.4b) 23 solutions were found for $\gamma = -0.06$ (of which 12 are linearly stable). Here, we focus on the three linearly stable solutions with $\sum \mathscr{F} \approx 5$, $\sum \mathscr{F} \approx 6$, and $\sum \mathscr{F} \approx 7$, respectively. In these cases the discrete density gradients are such that at each interface $\mathscr{F} \left(l \left[\rho_{k+1} - \rho_k\right]\right)$ is either 0 or 1 (due to finite computational precision), which implies that $\mathscr{F}$ could be replaced by $\mathscr{H}$ without changing the solution. In other words, the numerical solutions we examine might as well have been obtained using $\mathscr{H}$. We may also consider them as solutions of the problem in which the diffusivity is prescribed as $1 + F_0 \mathscr{H} \left(z_c - z\right)$, where $z_c = -0.725$, $z_c = -0.675$ and $z_c = -0.625$, respectively. So, in each case the value of z_c is inconsistent in the continuous case. We would therefore not like these numerical solutions, which are good
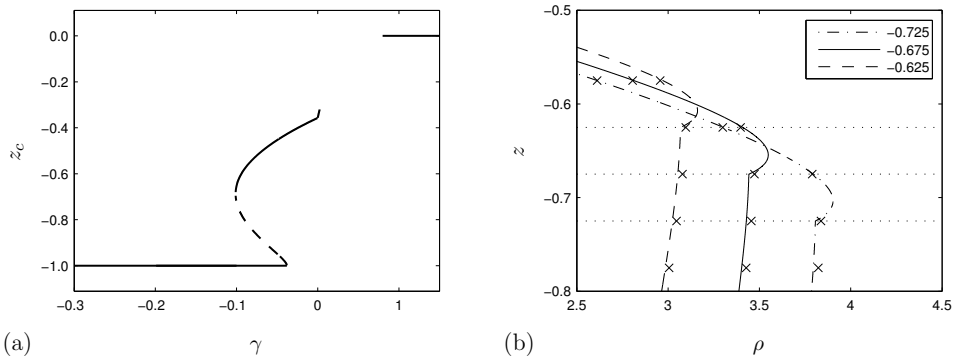
55

Figure 3.6: (a) Bifurcation diagram showing the consistent value of z_c for the analytical solution to the one-dimensional model with traditional convection. There are no consistent solutions within the interval $\gamma \in (0.024, 0.800)$. (b) Analytic density profiles for $\gamma = -0.06$, using three *inconsistent* values of z_c (indicated by horizontal dotted lines), and corresponding numerical solutions (crosses) from the experiment with $l = 20$.

approximations of the corresponding inconsistent analytical solutions (Fig. 3.6b), to exist.

Numerical solutions with inconsistent values of z_c nonetheless appear as viable solutions, which is due to the second limitation involved in the discretization of the problem: As demonstrated in Fig. 3.6b, the density gradients needed to evaluate $\mathscr{H}(\partial_z \rho)$ are not adequately resolved. The discrete derivative across the interval above $z = z_c$ is an average that does not capture the positive density gradient present in the analytical solution. In the contrary, the numerical gradient is of opposite sign. The solution is hence falsely considered consistent, which explains its existence. The multiple equilibria of the discrete model are thus completely artificial, both if $\mathscr{F}$ is used, as in subsection 3.3.3 (Fig. 3.4), as well as if $\mathscr{H}$ is used, as in conventional ocean models. Note, though, that only in the former case the spurious multiple steady states are connected through branches of linearly unstable solutions.

Increasing the resolution might seem to mitigate the problem, as such would improve the discrete estimates of continuous derivatives. Indeed, it leads to a reduction in the range of γ across which the spurious solutions are possible. Our results suggest, however, that the correct linear stability properties are only found in the continuous limit. This would imply that the convective feedback cannot be captured by a discrete model that uses CA.

3.4 Eliminating the spurious multiple equilibria

In the previous section we established that the numerous multiple equilibria associated with CA arise due to a model artifact. Although we believe this to be a fundamental problem, in this section we seek to establish a pragmatic remedy: the aim is to be able to apply a form of CA without severely diminishing the effectiveness of implicit modeling. Two alternative CA formulations are proposed in which the spurious model behavior is eliminated, or at least reduced. The new schemes result from modifications to the traditional CA scheme that are
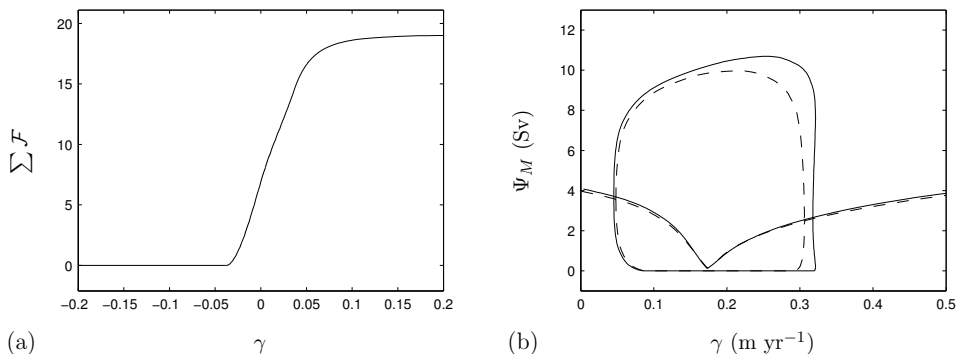
Figure 3.7: Bifurcation diagram for the (a) one-dimensional and (b) two-dimensional model with density mixing. In (b) linear stability is not indicated; the solid line corresponds to $F_0 = 10^2$ and the dashed line to $F_0 = 10^5$.

motivated by the results of the previous section. By implementing the alternative formulations in the two-dimensional model of section 3.2, we assess the impact they have on the large-scale dynamical behavior.

3.4.1 Density mixing

We first investigate a scheme in which multiple equilibria are absent by definition. It was shown in section 3.3.3 that positive eigenvalues are caused by the interaction of density and spiciness gradients. This interaction can be eliminated by choosing

$$\mathscr{K}_\rho = \mathscr{F}\left(\frac{\partial \rho}{\partial z}\right), \qquad\qquad \mathscr{K}_\mu = 0, \qquad\qquad (3.23)$$

in which case Eq. (3.19b, c) would change to $\Phi_\mu^\mu = 1$ and $\Phi_\rho^\mu = 0$. As a result, the eigenvalues λ of the one-dimensional column model are always negative [Eq. (3.18)]. Qualitatively, this formulation implies that density is affected by convection, while spiciness is not. This approach is therefore called "density mixing". We repeat the $l = 20$ experiment of section 3.3.3 to find that the resulting solution branch is indeed free of bifurcations (Fig. 3.7a). The spurious additional multiple equilibria introduced by traditional CA also disappear from the two-dimensional model results (Fig. 3.7b). Yet, the two pitchfork bifurcations, which are the signature of the large-scale salt advection feedback, are maintained. It is even possible to create the bifurcation diagram for very efficient convection, $F_0 = 10^5$, without running into computational problems.

However, these benefits come at a cost. The main disadvantage of this scheme is most easily illustrated by the equations for temperature and salinity in the one-dimensional model,
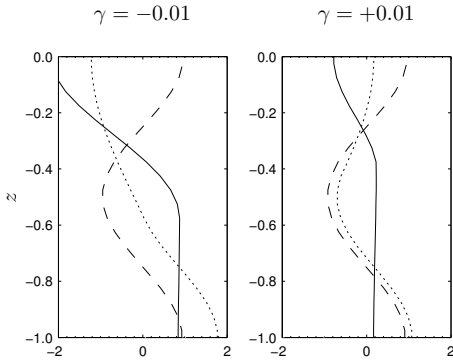
Figure 3.8: Same as Fig. 3.5, but for density mixing.

which are given by

$$\frac{\partial T}{\partial t} = \frac{1}{P}\frac{\partial^2 T}{\partial z^2} + \frac{F_0}{2P}\frac{\partial}{\partial z}\left(\mathscr{F}\left(\frac{\partial \rho}{\partial z}\right) \times \left[\frac{\partial T}{\partial z} - \frac{\partial S}{\partial z}\right]\right) - \left(\mathrm{i}_T^{\mathrm{res}} T - \tilde{T}(z)\right), \tag{3.24a}$$

$$\frac{\partial S}{\partial t} = \frac{1}{P}\frac{\partial^2 S}{\partial z^2} + \frac{F_0}{2P}\frac{\partial}{\partial z}\left(\mathscr{F}\left(\frac{\partial \rho}{\partial z}\right) \times \left[\frac{\partial S}{\partial z} - \frac{\partial T}{\partial z}\right]\right) - \left(\mathrm{i}_S^{\mathrm{res}} S - \tilde{S}(z)\right). \tag{3.24b}$$

It is clear that gradients in a tracer are created due to density mixing, even if that tracer is unforced. For example, if $\tilde{S}(z) = 0$, the solution of Eq. (3.24b) is different from $S(z) = 0$. Fig. 3.8, which may be compared to Fig. 3.5, illustrates this point for $\mathrm{i}_T^{\mathrm{res}} = 1$, $\mathrm{i}_S^{\mathrm{res}} = 0$. In comparison to the traditional formulation the (positive) density gradient in the part of the column with active CA is rather weak, which is achieved by mutual compensation of temperature and salinity gradients, i.e. $\partial_z T \approx \partial_z S \approx \partial_z \mu / 2$. The specified forcing allows salinity to be affected much stronger by CA than temperature. The creation of gradients due to density mixing is thus most apparent in the salinity profile.

3.4.2 Conditional mixing

The second alternative formulation is based on a partial disruption of the feedback that causes the multiple equilibria. By choosing the convective adjustment function for temperature and salinity as

$$\mathscr{K}_T = \mathscr{F}\left(\frac{\partial \rho}{\partial z}\right) \times \mathscr{F}\left(-\frac{\partial T}{\partial z}\right), \qquad \mathscr{K}_S = \mathscr{F}\left(\frac{\partial \rho}{\partial z}\right) \times \mathscr{F}\left(\frac{\partial S}{\partial z}\right), \tag{3.25}$$

convection only operates on a tracer if both the tracer and the density stratification are statically unstable. This approach is therefore coined "conditional mixing". Unlike density mixing, this form of CA cannot by itself generate a gradient in a tracer profile. In the one-dimensional experiment of section 3.3.3 the salinity stratification is statically stable across the entire depth range for $\gamma < 0$. Conditional mixing then results in $\mathscr{K}_S = 0$, which implies that convection cannot become self-sustaining. For $\gamma > 0$ the region of convection expands across the upper part of the domain, where temperature is stably stratified and thus unaffected
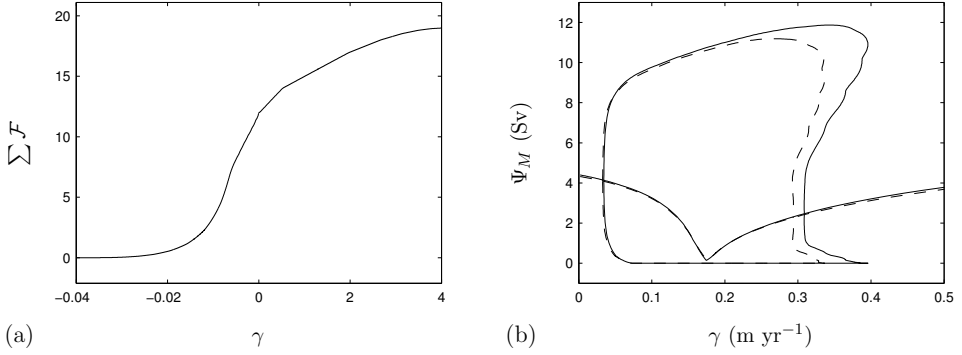
Figure 3.9: Same as Fig. 3.7, but for conditional mixing. Note the variation in scale on the horizontal axis of the plot in panel a.

by CA. There is hence also no interaction between temperature and salinity for positive salinity forcing. Fig. 3.9a shows that the bifurcation diagram is indeed free of bifurcations, while Fig. 3.10 illustrates how conditional mixing affects the tracer profiles.

If the forcing or model parameters are modified, however, the absence of singularities cannot be guaranteed. Applying the analysis demonstrated in section 3.3.2 leads to

$$\int_{-1}^{0} \left(\frac{\Upsilon_T^T}{P} \frac{\partial \widehat{\Delta T}}{\partial z} \frac{\partial \Delta T}{\partial z} + i_T^{\text{res}} |\Delta T|^2 \right) dz = - \int_{-1}^{0} \left(\frac{\Upsilon_S^T}{P} \frac{\partial \widehat{\Delta T}}{\partial z} \frac{\partial \Delta S}{\partial z} + \lambda |\Delta T|^2 \right) dz \qquad (3.26)$$

for the temperature equation [Eq. (3.7a)] and to

$$\int_{-1}^{0} \left(\frac{\Upsilon_S^S}{P} \frac{\partial \widehat{\Delta S}}{\partial z} \frac{\partial \Delta S}{\partial z} + i_S^{\text{res}} |\Delta S|^2 \right) dz = - \int_{-1}^{0} \left(\frac{\Upsilon_T^S}{P} \frac{\partial \widehat{\Delta S}}{\partial z} \frac{\partial \Delta T}{\partial z} + \lambda |\Delta S|^2 \right) dz \qquad (3.27)$$

for the salinity equation [Eq. (3.7b)], where we used the following definitions:

$$\Upsilon_T^T = 1 - F_0 \mathscr{F}'(\partial_z \overline{\rho}) \mathscr{F}(-\partial_z \overline{T}) \partial_z \overline{T} + \\ F_0 \mathscr{F}(\partial_z \overline{\rho}) \left(\mathscr{F}(-\partial_z \overline{T}) - \mathscr{F}'(-\partial_z \overline{T}) \partial_z \overline{T} \right), \qquad (3.28a)$$

$$\Upsilon_S^S = 1 + F_0 \mathscr{F}'(\partial_z \overline{\rho}) \mathscr{F}(\partial_z \overline{S}) \partial_z \overline{S} + \\ F_0 \mathscr{F}(\partial_z \overline{\rho}) \left(\mathscr{F}(\partial_z \overline{S}) + \mathscr{F}'(\partial_z \overline{S}) \partial_z \overline{S} \right), \qquad (3.28b)$$

$$\Upsilon_S^T = F_0 \mathscr{F}'(\partial_z \overline{\rho}) \mathscr{F}(-\partial_z \overline{T}) \partial_z \overline{T}, \qquad (3.28c)$$

$$\Upsilon_T^S = -F_0 \mathscr{F}'(\partial_z \overline{\rho}) \mathscr{F}(\partial_z \overline{S}) \partial_z \overline{S}. \qquad (3.28d)$$

Because $\Upsilon_T^T \geq 0$, the integral on the left-hand side of Eq. (3.26) is always nonnegative. So, this relation only allows eigenvalues to be nonnegative if $\Delta T = 0$ or if $\Upsilon_S^T \partial_z \Delta S$ is nonzero for some range $z \in Z_T$. If the first condition holds, Eq. (3.27) implies $\lambda < -i_S^{\text{res}}$, because $\Upsilon_S^S \geq 0$. So nonnegative eigenvalues are only possible if the second condition is satisfied. Hence, ΔS must be nonzero, which through Eq. (3.27) leads to the condition that Υ_T^S must be
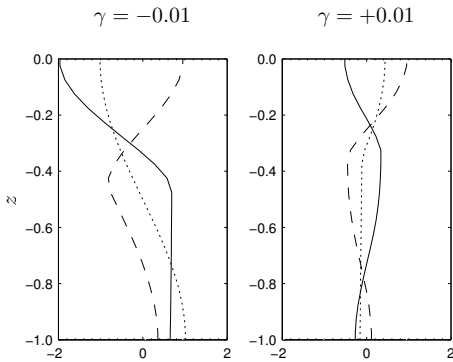
Figure 3.10: Same as Fig. 3.5 and Fig. 3.8, but for conditional mixing.

nonzero for some range $z \in Z_S$. In summary, for eigenvalues to be nonnegative it is required that Υ_S^T is nonzero for some $z \in Z_T$ *and* that Υ_T^S is nonzero for some $z \in Z_S$, where Z_T and Z_S are not empty. This condition is more restrictive than that for traditional CA, in which case $\overline{\mathcal{F}'}\partial_z\overline{\mu}$ must be nonzero for nonnegative eigenvalues to be possible. Nonetheless, although the condition is not satisfied for any γ in the problem of section 3.3.3, it may well be in general, as illustrated by the two-dimensional model results.

As with density mixing, the two-dimensional model operates without computational difficulties, even for $F_0 = 10^5$. In addition, the bifurcation diagram (Fig. 3.9b) shows that the large-scale dynamics are not affected qualitatively by conditional mixing. Different from the density mixing case, saddle-node bifurcations occur along the branches of the equatorially asymmetric solutions, but only on the parts where γ is larger than about $0.28\,\mathrm{myr}^{-1}$. Compared to traditional CA there are clearly less singularities, and those that are present do not raise computational problems.

3.5   Summary and Discussion

In this chapter, we reexamined the origin of the multiple equilibria in ocean-climate models that arise due to convective adjustment. Their occurrence presents a challenge to the application of numerical bifurcation analysis in these models. The problem was first illustrated in a fully-implicit two-dimensional primitive equation model. By varying the strength of the surface virtual salt flux, a multitude of saddle-node bifurcations was shown to occur (Fig. 3.2a). Next, the origin of these bifurcations was analyzed in detail using the one-dimensional column model introduced by V98, but extended in this study to include both temperature and salinity. A regime of multiple equilibria was identified and it was demonstrated that the number of coexisting steady states increases with increasing resolution, while the extent of the parameter space in which they occur decreases (Fig. 3.4). By comparing numerical and analytical results, we showed that the multiple equilibria are inherent to discretization of CA and therefore artificial (Fig. 3.6b). Finally, we proposed two alternative formulations of CA and demonstrated that these can be used as a pragmatic solution to the difficulty of applying CA in implicit models.

It should be emphasized that the extension of the column model of V98 to include two

tracers is necessary to fully understand the problem of artificial multiple equilibria. By analytically establishing the conditions required for the existence of zero eigenvalues of the Jacobian matrix (which implies bifurcations), we found two different feedback mechanisms that may be responsible for multiple equilibria. V98 only captured the feedback of self-sustaining diffusion, which may occur if there is sub-critical mixing for weakly stable stratification. We eliminated this mechanism by choosing a convective adjustment function in which there is no sub-critical mixing. This allowed us to focus on the nonlinear interaction of density and spiciness gradients that occurs due to the asymmetry in temperature (damping) and salinity (no damping) forcing. The associated feedback mechanism was discussed before by Lenderink and Haarsma (1994) and is also present in the simple box model of Welander (1982). In contrast to these studies, our results indicate that there is no meaningful way to capture this feedback in a discrete model by using CA, despite its possible relevance in the real world.

Our results suggest a close correspondence between the behavior of CA in the two-dimensional model and the column model. For example, we demonstrated analytically that multiple equilibria can be eliminated from the column model by density mixing, and showed numerically that also no spurious saddle-nodes occur due to CA when using this scheme in the two-dimensional model. This strongly suggests that the additional multiple equilibria in the two-dimensional model with traditional convection are solely due to the parameterization and are not induced by a response of resolved processes on changes in density caused by CA.

Still, it should be kept in mind that the one-dimensional model cannot be perceived as representing a column from a full ocean model. Rather, it allows to evaluate the properties of CA in a controlled way. We specifically note that the forcing was distributed along the entire column, instead of specified as boundary conditions at the top. In the latter case, the forcing would also have influenced the temperature and salinity across the full depth range, but only in an uncontrolled manner. Furthermore, conditions in the ocean model may correspond to other parameter values and forcing functions than used in the above, which were merely chosen such as to clearly illustrate the problems of CA.

The asset of the coarse-resolution (non eddy-permitting) modeling approach is that it allows to study the dynamical processes that might become obscured when, as a result of higher resolution, simulations on centennial to millennial timescales become computationally inaccessible. We believe that the relevance of the alternative CA formulations presented in section 3.4 should be assessed from this point of view. Both schemes help to realize a density field that respects the physical requirement that no static instabilities should be present at large spatial or temporal scales. At the same time they facilitate the use of numerical continuation techniques in coarse-resolution ocean models by avoiding (density mixing) or reducing (conditional mixing) the occurrence of artificial multiple equilibria.

The alternative schemes are not meant to faithfully reproduce the water mass characteristics seen in convective areas in the ocean - although the performance of traditional CA is probably not superior in this respect. Therefore, no attempt was made to compare the action of these schemes with data or high-resolution model output. It should be noted, though, that the fact that traditional, density and conditional mixing generate different temperature and salinity profiles, implies that large-scale dynamics are affected differently by these schemes. In the context of the two-dimensional model, this is clear from comparison of the (overall) bifurcation structure presented in Figs. 3.2a, 3.7b, and 3.9b. It is not straightforward to explain exactly how any of the different forms of CA deforms a bifurcation diagram. The bifurcation

behavior due to the salt advection feedback (Stommel, 1961), however, is qualitatively the same for different CA schemes.

It remains to be explored if this robustness transfers to three-dimensional models, since flow dynamics are severely altered between the two- and three-dimensional case (Rahmstorf, 1995). Yet, it turns out that, compared to computations without CA, applying the Newton-Raphson method to a model with one of the alternative CA schemes of section 3.4 still produces rather ill-posed systems, even if the artificial bifurcations due to traditional CA are absent or reduced in number. As a result, exploring the three-dimensional case is currently too challenging from a computational point of view. The technical details of this problem are beyond the scope of this work, but there are good prospects of resolving the issue. A hint of what might be expected if the flow dynamics were three-dimensional is provided by Weijer and Dijkstra (2001). They showed that the bifurcation diagram for the two-dimensional model is qualitatively similar to that of its three-dimensional extension, which was obtained by consecutively adding Earth rotation and surface wind stress. No CA was applied, however, so this result corresponds to the case with unstable stratification present in high latitudes. Nonetheless, using an iterative post-processing procedure, which avoids the problems of using CA in a numerical continuation experiment, Weijer and Dijkstra (2001) found that the mechanism of symmetry-breaking is probably not affected by the convective adjustment procedure. It may therefore well be that the alternatives presented in section 3.4 also mitigate the problems of applying CA in more complete models without affecting the relevant large-scale feedbacks.

Throughout this chapter, we have focussed on the use of numerical bifurcation techniques. It is to be emphasized, however, that artificial multiple steady states due to CA also occur in time-stepping models that are run until equilibrium is reached. Although the multiplicity was not classified as artificial behavior, Rahmstorf (1995) showed that in his idealized three-dimensional model many different convection patterns were stable under the same boundary conditions, using finite amplitude perturbations to switch between these states. Yet, it should be stated that the spurious saddle-node bifurcations due to CA are not evident in the hysteresis behavior of all ocean models (e.g. Sijp et al., 2006). Most likely, this is because a hysteresis experiment is inherently transient and can only result in approximate bifurcation diagrams. Even if the anomalous freshwater forcing is increased sufficiently slowly in time, the artificial steady states due to CA are not easily recognized, because the "jump" from one state to the other is relatively small (at least when overturning rate is used as measure of the solution, Fig. 3.2). It is however also possible that the artificial saddle-node bifurcations are not as ubiquitous as in the two-dimensional model results of section 3.2, because convection is more limited in space. Unlike the implicit model used here, most time-stepping codes currently employ isoneutral (Redi, 1982) and Gent and McWilliams (1990) mixing of tracers instead of simple horizontal diffusion. In a comparison of the two tracer mixing schemes Danabasoglu et al. (1994) showed that the use of the former causes convection to become much less widespread. Sijp et al. (2006) and Sijp and England (2009) suggested that this reduction is mainly due to isoneutral mixing and its interaction with the surface boundary conditions.

Eventually, computational resources will be no longer a limiting factor to run global simulations of the ocean at a resolution sufficient to capture the convective instability. This notwithstanding, coarser models probably remain valuable tools, provided that sub-grid scale

motions such as convection are parameterized in a way that is acceptable for the problem under study. Our results, in conjunction with previous work (Cessi, 1996; Cessi and Young, 1996; Vellinga, 1998; Hughes et al., 2009), demonstrate that convective adjustment has serious deficiencies. This strongly motivates to continue the development of parameterizations of convection that are both physically sound, and can be implemented in a numerical model without introducing artificial dynamics.

3.A   The analytical solution

Under the conditions specified in section 3.3.4, and defining $Q = P(1+F_0)^{-1}$, the temperature satisfies

$$0 = \frac{1}{Q}\frac{\partial^2 T}{\partial z^2} - T + \cos(2\pi z) \qquad \text{for} \quad z < z_c, \qquad (3.29a)$$

$$0 = \frac{1}{P}\frac{\partial^2 T}{\partial z^2} - T + \cos(2\pi z) \qquad \text{for} \quad z > z_c. \qquad (3.29b)$$

We require that the temperature and the diffusive temperature flux are continuous across $z = z_c$ and obtain

$$T = A_1 \cos(2\pi z) + B_1 \cosh\left(\sqrt{Q}(z+1)\right) \qquad \text{for} \quad z < z_c, \qquad (3.30a)$$

$$T = A_2 \cos(2\pi z) + B_2 \cosh\left(\sqrt{P}z\right) \qquad \text{for} \quad z > z_c. \qquad (3.30b)$$

Here,

$$A_1 = \left(1 + \frac{4\pi^2}{Q}\right)^{-1}, \qquad (3.31a)$$

$$A_2 = \left(1 + \frac{4\pi^2}{P}\right)^{-1}, \qquad (3.31b)$$

$$B_1 \cosh\left(\sqrt{Q}(z_c+1)\right) = $$
$$\frac{2\pi\left(\frac{P}{Q}A_1 - A_2\right)\sin(2\pi z_c) + (A_1 - A_2)\cos(2\pi z_c)\sqrt{P}\tanh\left(\sqrt{P}z_c\right)}{\frac{P}{Q}\sqrt{Q}\tanh\left(\sqrt{Q}(z_c+1)\right) - \sqrt{P}\tanh\left(\sqrt{P}z_c\right)}, \qquad (3.31c)$$

$$B_2 \cosh\left(\sqrt{P}z_c\right) = $$
$$\frac{2\pi\left(\frac{P}{Q}A_1 - A_2\right)\sin(2\pi z_c) + (A_1 - A_2)\cos(2\pi z_c)\frac{P}{Q}\sqrt{Q}\tanh\left(\sqrt{Q}(z_c+1)\right)}{\frac{P}{Q}\sqrt{Q}\tanh\left(\sqrt{Q}(z_c+1)\right) - \sqrt{P}\tanh\left(\sqrt{P}z_c\right)}. \qquad (3.31d)$$

The salinity profile is determined from

$$0 = \frac{1}{Q}\frac{\partial^2 S}{\partial z^2} + \gamma\cos(\pi z) \qquad \text{for} \quad z < z_c, \qquad (3.32a)$$

$$0 = \frac{1}{P}\frac{\partial^2 S}{\partial z^2} + \gamma\cos(\pi z) \qquad \text{for} \quad z > z_c. \qquad (3.32b)$$

We impose continuity of S at $z = z_c$ and the integral constraint

$$\int_{-1}^{0} S\mathrm{d}z = 0$$

to find

$$\gamma^{-1} S = C_1 \cos(\pi z) + D_1 \qquad \text{for} \quad z < z_c, \qquad (3.33a)$$

$$\gamma^{-1} S = C_2 \cos(\pi z) + D_2 \qquad \text{for} \quad z > z_c, \qquad (3.33b)$$

where

$$C_1 = \frac{Q}{\pi^2}, \qquad (3.34a)$$

$$C_2 = \frac{P}{\pi^2}, \qquad (3.34b)$$

$$D_1 = \frac{P-Q}{\pi^3} \left(\sin(\pi z_c) - \pi z_c \cos(\pi z_c) \right), \qquad (3.34c)$$

$$D_2 = \frac{P-Q}{\pi^3} \left(\sin(\pi z_c) - \pi \left(z_c + 1 \right) \cos(\pi z_c) \right). \qquad (3.34d)$$

4

Effect of atmospheric feedbacks on the stability of the Atlantic meridional overturning circulation

The impact of atmospheric feedbacks on the multiple equilibria (ME) regime of the Atlantic meridional overturning circulation (MOC) is investigated using a fully-implicit hybrid coupled model (HCM). The HCM consists of a global ocean model coupled to an empirical atmosphere model that is based on linear regressions of the heat, net evaporative, and momentum fluxes generated by a fully-coupled climate model onto local as well as Northern Hemisphere averaged sea surface temperatures. Using numerical continuation techniques bifurcation diagrams are constructed for the HCM with the strength of an anomalous freshwater flux as bifurcation parameter, which allows for an efficient first-order estimation of the effect of interactive surface fluxes on the MOC stability. The different components of the atmospheric fluxes are first considered individually and then combined. Heat feedbacks act to destabilize the present-day state of the MOC and to stabilize the collapsed state, thus leaving the size of the ME regime almost unaffected. In contrast, interactive freshwater fluxes cause a destabilization of both the present-day and collapsed states of the MOC. Wind feedbacks are found to have a minor impact. The joint effect of the three interactive fluxes is to narrow the range of ME. The shift of the saddle-node bifurcation that terminates the present-day state of the ocean is further investigated by adjoint sensitivity analysis of the overturning rate to surface fluxes. It is found that heat feedbacks primarily affect the MOC stability when they change the heat fluxes over the North Atlantic subpolar gyre, whereas interactive freshwater fluxes have an effect everywhere in the Atlantic basin.

4.1 Introduction

The circulation of the North Atlantic Ocean is thought to be a particularly sensitive component of the climate system. According to a long-standing hypothesis, the Atlantic meridional overturning circulation (MOC), which controls the meridional heat transport, is vulnerable to freshwater anomalies due to the salt advection feedback (section 1.2; Stommel, 1961; Bryan, 1986). As a result of this feedback, there may be a another stable equilibrium of the MOC, additional to the present-day temperature driven overturning, in which a self-sustained salinity distribution drives a reversed (and usually much weaker) circulation.

Multiple equilibria are indeed present in a hierarchy of ocean-only models, such as box models (Thual and Mcwilliams, 1992), two- (Cessi and Young, 1992) and three-dimensional models (Weijer and Dijkstra, 2001), and Earth System Models of Intermediate Complexity (EMICs; Rahmstorf et al., 2005). In these models, a relatively rapid (on a decadal to century time scale) transition from one equilibrium state to the other can be induced by changing the freshwater boundary conditions or by perturbing the salinity field.

In state-of-the-art Global Climate Models (GCMs), such as used in the fourth assessment report of the IPCC (Meehl et al., 2007) such multiple stable states have not yet been found. Computational constraints currently prevent performing the extensive parameter sweep experiments that are required to detect a bistable regime of the MOC in these models. The fact that no permanent collapse of the MOC is observed in the Special Report on Emissions Scenarios (SRES) A1B scenario runs, as discussed by Schmittner et al. (2005), or in experiments in which the high latitude freshwater flux is temporarily perturbed, as analyzed by Stouffer et al. (2006), is hence not conclusive about the existence of multiple stable equilibria in state-of-the-art GCMs.

Different conclusions have been reached based on coupled ocean-atmosphere models that use a coarser resolution than the state-of-the-art models. The results of Yin et al. (2006) suggest that the presence of a dynamically active atmosphere causes the bistable regime of the MOC to disappear. In that case the presence of multiple equilibria should be considered as an artifact of ocean-only models and EMICs that arises due to the poor representation of the interaction between atmosphere and ocean. In contrast, a recent extensive investigation by Hawkins et al. (2011) demonstrated the presence of multiple equilibria in FAMOUS, which is a low resolution version of a fully coupled GCM. Although differences in spatial resolution, and in the representation of unresolved processes are also likely to affect the MOC stability in different models, this study will focus on the effect of atmospheric feedbacks.

A reduction of the MOC due to freshwater anomalies leads to changes in sea surface temperatures, which, in turn, induce a change in wind fields, near surface air temperatures and evaporation and precipitation patterns. These atmospheric processes constitute changes in the ocean forcing and may hence feed back on the response of the MOC to freshwater anomalies. The southward shift of the Intertropical Convergence Zone (ITCZ) in response to a reduction of the MOC is a well-documented example of how the atmosphere interacts with the ocean, both as a mechanism for decadal variability (Vellinga and Wu, 2004), and as a process that destabilizes the collapsed state of the MOC (Vellinga et al., 2002; Yin et al., 2006).

The main question addressed in the chapter is: how do atmospheric processes affect the bistable regime of the Atlantic MOC? We approach this problem by starting from the ocean-

only case for which the stability properties have been systematically analyzed over the last decade. It is known that multiple equilibria in an ocean-climate model are connected to the existence of two saddle-node bifurcations (Dijkstra, 2005). The distance between the two saddle-node bifurcations in terms of the magnitude of a freshwater perturbation determines the width of the hysteresis which is found in quasi-equilibrium simulations (Rahmstorf et al., 2005). Using techniques from numerical bifurcation theory, the saddle-node bifurcations have been determined for a global ocean-only model (Dijkstra and Weijer, 2005) and an indicator was suggested to monitor the presence of the multiple equilibria regime (Huisman et al., 2010). In this study, we will use a fully-implicit Hybrid Coupled Model (HCM) and techniques of numerical bifurcation theory to determine the changes, and the physical processes causing these changes, in the position of the saddle-node bifurcations when atmospheric feedbacks are represented. The HCM consists of a global ocean general circulation model coupled to an empirical atmosphere model. The latter is based on linear regressions of the momentum, heat, and freshwater fluxes generated by a fully-coupled climate model onto local as well as Northern Hemisphere averaged sea surface temperatures (Cimatoribus et al., 2012).

The outline of this chapter is as follows. The model and methodology used are described in section 4.2. Section 4.3 presents the results on the changes in the bifurcation diagrams, of which the physics is further analyzed in section 4.4. A summary and discussion follows in section 4.5.

4.2 Model

The behavior of the coupled ocean-atmosphere system is investigated using numerical steady-state continuation and adjoint sensitivity analysis. These methods require that our model admits true steady-state solutions. So, it must exhibit less rich dynamics than state-of-the-art GCM's, but it should include the relevant long-term mean ocean-atmosphere interaction. This is achieved by adopting a hybrid approach in which we combine a fully-implicit, coarse-resolution ocean model with an empirical description of the fluxes at the ocean-atmosphere interface.

The core of the hybrid model is the Arakawa C-grid version of the ThermoHaline Circulation Model (THCM-C, Weijer et al., 2003), which is a fully-implicit ocean model designed specifically to perform numerical bifurcation analysis (section 1.3). The THCM-C is based on the rigid-lid primitive equations in spherical coordinates, formulated in longitude/latitude/depth coordinates. The model domain covers a near global region extending from 85.5°S to 85.5°N, and incorporates realistic bottom topography. The zonal (meridional) grid spacing is 3.75° (4.5°) and there are 12 levels, ranging in thickness from 50 m for the top layer to 950 m for the bottom layer. As reviewed in section 1.3, THCM-C can be used effectively only when the eddy viscosity is relatively high (Wubs et al., 2006) and when no convective adjustment scheme is applied (Vellinga, 1998; chapter 3). Despite these limitations many of the characteristics of the large-scale circulation, and, specifically, its equilibrium sensitivity to an anomalous freshwater forcing are consistent between THCM-C and traditional ocean models with the same resolution (Weijer et al., 2003; Dijkstra and Weijer, 2005).

The new element presented in this work is the treatment of the surface forcing. In addition

to boundary conditions corresponding to fixed atmospheric conditions, we use the empirical model developed by Cimatoribus et al. (2012) to calculate momentum, heat, and freshwater fluxes as function of changes in sea surface temperature (SST). We perform a number of computations in which we track the state of the global ocean as function of the strength of a persistent anomalous freshwater flux. Each of these computations results in a bifurcation diagram that provides exact information about the parameter regime for which the present-day and "collapsed" states of the MOC exist. The effect of different atmospheric feedbacks is evaluated by comparing the bifurcation diagram of a model in which the boundary conditions are (partially) interactive to the diagram of the model in which atmospheric feedbacks are absent.

We start with a description of the boundary conditions for the ocean-only (indicated by superscript oo) version of the model. The momentum fluxes, denoted by F_u^{oo} and F_v^{oo} for the zonal and meridional direction, respectively, are given by the annual mean wind stress climatology of Trenberth et al. (1989). The buoyancy fluxes are defined with respect to a reference (superscript R) solution for which the anomalous freshwater flux is zero. (Note that, although the boundary condition is in fact implemented as a flux of salt, we adhere to the "freshwater" terminology throughout the chapter.) The reference freshwater flux F_E^R (positive for evaporation, Fig. 4.1a) is equal to the flux implied by a restoring boundary condition on the reference sea surface salinity using the Levitus data set (Levitus et al., 1994) as target field. The total freshwater flux for grid point (i, j) is now given by

$$F_E^{oo}(i, j) = F_E^R(i, j) - \gamma F_E^p(i, j) - \Delta F_E. \tag{4.1}$$

Here, γ is the control or bifurcation parameter in all computations. It represents the amplitude of a freshwater perturbation that is applied over a region south of Greenland, indicated by F_E^p, and defined as the area confined by longitudes 60°W and 24°W and latitudes 54°N and 66°N. The term ΔF_E is a spatially constant compensation that is defined such that the flux integrates to zero. In the formulation of Weijer et al. (2003) the boundary condition for sea surface temperature follows from a one-layer energy balance model, in which the atmospheric temperature T_a is computed. In order to avoid interference with the empirical description of the atmosphere adopted in this study, the energy balance model is disabled. This is done by fixing the atmospheric temperature to the reference field T_a^R (Fig. 4.1b), while retaining the coupling to the ocean. The heat flux into the ocean is then given by

$$F_Q^{oo}(i, j) = \frac{I_0}{4} S(\phi(j)) (1 - \alpha) C_0 - \mu \left(\text{SST}(i, j) - T_a^R(i, j) \right). \tag{4.2}$$

Here, $I_0 = 1360 \, \text{W m}^{-2}$ is the solar constant,

$$S(\phi) = 1 - 0.241 \left(3 \sin^2 \phi - 1 \right)$$

the latitudinal (ϕ) dependence of the shortwave radiative heat flux, $\alpha = 0.3$ the albedo, $C_0 = 0.43$ the transmission coefficient, and $\mu = 13.0 \, \text{W m}^{-2} \, °\text{C}^{-1}$ a coupling coefficient. The formulation of the heat flux in Eq. (4.2) is mathematically equivalent to a restoring condition, but the relaxation time scale (about 200 d) is much longer than the often-used 30 d damping time scale. Furthermore, note that the target field would not be T_a^R, but rather $T_a^R + \frac{I_0}{4\mu} S(\phi) (1 - \alpha) C_0$. So, since $S(\phi)$ is positive everywhere, sea surface temperatures

must exceed T_a^R in order to realize a balance between incoming solar radiation and heat loss to the atmosphere, as illustrated in Fig. 4.1c for the reference sea surface temperature.

The effect of atmospheric feedbacks is represented by two additional contributions to the boundary conditions that depend linearly on SST (Cimatoribus et al., 2012). Both are assumed to vanish at the reference solution, for which $\text{SST} = \text{SST}^R$. The first contribution is proportional to local SST anomalies, while the second depends on SST averaged over the Northern Hemisphere and is assumed to account for the large-scale changes that arise when the strength of the Atlantic MOC decreases. For heat ($C = Q$), net evaporation ($C = E$), and momentum ($C = u$ or $C = v$), the hybrid model fluxes can be written as

$$
\begin{aligned}
F_C(i,j) = F_C^{oo}(i,j) &+ \xi_C p_1^{F_C}(i,j) \cdot \left(\text{SST}(i,j) - \text{SST}^R(i,j) \right) \\
&+ \xi_C p_2^{F_C}(i,j) \cdot \left(\langle \text{SST} \rangle_{NH} - \langle \text{SST}^R \rangle_{NH} \right),
\end{aligned}
\tag{4.3}
$$

where the $\langle \rangle_{NH}$ indicate the average over the Northern Hemisphere. The homotopy parameters ξ_C serve to control which of the individual feedbacks are active. The fields $p_1^{F_C}$ and $p_2^{F_C}$ in Eq. (4.3) are derived from a linear regression analysis on the output of two simulations with the fully-coupled SPEEDO (Speedy-Ocean) model (Severijns and Hazeleger, 2009) as detailed by Cimatoribus et al. (2012). The local regression parameters $p_1^{F_C}$ are calculated from a yearly averaged time series of the unperturbed SPEEDO simulation, while the large-scale parameters $p_2^{F_C}$ derive from a simulation with the same model in which the Atlantic MOC is forced to collapse.

Cimatoribus et al. (2012) have evaluated the performance of the empirical atmosphere model by coupling it to SPEEDO's ocean component, CLIO (Coupled Large-scale Ice Ocean model; Goosse and Fichefet, 1999). It was shown that the relevant long-term mean behavior of the MOC is essentially the same in the hybrid CLIO model and in the fully-coupled SPEEDO model, thus validating the approach of regressing atmospheric fluxes onto SST.

It should be kept in mind, however, that the regression coefficients were derived with reference to the unperturbed present-day state. Predictions of the changes in MOC stability are therefore probably more reliable for the present-day MOC than for the collapsed MOC.

In addition, there are several differences between the hybrid CLIO model of Cimatoribus et al. (2012) and the implicit hybrid model described here that should be considered in the interpretation of the results. First, as discussed above, the implicit methodology places constraints on the complexity of the parameterizations of subgrid-scale mixing in THCM-C, while CLIO includes sophisticated schemes to represent the unresolved physics. As a consequence, both models need to use their own set of ocean-only boundary conditions. Otherwise a very unrealistic circulation would result due to the strong sensitivity of the overturning to the patterns of heat and freshwater fluxes. The hybrid CLIO model uses the climatological mean fluxes of SPEEDO, while the implicit hybrid model uses the fluxes F_C^{oo} defined above. Hence, the fundamental assumption behind Eq. (4.3) is that its expression of the atmospheric response to changes in the MOC strength is sufficiently generic to give reliable results in different ocean models. A second difference is that the climatological mean fluxes and the local regression parameters vary seasonally in the hybrid CLIO, while the forcing in the implicit hybrid model is necessarily constant in time. As a result it does not capture the possible effects due to rectification of interactive atmospheric fluxes. Several tests with the hybrid CLIO in which constant local regression parameters were used, however, indicate that this rectifica-
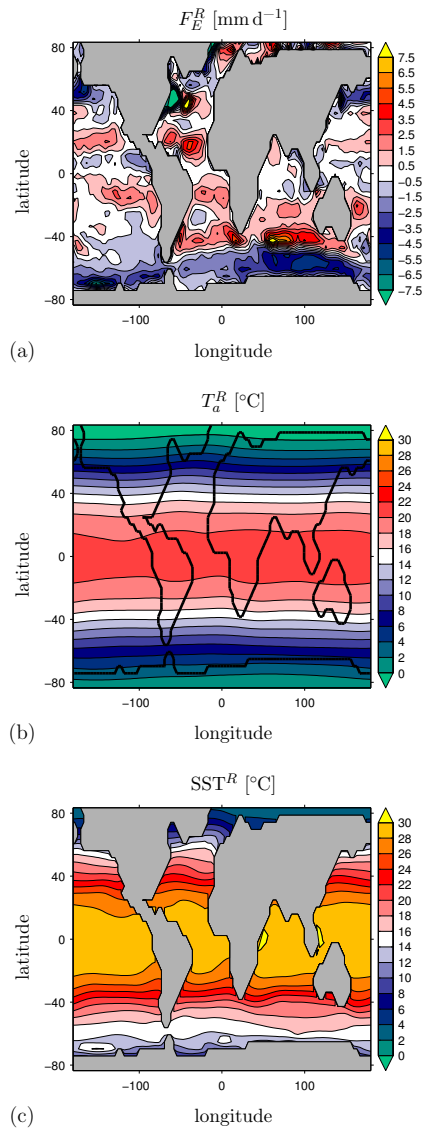
(a)

(b)

(c)

Figure 4.1: Reference fields of (a) evaporation minus precipitation, (b) atmospheric temperature, and (c) sea surface temperature.

tion effect is small. Finally, the implicit hybrid model does not include a sea ice component, whereas the hybrid CLIO does. The regression parameters $p_1^{F_C}$ and $p_2^{F_C}$ used here therefore include the effect of changing sea ice cover, so that they express the "effective" feedback of the combined atmosphere-sea ice system. This issue is further discussed in section IVB of the paper by Cimatoribus et al. (2012).

4.3 Bifurcation diagrams

4.3.1 Computation of steady-states

Due to the addition of the empirical atmosphere model it is convenient to slightly extend the methodology outlined in section 1.3. Readers less interested in this technical material may want to take note of Eq. (4.4) and its explanation before skipping to the results in section 4.3.2.

Instead of Eq. (1.10) the hybrid coupled model is represented as

$$\mathbf{M}\frac{d\mathbf{x}}{dt} = \tilde{\mathscr{F}}\left(\mathbf{x},\gamma,\xi_C\right) = \mathscr{F}\left(\mathbf{x},\gamma\right) + \sum_{C=Q,S,u,v} \xi_C \mathbf{L}_C\left(\mathbf{x}-\bar{\mathbf{x}}^R\right), \qquad (4.4)$$

where $\mathbf{x}$ is the N-dimensional state vector, $\mathbf{M}$ a diagonal matrix, and $\tilde{\mathscr{F}}$ a nonlinear operator, which we split into two parts. The operator $\mathscr{F}$ on $\mathbf{x}$ is the expression of all the processes included in the ocean component of model: the pressure gradient and Coriolis forces, advection, diffusion, et cetera. It depends on many parameters, but here we only highlight its dependence on the control parameter γ. The second part of $\tilde{\mathscr{F}}$ is the expression of the empirical atmosphere model, and corresponds to the terms added to F_C^{ao} in Eq. (4.3). The vector $\bar{\mathbf{x}}^R$ is the reference steady-state at $\gamma = 0$. The matrices $\mathbf{L}_C$ define the action of the coefficients $p_1^{F_C}(i,j)$ and $p_2^{F_C}(i,j)$ on the part of $\mathbf{x}$ that corresponds to the SSTs.

Steady-state solutions of Eq. (4.4) are found using Newton's method [Eq. (1.15)], which involves solving linear systems with the Jacobian matrix

$$\tilde{\Phi} = \Phi + \sum_{C=Q,S,u,v} \xi_C \mathbf{L}_C. \qquad (4.5)$$

The matrix Φ is the Jacobian matrix of the ocean-only operator $\mathscr{F}$. Because the stencil used for space discretization is compact, this matrix is sparse. As a result systems with Φ can be solved relatively efficiently using preconditioning and iterative solvers (Weijer et al., 2003). The matrices $\mathbf{L}_C$, however, are dense, due to the averaging operations implied by the definitions of $\langle \text{SST}\rangle_{NH}$ and ΔF_E. This means that $\tilde{\Phi}$ cannot be handled efficiently with iterative solution techniques.

We therefore separate out the averaging operations and rewrite the hybrid model as

$$\mathbf{M}\frac{d\mathbf{x}}{dt} = \tilde{\mathscr{F}}\left(\mathbf{x},\gamma,\xi_C\right) = \mathscr{F}'\left(\mathbf{x},\gamma,\xi_C\right) + p\mathbf{P}\left(\xi_C\right) + q\mathbf{Q}, \qquad (4.6)$$

where the additional variables p and q are the Northern Hemisphere averaged temperature, that is:

$$\langle \text{SST}\rangle_{NH} - p = 0; \qquad (4.7)$$

and the freshwater correction, that is:

$$\Delta F_E - q = 0. \tag{4.8}$$

The vector $\mathbf{P}$ contains the large-scale regression coefficients $p_2^{Fc}(i,j)$, while $\mathbf{Q}$ corresponds to a spatially uniform correction to the sea surface salinity field. The remaining sparse parts of the matrices $\xi_C \mathbf{L}_C$, which correspond to the local coupling through the regression coefficients $p_1^{Fc}(i,j)$, are added to $\mathscr{F}$, and the result is indicated by $\mathscr{F}'$. As will be explained below, the advantage of introducing the additional variables p and q is that the calculation of Newton updates now only requires solving systems with the Jacobian matrix of $\mathscr{F}'$ (denoted by Φ') which is a sparse matrix.

A pseudo-arclength parameterization (Keller, 1977) is used to find of a branch of solutions $(\bar{\mathbf{x}}(s), \bar{p}(s), \bar{q}(s), \gamma(s))$, where s is the arclength parameter. The set of equations is closed by adding an equation of the form

$$r(\mathbf{x}, p, q, \gamma) = \dot{\mathbf{x}}_0^T(\mathbf{x} - \mathbf{x}_0) + \dot{p}_0(p - p_0) + \dot{q}_0(q - p_0) + \dot{\gamma}_0(\gamma - \gamma_0) - \Delta s = 0. \tag{4.9}$$

The subcripts 0 are used to denote a previous solution on the branch, dots indicate the derivative with respect to s, and Δs is the step size of the arclength parameter.

In addition to the N-dimensional state vector $\mathbf{x}$, three additional variables, p, q, and s, were introduced, so that the total number of equations that must be solved is $N + 3$. Omitting the Newton iteration counter k in the Jacobian, the Newton updates for this extended system [Eqs (4.6-4.9)] are found from

$$\begin{pmatrix} \Phi' & \mathbf{P} & \mathbf{Q} & \frac{\partial \mathscr{F}'}{\partial \gamma} \\ \left(\frac{\partial \langle \text{SST} \rangle_{NH}}{\partial \mathbf{x}}\right)^T & -1 & 0 & 0 \\ \left(\frac{\partial \Delta F_E}{\partial \mathbf{x}}\right)^T & \frac{\partial \Delta F_E}{\partial p} & -1 & \frac{\partial \Delta F_E}{\partial \gamma} \\ \dot{\mathbf{x}}_0^T & \dot{p}_0 & \dot{q}_0 & \dot{\gamma}_0 \end{pmatrix} \begin{pmatrix} \mathbf{x}^{k+1} - \mathbf{x}^k \\ p^{k+1} - p^k \\ q^{k+1} - q^k \\ \gamma^{k+1} - \gamma^k \end{pmatrix} = \begin{pmatrix} -\tilde{\mathscr{F}}^k \\ p^k - \langle \text{SST} \rangle_{NH} \\ q^k - \Delta F_E \\ -r^k \end{pmatrix}$$

The extended Jacobian thus consists of the sparse Jacobian matrix Φ', bordered by three dense rows and columns. We exploit the sparsity of Φ' by first solving the four systems $\Phi' \mathbf{z}_1 = -\tilde{\mathscr{F}}$, $\Phi' \mathbf{z}_2 = \mathbf{P}$, $\Phi' \mathbf{z}_3 = \mathbf{Q}$, and $\Phi' \mathbf{z}_4 = \frac{\partial \mathscr{F}'}{\partial \gamma}$ for $\mathbf{z}_i$, $i = 1, \ldots, 4$, and then constructing the Newton update from the $\mathbf{z}_i$.

4.3.2 Results

The bifurcation structure of the ocean-only model (Fig. 4.2), which is computed by setting all $\xi_C = 0$, includes two saddle-node bifurcations, labelled L_1 and L_2. These bifurcations define three branches of solutions, whose characteristics are discussed in detail by Dijkstra and Weijer (2005). The left panel of Fig. 4.2 shows the bifurcation diagram with the Atlantic meridional overturning strength, Ψ_A, as measure of the solution. We define Ψ_A as the maximum of the meridional overturning stream function, measured below a depth of $500\,\text{m}$ in order to exclude the contribution from shallow wind-driven cells. The solutions on the branch labelled ON are linearly stable and correspond to present-day climate states, characterized by a strong overturning in the Atlantic with a typical pattern as shown in Fig. 4.3a. The ON state
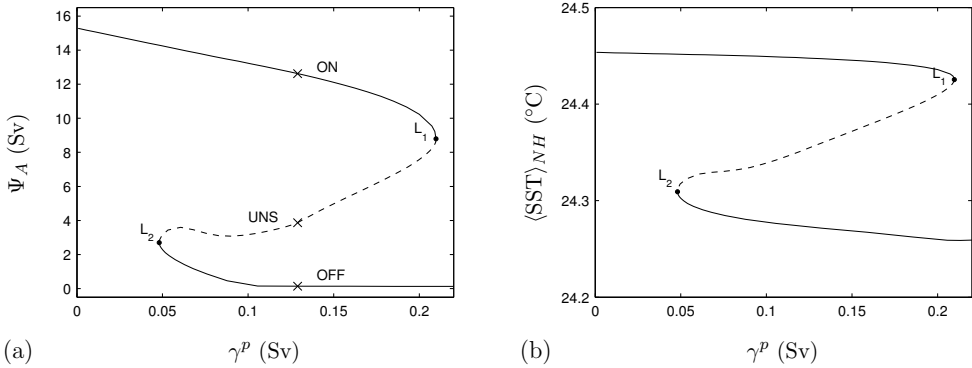
Figure 4.2: Bifurcation diagram for the ocean-only model showing (a) the maximum of the Atlantic meridional overturning stream function, measured below 500 m, and (b) the Northern Hemisphere averaged SST. Solid lines indicate that the branch is linearly stable, while dashed lines mean it is linearly unstable.

can only be maintained for $\gamma < \gamma(L_1) = 209.8$ mSv. For $\gamma > \gamma(L_2) = 48.0$ mSv it coexists with an unstable (UNS, Fig. 4.3b) and a linearly stable collapsed state of the Atlantic MOC (OFF, Fig. 4.3c).In the right panel of Fig. 4.2 we plot the diagram using the Northern Hemisphere averaged SST ($\langle SST \rangle_{NH}$) as measure of the solution. The reduction in the Atlantic MOC strength leads to a reduction in $\langle SST \rangle_{NH}$, as is required for our representation of the large-scale atmospheric feedbacks [see discussion surrounding Eq. (4.3)] to be valid. The difference in temperature between ON and OFF is approximately $0.2\,°C$, which is comparable to the response in the ocean-only version of the hybrid CLIO model of Cimatoribus et al. (2012).

The next step is to allow the operation of air-sea interactions by setting all $\xi_C = 1$. Fig. 4.4a shows that, although the size of the multiple equilibria regime is reduced compared to the ocean-only case, the bistability of the Atlantic overturning circulation is maintained in the hybrid coupled model. Both the ON and OFF states are destabilized by atmospheric feedbacks, in the sense that bifurcation point L_1 occurs at a smaller, and L_2 at a larger value of γ than in the ocean-only model. Quantitatively, however, the shift of L_1 is bigger than the shift of L_2 (Table 4.1).

The relative importance of the heat ($C = Q$), freshwater ($C = E$), and momentum ($C = u$ and $C = v$) flux feedbacks in the hybrid coupled model can be assessed by putting only the respective homotopy parameter $\xi_C = 1$, and leaving the others at zero. If only heat is interactive ($\xi_Q = 1$) the bifurcation diagram shifts towards smaller values of the freshwater anomaly γ (Fig. 4.4b). The destabilization of the ON state, as measured by the change in the value of γ corresponding to L_1, is about as large as the stabilization of the OFF state (Table 4.1). In contrast, switching on only the freshwater feedback ($\xi_E = 1$) results in a significant decrease in the size of the multiple equilibria regime, because both the ON and OFF state are destabilized (Fig. 4.4c). When only the momentum feedback is switched on ($\xi_u = \xi_v = 1$), both the ON and OFF state can be maintained across a range of γ that is only slightly larger than for the ocean-only model (Fig. 4.4d).
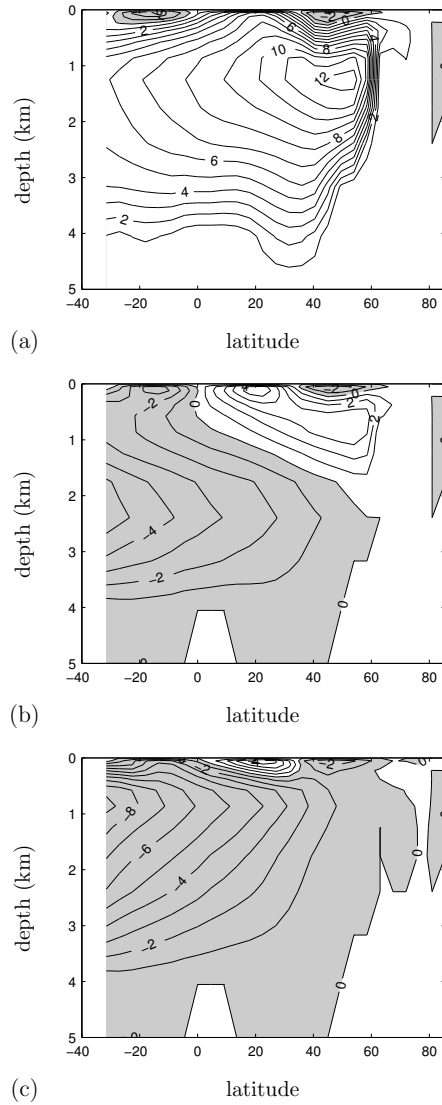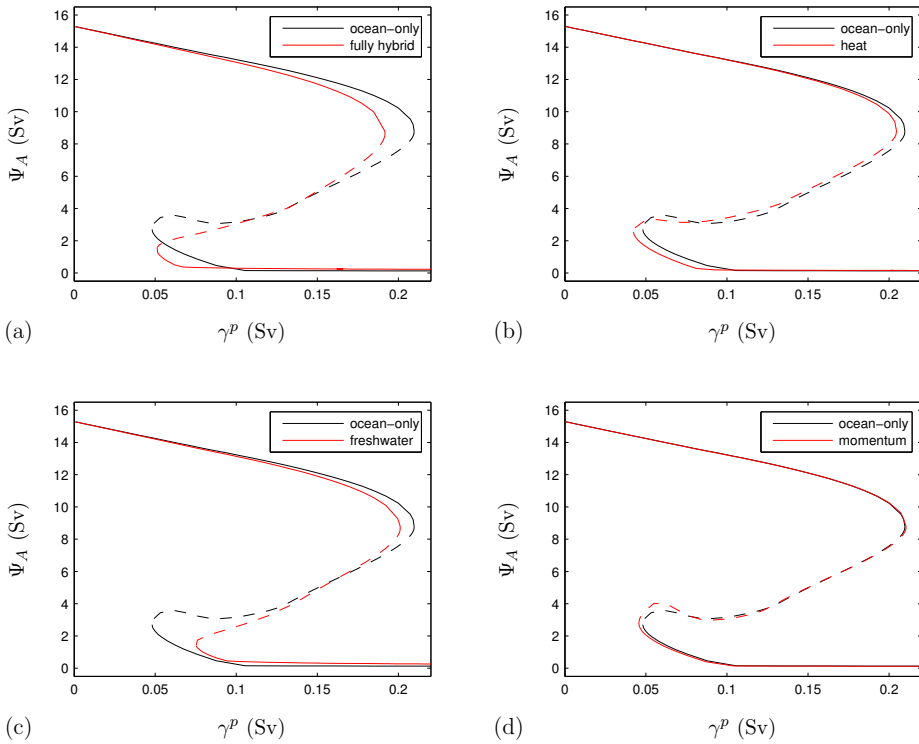
Figure 4.3: Contour plots of the Atlantic meridional overturning stream function for the (a) ON, (b) UNS, and (c) OFF state at $\gamma = 0.13\,\mathrm{Sv}$ (see crosses in panel a of Fig. 4.2). The contour interval is $1\,\mathrm{Sv}$ and shading indicates negative values.

Figure 4.4: Changes in the bifurcation diagram due to the surfaces fluxes being interactive. The black line represents the ocean-only case as in Fig. 4.2a and the red lines correspond to (a) the full hybrid coupled model, and the cases with only (b) interactive heat fluxes, (c) interactive freshwater fluxes, and (d) interactive momentum fluxes enabled.

The shifts of the bifurcation points L_1 and L_2 in the full hybrid model (Fig. 4.4a) appear to be consistent with a simple combination of the shifts in each of the partially interactive models (Fig. 4.4b-d). This is only true in qualitative sense, however. As listed in Table 4.1, the value of γ at L_1 is 18.0 mSv smaller in the full hybrid model than in the ocean-only model, while the shifts of the individual feedbacks added together amount to a shift of only 13.2 mSv. The actual shift of L_2 in the full hybrid model, on the other hand, is much smaller than simple addition would predict: 3.1 mSv rather than 18.9 mSv. Although a complete analysis of this issue is beyond the scope of this work, two aspects of it are worth discussing in more detail.

First, we emphasize the role of interactive heat fluxes in determining the SST field. For solutions that are relatively close to the reference state atmospheric feedbacks do not significantly alter the pattern of the circulation compared to the ocean-only case. This explains why the value of Ψ_A at saddle-node bifurcation L_1 is approximately the same in all of the cases shown in Fig. 4.4. Despite the similarity of the circulation, the SST field differs depending on whether the heat feedback is enabled or not. As can be deduced from Eq. (4.3) the sea surface temperature contrast $\text{SST}(i, j) - \text{SST}^R(i, j)$ at a particular location (i, j) is either am-

Table 4.1: Changes in the value of γ corresponding to the saddle-node bifurcation points L_1 and L_2 as a result of atmospheric feedbacks. Positive values mean that the saddle-node bifurcation shifts to larger values of γ.

	Shift of L_1 (mSv)	Shift of L_2 (mSv)
Heat	-5.2	-5.8
Freshwater	-8.7	27.2
Momentum	0.7	-2.5
All	-18.0	3.1

plified [if $F_Q(i,j) - F_Q^{oo}(i,j)$ is of the same sign as $SST(i,j) - SST^R(i,j)$], or damped [if the two quantities are of opposite sign] by the interactive heat flux. Figure 4.5 shows that the Northern Hemisphere averaged SST is less sensitive to changes in Ψ_A when the heat feedback is enabled ($\xi_Q = 1$). As a consequence, the *large-scale* interactive freshwater and momentum fluxes, which are proportional to $\langle SST \rangle_{NH} - \langle SST^R \rangle_{NH}$, will be smaller when the heat feedback is switched on. Whether the *local* interactive freshwater and momentum fluxes are enhanced or reduced by the direct feedback of heat on SST depends on the location that is considered, as will be shown for a solution close to bifurcation point L_1 in section 4.4. The fact that the shift of L_1 is larger in the full hybrid model than the sum of the shifts in each of the partially interactive models suggests that the heat feedback modifies the SST field in such a way that those fluxes are favored that destabilize the ON state of the MOC.

Second, we point out that as atmospheric fluxes increase in magnitude, they not only affect the strength of the MOC, but the pattern of the circulation as well. So, in addition to the direct impact of the heat feedback, interactive fluxes also influence the SST field indirectly by modifying the surface velocity field. This effect explains the (slight) differences in the plots of Ψ_A versus $\langle SST \rangle_{NH}$ (Fig. 4.5) between the three models without interactive heat fluxes ('ocean-only', 'freshwater', and 'momentum'), as well as the difference between the two models with interactive heat fluxes ('fully hybrid' and 'heat'). The effect described here implies that there is a complex coupling between SST and all interactive atmospheric fluxes. Figure 4.5 suggests, however, that in our model results indirect effects are of secondary importance compared to the direct influence of the heat feedback on SST.

As reported above the window of bistability hardly changes when the feedbacks in the momentum fluxes are switched on (Fig. 4.4d). This can be attributed to the relatively high eddy viscosity that is used in THCM-C (Dijkstra and Weijer, 2005). Using an EMIC Arzel et al. (2011) showed that wind-stress feedbacks do not alter the stability of the ON state. Consistently, coupled GCM results of Dixon et al. (1999) suggest that the ON state overturning strength is hardly affected by momentum fluxes being interactive or not. We are therefore confident in the result that saddle-node bifurcation L_1 does not shift much due to wind feedbacks. The OFF state, however, is expected to have a substantially different surface circulation as a result of altered winds (Vellinga and Wood, 2002). In the hybrid CLIO model of Cimatoribus et al. (2012) the difference in $\langle SST \rangle_{NH}$ between the ON and OFF state is about 1.2 °C. By switching off the wind feedback in the hybrid CLIO model it is found that interactive winds are responsible for about 1 °C of this difference. The destabilization of

Figure 4.5: Northern Hemisphere averaged sea surface temperature versus Atlantic MOC strength for the computations with the ocean-only model, and the hybrid model with (partially) interactive fluxes as indicated. As in the bifurcation diagrams, the linestyle indicates the linear stability of the states [solid (dashed) means (un)stable].
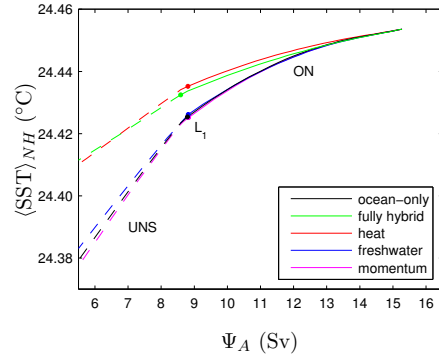
the OFF state due interactive freshwater fluxes (Fig. 4.4c) appears to be reduced in the full hybrid model (Fig. 4.4a) as a result of the direct impact of interactive heat fluxes on SST. This reduction may well be counteracted, however, by the indirect effect of interactive momentum fluxes that is described here. As this effect is not accurately reproduced by THCM-C, it is not possible to reliably compare the relative amounts by which the ON and OFF states are destabilized. This deficiency will be discussed further in section 4.5

4.4 Adjoint sensitivity Analysis

It was shown in the previous section that the addition of atmospheric feedbacks results in changes in the bifurcation diagram of the persistent freshwater perturbation γ. In particular, we described the shifts of the two saddle-node bifurcations, which define the multiple equilibria regime, but noted that the results for saddle-node L_2 should be treated with care if feedbacks acting through the momentum fluxes are enabled. In addition, we recall that the regression coefficients p_1^{Fc} and p_2^{Fc} [Eq. (4.3)] were derived with reference to the ON state with $\gamma = 0$. The focus of this section is therefore on the shift of saddle-node bifurcation L_1. Using adjoint sensitivity analysis we aim to link the changes in the stability of the ON state to the physical processes responsible for it.

4.4.1 Overturning rate as measure of stability

Figure 4.4 shows that the overturning strength Ψ_A is roughly the same (about 8.8 Sv) at bifurcation point L_1 irrespective of which fluxes are interactive. So, those atmospheric fluxes that cause a reduction of the overturning strength push saddle-node bifurcation L_1 to smaller values of γ, and vice versa. We therefore argue that it is sufficient to explain how Ψ_A is modified by atmospheric feedbacks in order to understand the changes in the stability of the present-day branch. In fact, as will be shown below, it is possible to compute a first order estimate of the shift of L_1 by calculating the change in the freshwater perturbation γ that would oppose the change in Ψ_A caused by enabling the atmospheric feedbacks.

4.4.2 Computation of adjoint sensitivities

Numerical steady-state continuation provides the sensitivity of a solution to a single control parameter and bifurcation diagrams can be drawn for any metric of the solution. In contrast, adjoint sensitivity analysis provides the sensitivity of a single metric of the solution to any model parameter. We argued above that a useful metric is defined by the Atlantic MOC strength, which must be computed at a fixed depth and latitude (denoted by $\Psi_A^{\phi,z}$). To explain the shift of saddle-node bifurcation L_1 we consider simultaneous infinitesimal variation of the strength of one of the feedbacks and of the amplitude of the freshwater perturbation γ in such a way that the steady-state overturning remains constant. We start from the ocean-only solution (all ξ_C set to zero) at $\gamma = 0.2\,\text{Sv}$, which is close to bifurcation point L_1. For this solution the maximum of the Atlantic overturning stream function occurs at $\phi = 54°N$ and $z = 1247$ meter.

In view of the insignificance of the wind feedback for the ON state stability we limit the analysis to the heat and freshwater feedbacks. For each case let the homotopy parameter be the independent variable, so $\gamma = \gamma(\xi_C)$ and the steady-state $\bar{\mathbf{x}} = \bar{\mathbf{x}}(\gamma(\xi_C), \xi_C)$, where C may indicate either heat (Q), or net evaporation (E). The requirement of constant $\Psi_A^{\phi,z}$ can be expressed as

$$\frac{\mathrm{d}\Psi_A^{\phi,z}}{\mathrm{d}\xi_C} = \left(\frac{\partial \Psi_A^{\phi,z}}{\partial \mathbf{x}}\right)^T \left(\frac{\partial \bar{\mathbf{x}}}{\partial \gamma}\frac{\mathrm{d}\gamma}{\mathrm{d}\xi_C} + \frac{\partial \bar{\mathbf{x}}}{\partial \xi_C}\right) = 0, \tag{4.10}$$

where $\partial \Psi_A^{\phi,z}/\partial \mathbf{x}$ denotes the N-dimensional vector whose entries are formed by taking the derivative of $\Psi_A^{\phi,z}$ with respect to each state variable. The definition of $\Psi_A^{\phi,z}$ implies that the only entries that are nonzero are those corresponding to the meridional velocities in the Atlantic at $\phi = 54°N$. The goal of our analysis is to compute $\mathrm{d}\gamma/\mathrm{d}\xi_C$, which is the shift of bifurcation point L_1 per unit feedback strength. Note, though, that $\mathrm{d}\gamma/\mathrm{d}\xi_C$ may vary along the path in parameter space from $\xi_C = 0$ to $\xi_C = 1$. So, $\mathrm{d}\gamma/\mathrm{d}\xi_C$ must be considered as a first order estimate of the total shift of L_1.

The following step is to compute the derivative of Eq. (4.4) with respect to ξ_C, and to evaluate it at $\xi_C = 0$:

$$\Phi\left(\frac{\partial \bar{\mathbf{x}}}{\partial \gamma}\frac{\mathrm{d}\gamma}{\mathrm{d}\xi_C} + \frac{\partial \bar{\mathbf{x}}}{\partial \xi_C}\right) + \frac{\partial \mathscr{F}}{\partial \gamma}\frac{\mathrm{d}\gamma}{\mathrm{d}\xi_C} + \mathbf{L}_C\left(\bar{\mathbf{x}} - \bar{\mathbf{x}}^R\right) = \mathbf{0}, \tag{4.11}$$

where Φ is the Jacobian of the ocean-only operator $\mathscr{F}$ introduced in Eq. (4.4). Next, we define the adjoint sensitivity vector $\mathbf{y}$ as the solution of

$$\mathbf{y}^T \Phi = -\left(\frac{\partial \Psi_A^{\phi,z}}{\partial \mathbf{x}}\right)^T. \tag{4.12}$$

Finally, we combine Eqs. (4.10-4.12) to find

$$\frac{\mathrm{d}\Psi_A^{\phi,z}}{\mathrm{d}\xi_C} = \mathbf{y}^T \frac{\partial \mathscr{F}}{\partial \gamma}\frac{\mathrm{d}\gamma}{\mathrm{d}\xi_C} + \mathbf{y}^T \mathbf{L}_C\left(\bar{\mathbf{x}} - \bar{\mathbf{x}}^R\right) = 0. \tag{4.13}$$
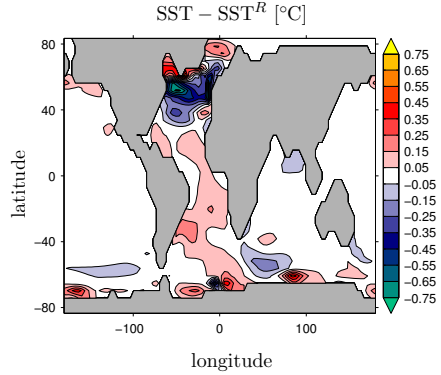
Figure 4.6: Difference between the SST field of the ON state solution at $\gamma = 0.2\,\mathrm{Sv}$ and the reference field (Fig. 4.1c).

The sensitivity of $\Psi_A^{\phi,z}$ to simultaneous variation of γ and ξ_C is now elegantly expressed as the inner product of the sensitivity to a change in forcing and a change in forcing per unit feedback strength. The change in forcing per unit feedback strength is split into a contribution from the anomalous freshwater flux and a contribution from the empirical atmosphere model. The compensation between these two defines the shift per unit feedback strength. By examining the spatial patterns of the adjoint sensitivity vector $\mathbf{y}$ and the forcing per unit feedback strength, we get insight into the physical mechanisms that are responsible for the shift of the saddle-node bifurcation.

In the following two subsections we discuss the term $\mathbf{y}^T \mathbf{L}_C \left(\bar{\mathbf{x}} - \bar{\mathbf{x}}^R \right)$ in Eq. (4.13), first for heat ($C = Q$), and then for net evaporation ($C = E$). The vector $\mathbf{L}_C \left(\bar{\mathbf{x}} - \bar{\mathbf{x}}^R \right)$ is the derivative of the empirical atmosphere model flux with respect to the homotopy parameter. Only the entries corresponding to surface variables are nonzero, and follow from Eq. (4.3):

$$
\frac{\partial F_C(i,j)}{\partial \xi_C} = p_1^{F_C}(i,j) \cdot \left(\mathrm{SST}(i,j) - \mathrm{SST}^R(i,j) \right) +
$$
$$
p_2^{F_C}(i,j) \cdot \left(\langle \mathrm{SST} \rangle_{NH} - \langle \mathrm{SST}^R \rangle_{NH} \right), \tag{4.14}
$$

The temperature contrast $\mathrm{SST}\text{-}\mathrm{SST}^R$ for $\gamma = 0.2\,\mathrm{Sv}$ is shown in Fig. 4.6. The most pronounced signal is seen in the Atlantic basin, where the reduction of the overturning strength (Ψ_A decreases by about $5\,\mathrm{Sv}$; Fig. 4.2a) causes strong and widespread cooling in the North Atlantic between 30°N and 60°N, and a moderate warming in the region south of 30°N. The increase in SST in the seas surrounding Greenland is related to the application of the freshwater perturbation. The local (equilibrium) response to this perturbation is enhanced upwelling of relatively saline water. Because the deeper water is also relatively warm, the SSTs increase, and more heat is lost to the atmosphere. Outside the Atlantic the SST contrast is confined to a number of small areas around Antarctica. Averaged over the Northern Hemisphere the SST difference is $\langle \mathrm{SST} \rangle_{NH} - \langle \mathrm{SST}^R \rangle_{NH} = -0.018\,°\mathrm{C}$.

4.4.3 Heat feedback

Figure 4.7a shows the part of $\mathbf{y}$ [Eq. (4.12)] that corresponds to the sensitivity of $\Psi_A^{\phi,z}$ to local changes in the surface heat flux, which is defined as positive when into the ocean. As

demonstrated by Dijkstra (2008) there is a linear relation between Ψ_A and the large-scale north-south density difference, which helps to explain the patterns in Fig. 4.7a. In examining a variety of different locations on the grid, we find that if at a grid point (i, j) a small, persistent perturbation is applied to the background heat flux, the first-order (steady-state) response is restricted to the local sea surface temperature, $\mathrm{SST}(i, j)$. The anomaly does not spread horizontally because the timescale associated with the standard atmospheric damping [Eq. (4.2)] is short compared to the advective timescale. It appears that such heat flux perturbation can only bring about a significant change in the large-scale density difference, and hence the overturning strength, if there is deep reaching downwelling at location (i, j). Consistent with this idea, the sensitivity of $\Psi_A^{\phi,z}$ to changes in the heat flux is strongly negative in the northeastern part of the Atlantic basin, which is the region where dense water sinks in the model. The strongly positive sensitivity in the region along the coast of South America also coincides with a zone of downwelling. In this area the vertical velocity is negative from the surface downward to a depth of about 1000 m due to the convergence of the northward-flowing extension of the Antarctic Circumpolar Current (the model's representation of the Malvinas current) and the southward-flowing western boundary current of the subtropical gyre (the Brazil current). In the largest part of the Atlantic that we did not discuss so far, the adjoint sensitivity of $\Psi_A^{\phi,z}$ to changes in the heat flux is weakly negative. In these areas there is no deep injection of surface waters. When a perturbation is applied here, it affects the MOC only indirectly by changing the surface velocity field.

As discussed more extensively by Cimatoribus et al. (2012), the local regression parameter field $p_1^{F_Q}$ (Fig. 4.7b), as found from the SPEEDO model, can be interpreted as the expression of different physical feedback processes. We remind the reader that the regression parameters include the net effect of changes in sea ice. The strong damping in the (sub)polar areas (negative values in Fig. 4.7b) is mainly accounted for by the fact that the area of the ocean covered by sea ice decreases with increasing SST, while the ocean is losing heat to the atmosphere in this region. A positive SST anomaly at a certain grid point is thus damped, because it causes a larger fraction of the grid cell area to be exposed to upward heat fluxes. The same applies conversely to negative SST anomalies. So, the positive temperature contrast in the seas surrounding Greenland (Fig. 4.6) induces cooling (Fig. 4.7c). The net effect on $\Psi_A^{\phi,z}$, however, is small because the sensitivity of $\Psi_A^{\phi,z}$ to changes in the heat flux is weak and of opposite sign in the Labrador Sea and the Nordic Seas. The SST changes around Antarctica are also damped due to sea ice dynamics, but the net effect on $\Psi_A^{\phi,z}$ is again small.

Outside the polar areas local heat flux changes are dominated by changes in latent heat release, followed in importance by changes in sensible heat and long-wave radiation (Cimatoribus et al., 2012). In the (northern) mid latitudes and in the equatorial region the local heat feedback enhances the standard atmospheric damping of SST anomalies. In the (sub)tropics, on the other hand, the heat feedback tends to amplify SST anomalies, probably as a result of the convection-evaporation feedback mechanism (Zhang et al., 1995; Chang et al., 1997). On climatically relevant time scales positive SST anomalies in these regions give rise to enhanced convection, and thus to increased low-level convergence, weaker surface winds and hence reduced latent heat loss by the ocean. It is worth noting that the different responses of latent heat are roughly consistent with the pattern of the local freshwater regression parameter $p_1^{F_E}$ (Fig. 4.8b). The strongly negative temperature contrast in the mid-latitude North Atlantic
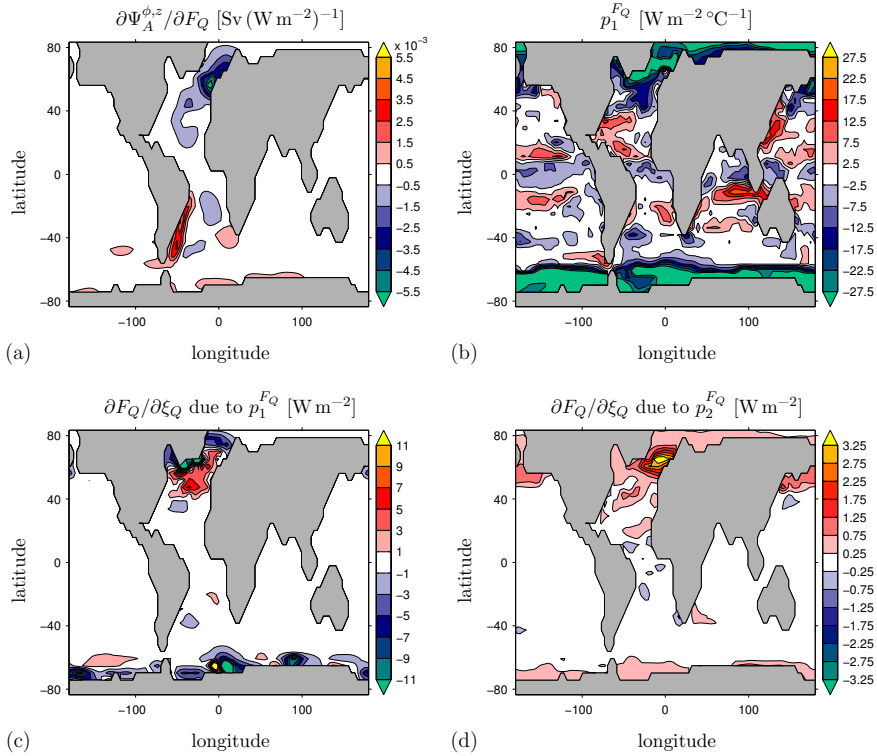
$\partial\Psi_A^{\phi,z}/\partial F_Q$ [Sv (W m^{-2})$^{-1}$]

$p_1^{F_Q}$ [W m^{-2} °C^{-1}]

$\partial F_Q/\partial\xi_Q$ due to $p_1^{F_Q}$ [W m^{-2}]

$\partial F_Q/\partial\xi_Q$ due to $p_2^{F_Q}$ [W m^{-2}]

Figure 4.7: Analysis of the heat feedback for the ON state solution at $\gamma = 0.2$ Sv. All heat fluxes are positive downward. (a) Map of the adjoint sensitivity of the steady-state Atlantic MOC strength with respect to local variations in heat flux. (b) Local regression parameter. (c,d) Derivative of the heat flux with respect to the homotopy parameter as in Eq. (4.14), with the flux due to the local regression parameter shown in (c) and that due to the large-scale coupling in (d).

mainly projects onto negative values of $p_1^{F_Q}$ and is therefore counteracted by local heating. Due to the negative adjoint sensitivity of $\Psi_A^{\phi,z}$ to changes in the heat flux this finally results in a decrease in overturning strength. The heat fluxes associated with the positive heat contrast south of 30°N are relatively weak, and have little effect on $\Psi_A^{\phi,z}$.

The combined effect of the different physical feedbacks leads to an overall sensitivity of $\Psi_A^{\phi,z}$ to the local heat feedback strength of -0.44 Sv per unit feedback strength.

Figure 4.7d shows the heat flux due to the large-scale feedback, calculated as the product of $\langle \text{SST} \rangle_{NH} - \langle \text{SST}^R \rangle_{NH} = -0.018$ °C and the large-scale regression parameter field $p_2^{F_Q}$. The large-scale heat feedback is entirely dominated by changes in insulation due to changing sea ice cover. Similar to the expression of this effect in the local regression parameter $p_1^{F_Q}$ (Fig. 4.7b) this causes $p_2^{F_Q}$ to be negative, and hence the large-scale interactive heat flux to be positive, in the subarctic region. Regions where the adjoint sensitivity of $\Psi_A^{\phi,z}$ to changes in the heat flux is strongly negative roughly overlap with regions of strong large-scale heat

fluxes, resulting in an overall sensitivity of $-0.22\,\mathrm{Sv}$ per unit feedback strength. The total response of $\Psi_A^{\phi,z}$ to enabling the heat feedback is thus $\mathbf{y}^T \mathbf{L}_Q \left(\mathbf{\bar{x}} - \mathbf{\bar{x}}^R \right) = -0.66\,\mathrm{Sv}$ per unit feedback strength.

4.4.4 Freshwater feedback

The part of $\mathbf{y}$ [Eq. (4.12)] corresponding to the sensitivity of $\Psi_A^{\phi,z}$ to local changes in the net evaporative flux (Fig. 4.8a) shows a less localized pattern than the sensitivity to the heat flux (Fig. 4.7a), which is due to the fact that sea surface salinity anomalies are not damped by the atmosphere. By applying a small, persistent perturbation to the local freshwater flux at a number of different locations, we find for each case that such perturbation produces a steady-state with a large-scale anomaly in the sea surface salinity, in contrast to the localized response of SST to local heat flux perturbations. A positive perturbation (enhanced evaporation) typically causes sea surface salinities to increase upstream, and to decrease downstream of the location where the perturbation is applied. It thus appears that perturbations in the freshwater flux can influence the MOC strength directly by exerting a remote influence on the salinity field in the regions of strong downwelling, and hence on the large-scale density contrast. Consistently, the sensitivity of $\Psi_A^{\phi,z}$ to changes in the net evaporative flux is positive in the Atlantic basin, except in the region close the southern coast of South America. Since grid cell area decreases with latitude, a smaller change in net evaporation (which is measured in $\mathrm{mm\,d}^{-1}$) is needed at the equator than at higher latitudes to produce the same change in the total amount of salt in a grid cell. The fact that the strongest sensitivities are found at the equator therefore fits with the idea that evaporation changes have a remote, but direct effect on the salinity in the downwelling region and hence on the strength of the MOC.

The local freshwater regression parameter $p_1^{F_E}$ (Fig. 4.8b) is largest in magnitude in the subtropics and tropics. The evaporation-convection feedback (Zhang et al., 1995) is at work in these areas: higher SSTs lead to enhanced convection and stronger precipitation. The SST contrast is positive in the (sub)tropical part of the Atlantic where $p_1^{F_E}$ is negative. This means that the evaporation-convection feedback leads to net input of freshwater into the Atlantic (Fig. 4.8c), and hence to a decrease in overturning strength. In the mid latitudes the parameter $p_1^{F_E}$ is weakly positive, implying that net evaporation is enhanced at higher SSTs. A significant part of the negative mid latitude SST contrast projects onto the area of positive $p_1^{F_E}$ and thus leads to a smaller overturning rate. The positive SST contrast at the equator does not have a significant effect on $\Psi_A^{\phi,z}$, though. In the polar areas and south of Greenland the local feedback causes enhanced freshwater input at higher SSTs, which is probably a combined effect of enhanced discharge from the land-surface and increased precipitation. The positive temperature contrast in the Labrador and Nordic Seas therefore results in net freshwater input and hence in a decrease in $\Psi_A^{\phi,z}$. The overall sensitivity of $\Psi_A^{\phi,z}$ to the local freshwater feedback strength equals $-0.72\,\mathrm{Sv}$ per unit feedback strength.

The dominant signal in the large-scale freshwater regression parameter $p_2^{F_E}$ is the signature of the southward shift of the intertropical converge zone (Yin et al., 2006) in response to a weaker overturning circulation (Fig. 4.8d). However, because the adjoint sensitivity of $\Psi_A^{\phi,z}$ to changes in the net evaporative flux is relatively constant just north of the equator, the ITCZ shift hardly affects the Atlantic overturning rate. The sensitivity to the large-scale feedback
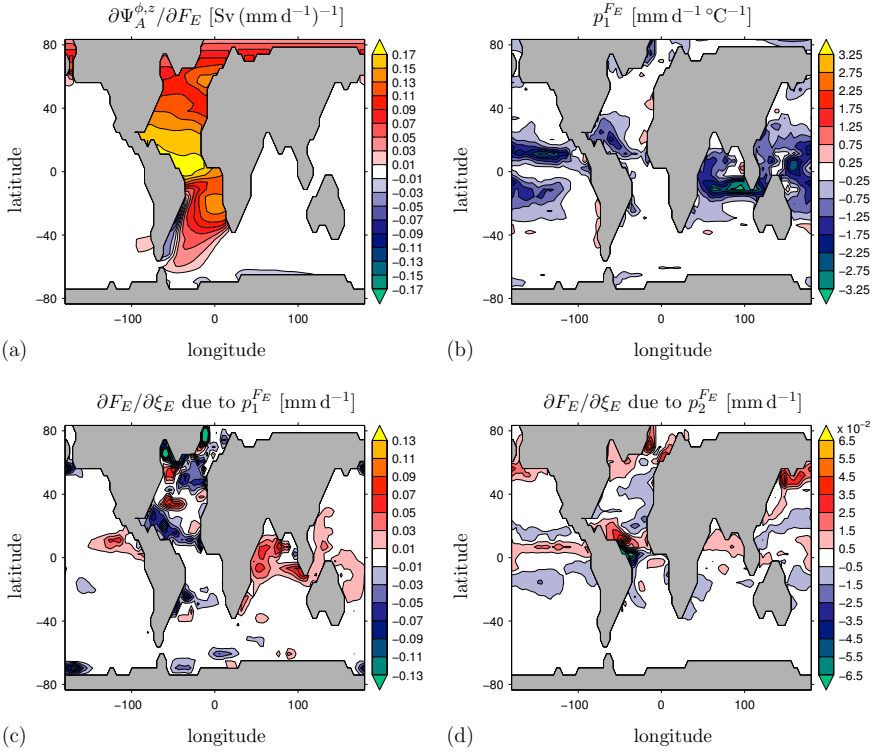
Figure 4.8: As Fig. 4.7, but for the freshwater feedback. Positive fluxes represent net evaporation.

strength is therefore only 0.03 Sv per unit feedback strength. The total sensitivity of $\Psi_A^{\phi,z}$ to the freshwater feedback is hence $\mathbf{y}^T \mathbf{L}_E \left(\bar{\mathbf{x}} - \bar{\mathbf{x}}^R \right) = -0.69$ Sv per unit feedback strength.

4.4.5 Shift of saddle-node bifurcation L_1

As explained in subsection 4.4.2, the final aim of our analysis is to calculate $d\gamma/d\xi_C$ from Eq. (4.13),

$$\frac{d\gamma}{d\xi_C} = -\mathbf{y}^T \mathbf{L}_C \left(\bar{\mathbf{x}} - \bar{\mathbf{x}}^R \right) \left(\mathbf{y}^T \frac{\partial \mathscr{F}}{\partial \gamma} \right)^{-1}, \tag{4.15}$$

which provides a first order estimate of the shift of bifurcation point L_1. The term $\mathbf{y}^T \mathbf{L}_C \left(\bar{\mathbf{x}} - \bar{\mathbf{x}}^R \right)$ was computed in subsections 4.4.3 and 4.4.4 for feedbacks acting through the heat ($C = Q$) and freshwater ($C = E$) fluxes, respectively. The term $\mathbf{y}^T \frac{\partial \mathscr{F}}{\partial \gamma}$ represents the sensitivity of $\Psi_A^{\phi,z}$ to γ and can be thought of as the slope of the tangent to the bifurcation diagram at $\gamma = 0.2$ Sv. It follows from Eq. (4.1) that $\frac{\partial \mathscr{F}}{\partial \gamma}$ corresponds to the perturbation pattern $-F_E^p$. Using the adjoint sensitivity to net evaporative fluxes (Fig. 4.8a), the sensitivity of Ψ_A to γ is found to be -0.0682 Sv mSv^{-1}. The total response of Ψ_A to enabling the heat

feedback (-0.66 Sv per unit feedback strength) can thus be compensated by a shift in γ of $d\gamma/d\xi_Q = -9.7$ mSv per unit feedback strength. The actual shift is smaller (-5.2 mSv, see Table 4.1) due to the direct negative feedback between the interactive forcing and SST. The total response of Ψ_A to enabling the freshwater feedback (-0.69 Sv per unit feedback strength) can be counteracted by a shift in γ of $d\gamma/d\xi_E = -10.1$ mSv per unit feedback strength, which is very close to the actual shift of -8.7 mSv (Table 4.1). The fact the first order estimates of the shifts are close to the actual values indicates the relevance of the physical mechanisms described above for explaining the changes in the stability of the ON state.

4.5   Summary and Discussion

Using a global hybrid ocean-atmosphere model and techniques from numerical bifurcation theory to solve for exact steady-states of this model, we investigated the changes in the multiple equilibria regime of the Atlantic Meridional Overturning Circulation (MOC) due to atmospheric feedbacks. The main new element of this study is a systematic assessment of how different interactive ocean-atmosphere fluxes affect the position of the two saddle-node bifurcations that bound the multiple equilibria regime of the MOC.

Atmospheric feedbacks cause the saddle-node bifurcation that terminates the present-day (ON) branch of solutions (L_1) to occur at a smaller magnitude of the freshwater perturbation (γ) than in the ocean-only model (Fig. 4.4). Feedbacks acting through the freshwater flux appear to contribute most to the destabilization of the ON state. Their effect is probably enhanced by the direct impact of interactive heat fluxes on the sea surface temperature (SST) field. The implication of this result is that, if the freshwater input into the northern part of the North Atlantic increases gradually in time, the threshold value for collapse will be reached sooner as a result of air-sea interactions. If, instead, the present-day state of the ocean is perturbed by a temporary freshwater pulse, a smaller magnitude or shorter duration of the pulse will suffice to force a transition to the collapsed (OFF) state (Dijkstra et al., 2004).

In general, the MOC will recover from a collapse induced by a temporary perturbation if the unperturbed state is in the unique regime, but it will remain collapsed when it is in the bistable regime. This means that the bifurcation point that terminates the OFF branch of solutions (L_2) must also be considered when assessing the nonlinear sensitivity of the MOC to freshwater perturbations. The hybrid coupled model predicts that L_2 occurs at a larger value of γ. Although its position on the bifurcation diagram is uncertain, the consequence might be that the present-day state of the climate is brought to the unique regime as a result of atmospheric feedbacks.

Atmospheric feedbacks arise because changes in the MOC induce changes in the atmospheric momentum, heat, and freshwater fluxes, which in turn influence the strength and pattern of the MOC. Using adjoint methods we identified which physical mechanisms are responsible for the shift of L_1. We analyzed the sensitivity of the MOC to the feedback strengths of heat and freshwater, which dominate the response (section 4.4). The impact of interactive heat fluxes on the MOC stability is roughly limited to the region of the North Atlantic subpolar gyre (Fig. 4.7a), where the regression coefficients of the hybrid model represent atmosphere and sea-ice dynamics that act to reduce the negative SST anomalies (Fig. (4.6)). Interactive freshwater fluxes, on the other hand, have an effect everywhere in the Atlantic

basin (Fig. 4.8a). We identified the (sub)tropical evaporation-convection feedback (Zhang et al., 1995; Chang et al., 1997), the midlatitude coupling between SST and net evaporation, and the polar changes in precipitation and runoff as important mechanisms for the MOC stability. Due to the SST signature of the MOC decrease (Fig. 4.6) their net effect is to shift the saddle-node L_1 to smaller values of γ. The shift of the ITCZ captured by the large-scale regression parameter was found to have little effect on the ON state MOC stability.

The qualitative results on the shifts of the saddle-node bifurcations and the mechanisms derived from the adjoint sensitivity are more important than the quantitative shifts in itself. We need to recall here that the hybrid model is based on regression coefficients that were derived with reference to the ON state with $\gamma = 0$. Furthermore, we noted that the small response to winds being interactive is due to the relatively high lateral viscosity of the ocean model. The results of Arzel et al. (2011) suggest that this deficiency only affects the position of L_2. In addition to possible direct effects, which only modify the strength of the overturning but not its pattern, interactive momentum fluxes influence the OFF state SST field (and hence all atmospheric fluxes) indirectly by modifying the surface expression of the overturning. We found that this effect is not reproduced by THCM-C. As a consequence of these limitations, predictions for the shift of L_1 will be more reliable than for the shift of L_2.

Another weakness of the hybrid model approach is that certain feedbacks may be underestimated or even ignored. First, although the linearized effect of sea-ice on the heat-flux feedback is taken into account through the regression parameters (Cimatoribus et al., 2012), the full nonlinear response due to sea-ice dynamics is not captured. Furthermore, it should be realized that the effect of the hydrological cycle on the stability of the MOC is a very complex issue. It is possible that for a different mean climate, other feedbacks dominate over the ones that were captured in the regression coefficients, which were derived with respect to the present climate. For example, Tziperman and Gildor (2002) pointed out that the temperature-precipitation feedback, according to which there is less precipitation over higher latitudes during colder periods, may stabilize the thermohaline circulation, in contrast to our results. Additional feedbacks may also arise if other parameters, such as CO_2 concentration, are varied besides the high latitude input of freshwater. For instance, Latif et al. (2000) showed how tropical air-sea interactions may stabilize the MOC in a greenhouse warming scenario.

Our motivation to study the effect of atmospheric feedbacks stems from the apparent absence of a multiple equilibria regime in state-of-the-art IPCC-AR4 models. The results in this chapter show (i) that atmospheric feedbacks reduce the size of the multiple equilibria regime, or hysteresis width, of the Atlantic MOC; and (ii) that the present-day state is more vulnerable to long-lasting increases in the northern high latitude freshwater input when air-sea interactions are taken into account. Emphasizing that the results are mainly qualitative, it is not expected that atmospheric feedbacks remove the multiple equilibria regime. In agreement with Hofmann and Rahmstorf (2009), we argue that the feedbacks are too weak to induce substantial changes in the positions of the saddle node bifurcations. The extent of the multiple equilibria regime in state-of-the-art GCMs is hence more likely affected by biases in the GCMs (Huisman et al., 2010; Drijfhout et al., 2011) then by the effect of atmospheric feedbacks.

5

Sensitivity of a strongly eddying global ocean to North Atlantic freshwater perturbations

The strongly eddying ("$R_{0.1}$") version of the Parallel Ocean Program (POP) is used in two 45-year simulations to investigate the response of the Atlantic Meridional Overturning Circulation (AMOC) to strongly enhanced Greenland run-off. One is a reference simulation, while in the other an anomalous 0.5 Sv freshwater flux is applied. For comparison, a similar set of experiments is performed using a non-eddying ("$x1$") version of POP. The aim is to identify the signature of the salt advection feedback in the two configurations. The freshwater input leads to a quantitatively comparable reduction of the AMOC in the two models. However, whereas the AMOC is proportional to the meridional density contrast in $x1$, in agreement with the concept of the salt advection feedback, the two quantities are negatively correlated in $R_{0.1}$. To examine the importance of transient effects in the AMOC vs. density relation, the results of $R_{0.1}$ are related to water mass transformation theory. The freshwater forcing leads to a reduction of the rate of light to dense water conversion in the North Atlantic, but there is no change in dense to light transformation elsewhere. This means that high density layers are continuously deflating. The steady-state concept of the adiabatic pole-to-pole circulation is hence of limited value in this case. As a next step, the effect of the AMOC reduction on the basin-wide advection of freshwater is considered. The $x1$ results show a change of the net freshwater advection that is consistent with the salt advection feedback. However, for $R_{0.1}$, the net freshwater advection into the Atlantic basin appears to be unaffected, despite the significant change in the large-scale velocity structure.

5.1 Introduction

Computational resources put constraints on the resolution that can be used for the ocean component of a global climate model (GCM). A typical horizontal grid spacing for such a model is one degree. This is too coarse to resolve the first baroclinic Rossby radius of deformation, which is a fundamental horizontal scale of mesoscale processes. As a result, the representation of the oceans in a GCM is significantly different from observations in several crucial aspects. For example, the data presented by Bower et al. (2009) shows that recently formed deep water follows irregular interior pathways. This is in contrast with the idea that this water flows southward as part of a relatively steady, coherent deep western boundary current, such as is suggested by coarse-resolution ocean models (Drijfhout et al., 1996). The trajectories taken by water parcels are much better represented in a high-resolution, eddy-resolving model (Bower et al., 2009), and the dispersion of surface properties is markedly different in non-eddying and eddy-resolving models (Weijer et al., 2012). As a result, low-resolution models may provide incorrect estimates of the ocean's sensitivity to external forcing. The topic of the this study is the sensitivity of the Atlantic Meridional Overturning Circulation (AMOC) to anomalous high-latitude freshwater forcing. The question that will be addressed is how estimates of this sensitivity differ between models in which eddies are parameterized, and models that explicitly resolve eddies.

These issues are also studied by Weijer et al. (2012), who used the Parallel Ocean Program (POP) in two configurations, with horizontal resolutions of $1°$, and $0.1°$, respectively. In that paper, it is shown that the transient response to the addition of $0.1\,\mathrm{Sv}$ ($1\,\mathrm{Sv} = 1 \times 10^6\,\mathrm{m}^3\,\mathrm{s}^{-1}$) of freshwater is significantly different between the two configurations. In the low-resolution version of the model, the AMOC strength levels off after a rapid initial decline, while in the high-resolution configuration, the AMOC decline is more gradual and persistent. In addition, only in the high-resolution configuration is the response found to depend strongly on where the anomalous freshwater forcing is applied. As shown in Weijer et al. (2012), the initial decline of the AMOC in these simulations can be related to the behavior of convection, meaning that the efficiency of the anomalous freshwater transport to the sites of convection is an important factor in explaining the differences between the simulations (Marsh et al., 2010). In this chapter, we continue the analysis of Weijer et al. (2012), but instead focus on differences between the two configurations in processes acting at the scale of the basin. Specifically, we frame the discussion around the question of what the contribution of the salt advection feedback is to the reduction of the AMOC.

The concept of the salt advection feedback is commonly illustrated with a two-box model, as originally proposed by Stommel (1961). As discussed in more detail in section 1.2, the basic idea is that the overturning is proportional to a meridional density gradient, while, in turn, the overturning enhances the meridional density gradient by reducing the salinity gradient. The temperature advection feedback is commonly assumed to be less important due to the strong damping of temperature anomalies by the atmosphere. Whether the three-dimensional ocean circulation has analogous dynamics is not a simple question. In coarse-resolution ocean-climate models the salt advection feedback is found to be responsible for the existence of multiple equilibria (Rahmstorf, 2000). Hence, abrupt transitions between different states may occur in these models. Anthropogenic warming makes the question of whether the AMOC may undergo such transition (or "collapse") a timely issue to tackle. Under-

standing the nonlinear response of the AMOC to freshwater perturbations is also vital for the interpretation of rapid climate changes in the past, the Dansgaard-Oeschger and Heinrich events, as derived from ice-core records (Alley et al., 2003). However, due to computational constraints, the detection of multiple equilibria is currently not feasible for global eddying models. Therefore, the approach taken in this chapter is to examine the analogy between the conceptual model of Stommel (1961) and the non-eddying and eddy-resolving versions of POP, using transient decadal time-scale simulations of the response to anomalous freshwater forcing. Specifically, we focus on (1) the relation between AMOC strength and meridional density distribution, and (2) the effect of changes in the AMOC on the basin-wide freshwater transport.

As anomalous freshwater forcing, we consider enhanced runoff from the Greenland Ice Sheet (GrIS). Observations indicate that the mass balance of the ice sheet is currently negative (Rignot et al., 2011), while future projections suggest that discharge from the GrIS will increase further in the course of the 21st century (Mernild et al., 2010). However, our aim is not to provide a realistic GrIS melting scenario, but to isolate the oceanic response to a large freshwater perturbation with a realistic pattern. We therefore enhance the amplitude of the GrIS discharge to 0.5 Sv.

Scenarios more relevant for future climate change have been explored extensively in low-resolution models, and may be compared to the results with the non-eddying version of POP that will be described here. For example, using the Modular Ocean Model (MOM) at a horizontal resolution of about 2°, Gerdes et al. (2006) investigated the role of different ocean-atmosphere boundary conditions in determining the response of the Atlantic to GrIS freshwater anomalies. They show that the strength of the AMOC decreases by about 50% in 100 years in response to an integrated freshwater perturbation of 0.1 Sv. Furthermore, Stammer (2008), use the Massachusetts Institute of Technology (MIT) general circulation model at a horizontal resolution of 1° in a 50-year simulation with enhanced runoff from Greenland (the integrated flux is not provided). Jungclaus et al. (2006) consider the AMOC change in the ECHAM5-OM1 model (1.5° horizontal circulation in the ocean model) under different scenario's of GrIS melting and greenhouse forcing. For high melting estimates, the AMOC reduction is about 42%, compared to 30% for the SRES-A1B scenario only. The paper of Hu et al. (2009) considers the effect of enhanced GrIS melting in transient simulations with the Community Climate System Model (CCSM) version 3 under the SRES-A1B scenario. Note that the ocean component of CCSM is POP, which is configured at the same 1° horizontal resolution as considered in this study. In this case, the AMOC strength decreases by about 50% in 2100, but only when the GrIS melting flux is very strong, being 0.3 Sv in 2100.

The plan of this chapter is as follows: A description of the model and the simulations used in this study is given in section 5.2. The response of the AMOC to the freshwater perturbation is presented in section 5.3. Section 5.4 discusses the relation of the AMOC to the meridional density distribution, and in section 5.5, the role of the AMOC in the freshwater budget of the Atlantic is analyzed. The chapter concludes with a summary and discussion in section 5.6.

5.2   Model and simulations

The global simulations described here are performed using the Parallel Ocean Program (POP, Dukowicz and Smith, 1994), developed at Los Alamos National Laboratory. We consider the same two configurations as Weijer et al. (2012). The strongly eddying configuration, indicated by $R_{0.1}$, has a nominal horizontal resolution of 0.1° and is the same as that used by Maltrud et al. (2010). The low resolution configuration ($x1$), on the other hand, has the nominal 1 degree horizontal resolution of the Community Climate System Model (CCSM). The two versions of the model are configured to be consistent with each other, where possible. There are, however, some notable differences, which are discussed in full in the supplementary material of Weijer et al. (2012). Here, we note that the $R_{0.1}$ configuration has a tripolar (Murray, 1996) grid layout, with poles in Canada and Russia, while the $x1$ configuration is based on a dipolar grid, with the northern pole placed onto Greenland. In the $R_{0.1}$ configuration, the model has 42 non-equidistant z-levels, increasing in thickness from 10 m just below the upper boundary to 250 m just above the lower boundary at 6000 m depth. In addition, bottom topography is discretized using partial bottom cells, creating a more accurate and smoother representation of topographic slopes. In contrast, in the $x1$ configuration, there are 40 levels (with the same spacing as in $R_{0.1}$), and the partial bottom cell approach is not used.

Since this study focuses on the impact of explicitly resolved mesoscale transports on the decadal response of the global ocean to freshwater flux perturbations, we restrict the timescales introduced by the surface forcing to seasonal. The atmospheric state is based on the repeat annual cycle (normal-year) Coordinated Ocean Reference Experiment (CORE[#]) forcing dataset (Large and Yeager, 2004), with the 6-hourly forcing averaged to monthly. Wind stress is calculated offline using the Hurrell Sea Surface Temperature (SST) climatology (Hurrell et al., 2008) and standard bulk formulae. Evaporation and sensible heat flux are calculated online using bulk formulae and the model predicted SST. Precipitation is also taken from the CORE forcing dataset. Monthly river runoff from 46 major rivers (Fekete et al., 2000) is added to the freshwater flux at the locations of the actual outflow, with the remaining runoff distributed evenly along the coasts of all of the continents. In the model all freshwater fluxes are converted to equivalent virtual salt fluxes, so that no volume flux is associated with them. In the presentation of our results, though, we refer to these salt fluxes as if freshwater is exchanged across the upper boundary of the model. Ice cover is prescribed based on the −1.8 °C isoline of the SST climatology, with both temperature and salinity restored on a timescale of 30 days under diagnosed climatological ice. Consequently, whereas in reality the distribution of sea ice may respond to changes in the surface circulation of the Arctic and subpolar regions, thus modifying the magnitude and pattern of ice-ocean heat and freshwater exchange, this feedback is not represented in the simulations described here.

Our $R_{0.1}$ experiments branch off from the end of year 75 of a simulation spun up from rest, the results of which are described in Maltrud et al. (2010). In this spin-up integration global salinity drift was controlled by applying a relaxation condition with a timescale of one year to the surface salinity in the open ocean, additional to the climatological precipitation, (SST-dependent) evaporation, and runoff specified above. Because such forcing would artificially
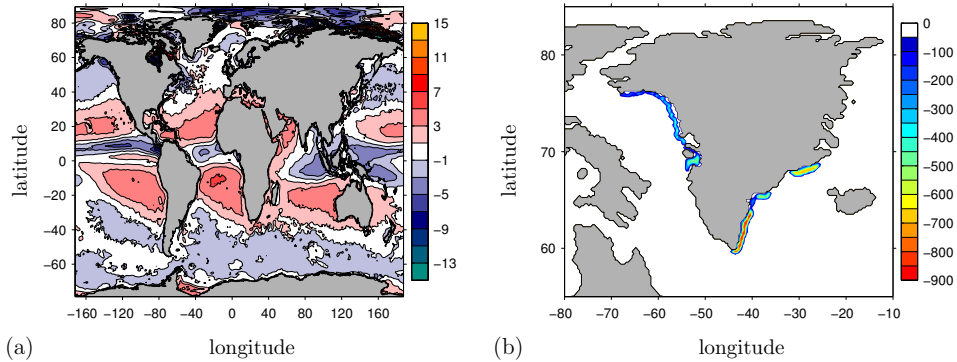

[#]see http://www.clivar.org/organization/wgomd/core/core.php

Figure 5.1: Annual mean fields of the seasonally varying virtual salt flux for the $R_{0.1}$ configuration, converted to units of mm day^{-1} and with positive values indicating evaporation. (a) Reference flux, consisting of climatological evaporation, precipitation, and runoff, and the diagnosed flux implied by the restoring condition in the spin-up integration. Apart from minor changes due to evaporation depending on SST, this flux is constant throughout the years and the same in both simulations. This plot shows the field for year 76 in REF. (b) Runoff from Greenland as applied in PERT.

remove salinity perturbations (Marsh et al., 2010), the dependence of the salt flux on sea surface salinity is removed in the experiments described here. This is done by diagnosing the salt flux implied by the restoring condition from the next 5 years (years 76-80) of the spin-up simulation and adding the result to the climatological fluxes. The annual mean field of the total flux is plotted in Fig. 5.1a for $R_{0.1}$ and shows a good agreement with observations (e.g. the HOAPS dataset as in Fig. 16 of Andersson et al., 2010).

In contrast to the $R_{0.1}$ configuration, in the $x1$ configuration, the integrated freshwater budget of the Atlantic and Arctic Oceans (to be discussed in section 5.5) does not reach equilibrium within a 75 year spin-up. Therefore, for $x1$, a sufficiently equilibrated state is obtained by integrating the model for an additional 500 years under mixed boundary conditions. The $x1$ simulations then branch off from this state.

For both configurations, we present the results of two experiments: an unperturbed reference simulation (REF) and an experiment with enhanced runoff from the GrIS (PERT). The REF experiment with the $R_{0.1}$ configuration is also used by Weijer et al. (2012) (referred to there as C-Mixed), who present a comparison with observations in the auxiliary material of their paper. The anomalous flux in the PERT simulations is applied throughout the duration of the experiments. Its spatial distribution, shown in Fig. 5.1b for $R_{0.1}$, is based on observed values of run-off and calving (Rignot and Kanagaratnam, 2006). The integrated flux is much larger than observed, however, varying seasonally around an annual mean amplitude of 0.5 Sv, and reaching a maximum amplitude of 0.9 Sv in July. The two simulations are continued for 45 years and 100 years for the $R_{0.1}$ and $x1$ configurations, respectively. For all simulations, monthly mean data were saved. In addition, daily fields were saved for the years 76 and 116 for the $R_{0.1}$ configuration to allow a better reconstruction of the overturning circulation in density coordinates (to be discussed in section 5.45.4.2).
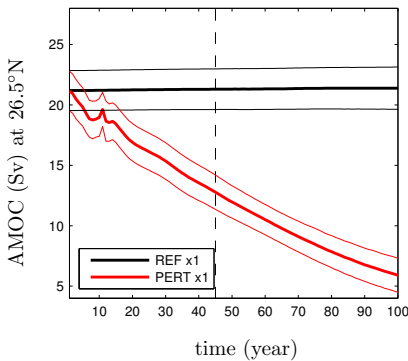
Figure 5.2: Strength of the AMOC at 26.5°N for the x1 POP configuration, diagnosed as the maximum value of Ψ (Eq. 5.1), which occurs at a depth of about 1 km. In this and subsequent time series plots, the thick lines are yearly mean values, while the thin lines represent the 1-year root-mean-square deviation. The dashed line drawn at 45 years indicates the duration of the corresponding $R_{0.1}$ simulations.

5.3   Overturning circulation

A first order picture of the evolution in the basin-scale overturning circulation is obtained by calculating the meridional overturning stream function in depth coordinates, given by

$$\Psi(\phi,z,t) = -r_0 \cos\phi \int_{\lambda_W}^{\lambda_E} \int_{-H}^{z} v(\lambda,\phi,z',t)\, \mathrm{d}z'\mathrm{d}\lambda, \tag{5.1}$$

where λ is longitude, ϕ latitude, z the height above mean sea level, t time, r_0 the radius of Earth, λ_W (λ_E) the (latitude dependent) longitude of the western (eastern) boundary of the basin, H the local bottom depth, and $v(\lambda,\phi,z,t)$ the meridional velocity.

First, the results for the *x1* simulations are briefly described. Figure 5.2 shows the maximum value of Ψ at 26.5°N, which is the latitude of the RAPID observational array (Cunningham et al., 2007). For the control simulation (REF), the mean is 21 Sv, which is somewhat stronger than the observations suggest. The root-mean-square deviation is 1.7 Sv, which is clearly smaller than what is observed (± 6 Sv). The transient response of the AMOC to the freshwater perturbation (PERT) is characterized by a rapid decline in the first 8 years, followed by a slight resumption up to year 11, after which the decrease continues until the end of the simulation. After 45 years (the duration of the $R_{0.1}$ simulations), the AMOC has weakened by 8.5 Sv. Even 100 years after the onset of the perturbation, the AMOC strength is still decreasing. The decline of the AMOC strength is a meridionally coherent signal (not shown). As a result, it affects the basin-wide divergence of freshwater transport, as will be shown in section 5.5. [][t]

Next, we discuss the results for the $R_{0.1}$ configuration. The strength of the Ψ at 26.5°N is plotted in Fig. 5.3a. Comparison with Fig. 5.2 shows that the average strength of the AMOC in the REF case (22 Sv) is similar to that in the *x1* configuration. The typical 1-year root-mean square deviation (about 1.5 Sv) is also comparable. However, the inter-annual variability evident in the $R_{0.1}$ results is absent in the *x1* configuration. Although a long-term adjustment to a quasi equilibrium situation may still be underway, part of the year-to-year variations must be attributed to intrinsic variability. Note here that the surface forcing does not introduce time scales longer than 1 year. Because, in addition, part of the short-term variability is removed by using monthly averaged forcing, it is not surprising that the AMOC
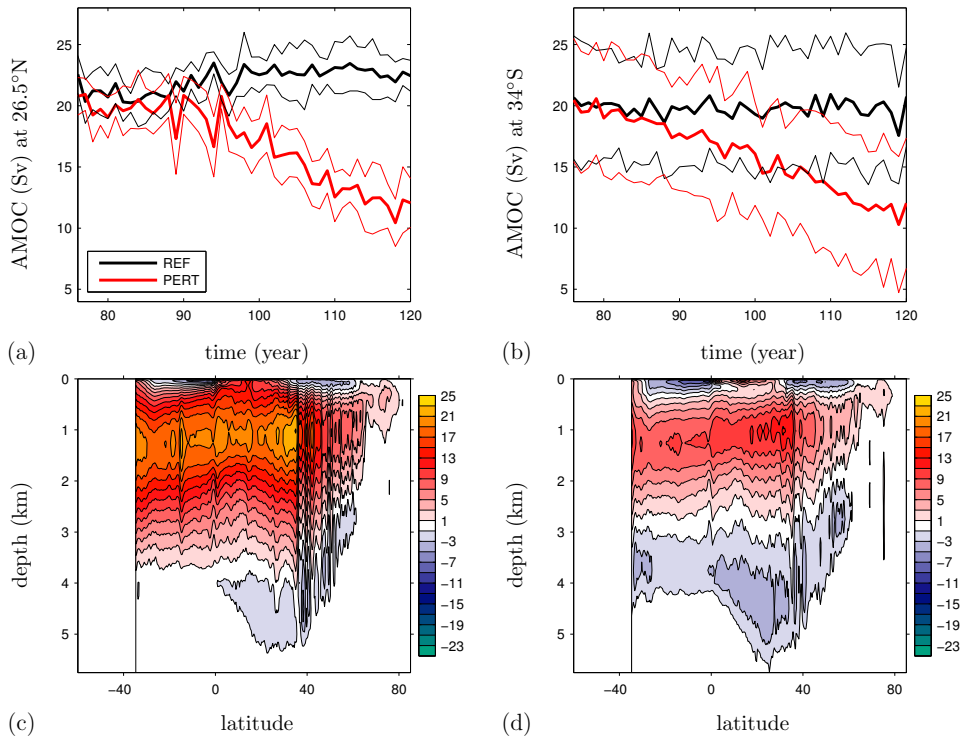
Figure 5.3: The AMOC for the $R_{0.1}$ POP configuration. (a,b) AMOC strength at (a) 26.5°N and (b) 34°S, diagnosed as Ψ (Eq. 5.1) at the depth of its maximum, which is about 1 km. (c,d) Stream functions (contour interval 2 Sv) of the annual mean AMOC in PERT for (c) year 76 and (d) year 116.

variability is still much larger in the observations (± 6 Sv, Cunningham et al., 2007) than in the highly eddying version of the model.

In the $R_{0.1}$ PERT simulation, the AMOC strength shows a small decrease in the first three years after the onset of the freshwater perturbation, attaining an annual mean value below the weakest annual mean strength in REF in year 78. Only after about two decades, however, is there a persistent, gradual decline in overturning strength, resulting in an anomaly with respect to the REF experiment that clearly exceeds the intra-annual variations. An explanation of what determines the timing of the response is outside the scope of this study. We note, however, that AMOC variations propagate at the Kelvin wave speed south of 34°N, but at the much slower advection speed north of that latitude. As a result there is at least a 6 year time lag between variations in Labrador Sea mixed layer depth and AMOC variations at 26.5°N (Zhang, 2010). In addition, the access of the freshwater anomalies to the sites of deep convection is limited by the narrow boundary currents in the basin (Marsh et al., 2010; Weijer et al., 2012). The year 120 anomaly of the annual mean strength equals -10.4 Sv, exceeding the response in *x*1 configuration by about 2 Sv. Furthermore, the anomaly is about 50% larger than the anomaly in the equivalent simulation with a 0.1 Sv integrated input of

freshwater described by Weijer et al. (2012). In contrast to their results, however, there is no indication that the overturning strength is close to reaching a new equilibrium in the final stage of the PERT experiment.

As will be discussed in section 5.5, changes in the AMOC strength are expected to affect the transport of freshwater at the southern margin of the Atlantic at 34°S. Figure 5.3b) shows that for both experiments the yearly mean strength of the AMOC at 34°S is similar to that at 26.5°N. Whereas the intra-annual variability is larger, year-to-year variations appear to be smaller at 34°S. In PERT, the AMOC strength decreases almost linearly, first reaching an annual mean value lower than that seen in REF in year 89. At the end of the simulation (year 120) the anomaly in annual mean strength equals -8.3 Sv.

Comparison of panels c and d of Fig. 5.3 shows that there is no change in the depth of maximum overturning between year 76 and year 116 of the PERT experiment. This is also true for the minimum of the stream function at 4.5 km depth, representing northward bottom flow, although the strength of this negative cell increases by roughly 2 Sv between year 76 and year 116. Although the rate of overturning has changed, the pattern of Ψ is essentially not modified during the simulation, which suggests that the AMOC does not experience a transition ("collapse") to a different state. The integration period is, however, quite short and it is possible that when the simulation would be continued, the AMOC would eventually collapse.

5.4 Relation between overturning strength and meridional density distribution

In order to investigate how to draw an analogy between Stommel's (1961) conceptual model of the salt advection feedback and the three-dimensional ocean circulation, we consider in this section the relation between AMOC strength and the meridional density distribution. First, we examine the North-to-South density contrast as in Rahmstorf (1996) and find that it correlates positively to the AMOC for the $x1$ configuration, as assumed in the conceptual model, but negatively for $R_{0.1}$. For the latter, a further analysis is therefore performed which builds on the framework of the adiabatic pole-to-pole circulation put forward by Wolfe and Cessi (2009, 2011). It turns out that, on the time scale considered here, transient effects cannot be ignored.

5.4.1 Relation to density contrast

As reviewed in the introduction of chapter 2 and by, for example, Rahmstorf (1996) and De Boer et al. (2010), theoretical scaling relations indicate that the AMOC is driven by a meridional density contrast. Although counterexamples are provided by De Boer et al. (2010), there are several model results that indeed show a positive relation between the AMOC strength and meridional density contrast (Rahmstorf, 1996; Dijkstra, 2008), or meridional pressure difference (Griesel and Maqueda, 2006). The theoretical relations are based on the assumption of steady state conditions, while we apply the concept to transient model results. However, rather than establishing the validity of the scaling relation, we want to test whether the salt advection feedback is involved in the response of the AMOC. For this to be
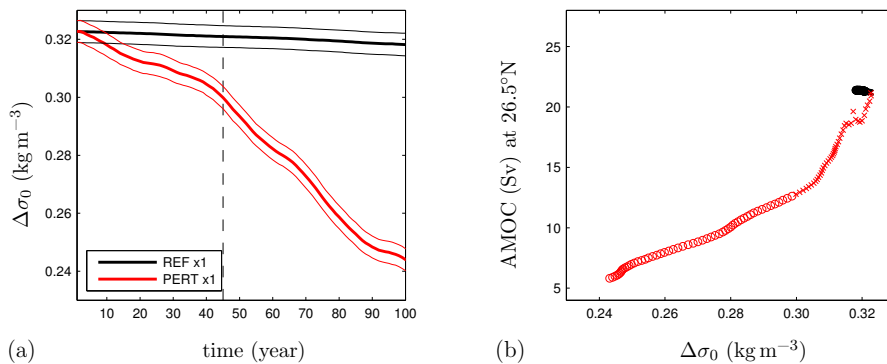
Figure 5.4: (a) Time series of the meridional density difference $\Delta\sigma_0$ for the x1 configuration. The figure shows the difference in potential density (referenced to the surface) between two latitudinal strips (50-55°N and 35-40°S, as in Rahmstorf (1996)) at the model level at 918 m depth. (b) Relation between AMOC strength at 26.5°N and $\Delta\sigma_0$, based on yearly means. Crosses indicate values from years 1-45, while circles indicate values from years 46-100. Similar relations hold for other latitudinal ranges and for other depths.

true, a positive relation between AMOC strength and meridional density contrast must also hold on the time scale of the simulations described here. Note that in the conceptual model of Stommel (1961), the dependence of the flow strength on the density difference is expressed by a diagnostic relation, see Eq. (1.8).

We present here the meridional potential density contrast ($\Delta\sigma_0$, referenced to the surface) at a depth of 918 m, where the difference is taken between the latitudinal strips 50-55°N and 35-40°S, as in Rahmstorf (1996). Figure 5.4a shows that $\Delta\sigma_0$ reduces in response to the freshwater perturbation. When plotted against Ψ, a positive correlation is evident (Fig. 5.4b), although the relation is clearly not linear. Obviously, the positive correlation does not imply causality, but the result is at least consistent with the flow law used in Stommel's (1961) model. This is, however, not the case for the $R_{0.1}$ POP model. In Fig. 5.5a, it is shown that in PERT the density difference $\Delta\sigma_0$ even increases in time and becomes larger than that of REF. For PERT, a correlation holds between $\Delta\sigma_0$ and the AMOC strength, but it is opposite to that found in the *x*1 version of the model (Fig. 5.5b). A similar conclusion is reached based on the computation of meridional pressure differences as in Griesel and Maqueda (2006, not shown).

5.4.2 The adiabatic pole-to-pole concept

The approach taken in the above provides no information about the importance of transient effects for the relation between surface densities and the evolution of the AMOC. We therefore continue the analysis for the strongly eddying model simulations by relating the results to water mass transformation theory (Walin, 1982; Marsh et al., 2000).

As suggested recently by Wolfe and Cessi (2009, 2011), water mass transformation theory can be used to relate the steady-state strength of the adiabatic, interhemispheric ("pole-
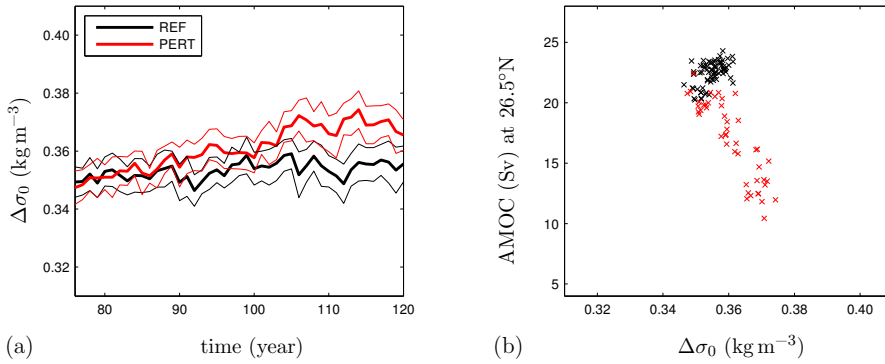
Figure 5.5: Same as Fig. 5.4, but for the $R_{0.1}$ configuration.

to-pole") overturning circulation to the surface density distribution. This is achieved by incorporating the idea that Southern Ocean Ekman transport can maintain a deep overturning circulation in the absence of diapycnal mixing (Toggweiler and Samuels, 1995). The main suggestion is that a pole-to-pole circulation exists, because the following two conditions are met: (1) westerlies are present over the Southern Ocean, which drive a thermally indirect meridional flow and establish a deep stratification; and (2) there is a set of outcropping isopycnals that are shared between the Southern Ocean and the northern North Atlantic, providing a deep, adiabatic pathway for the southward return flow of North Atlantic Deep Water. The theory can be extended by including a diabatic abyssal overturning cell, corresponding to Antarctic Bottom Water (Nikurashin and Vallis, 2011, 2012).

In Wolfe and Cessi (2011) the adiabatic pole-to-pole circulation is analyzed using the isopycnal overturning stream function, which is defined as

$$\psi(\phi, b, t) = -r_0 \cos\phi \int_{\lambda_W}^{\lambda_E} \int_{-H}^{\zeta(\lambda, \phi, b, t)} v(\lambda, \phi, z, t) \, \mathrm{d}z \mathrm{d}\lambda. \qquad (5.2)$$

Here, b represents a buoyancy variable, and $\zeta(\lambda, \phi, b, t)$ is the height of the surface with buoyancy b. In our analysis potential density referenced to 2000 m is used, that is $b = \sigma_2$. In contrast to the evaluation of the depth coordinate stream function Ψ [Eq. (5.1)], monthly-averaged data is not sufficient to construct ψ, due to the time dependence of the upper limit of integration ζ. We therefore restrict the analysis in this subsection to model years 76 and 116 of the PERT simulation (Fig. 5.6a,b), for which daily averaged output is available.

The two conditions for the existence of an adiabatic pole-to-pole circulation put forward by Wolfe and Cessi (2011) relate to water mass transformation in the Southern Ocean and the North Atlantic, respectively. In non-stationary simulations, however, isopycnal transport is not necessarily equal to diapycnal transport (Marsh et al., 2000). In addition to the isopycnal stream function ψ, therefore, one also needs to consider the change in time of

$$V(\phi, b, t) = r_0^2 \int_{\phi}^{90°} \cos\phi' \int_{\lambda_W}^{\lambda_E} \int_{-H}^{\zeta(\lambda, \phi, b, t)} \mathrm{d}z \mathrm{d}\lambda \mathrm{d}\phi', \qquad (5.3)$$
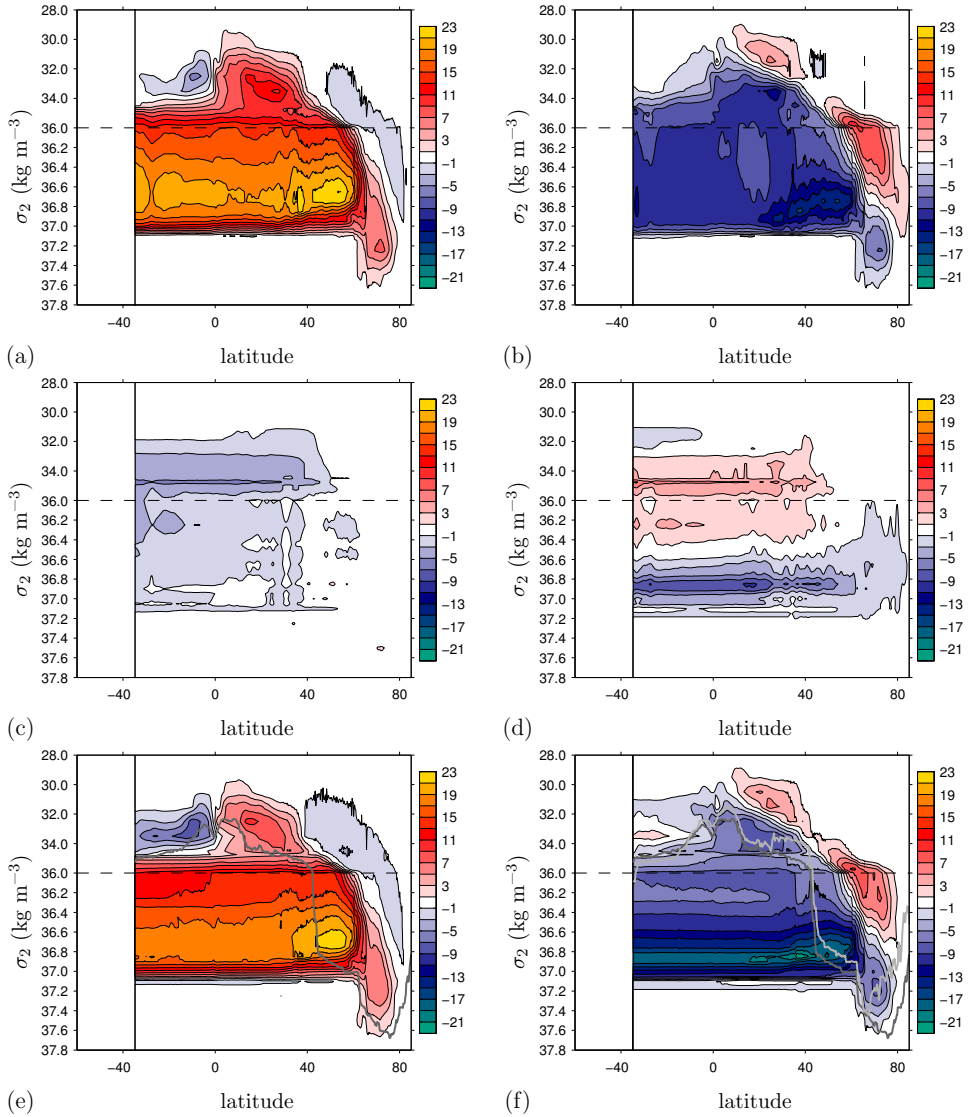
Figure 5.6: Annual mean isopycnal and diapycnal transports in the Atlantic (contour interval 2 Sv) for the $R_{0.1}$ configuration. Panels (a,c,e) show year 76 of PERT and (b,d,f) the difference between year 116 and year 76. Note the change in the vertical scale at $\sigma_2 = 36.0\,\mathrm{kg\,m^{-3}}$. (a,b) Isopycnal stream function ψ. (c,d) Volume tendency $\partial V / \partial t$. (e,f) Transformation stream function G, overlain with the year-round maximum density of the mixed layer in the Atlantic sector, shown in dark grey for year 76 and light grey for year 116 (only in panel f).

the volume north of the section at latitude ϕ and below the surface with buoyancy b (Fig. 5.6c,d). A transformation "pseudo" stream function

$$G(\phi,b,t) = \psi(\phi,b,t) + \frac{\partial V(\phi,b,t)}{\partial t}, \qquad (5.4)$$

can then be defined (Fig. 5.6e,f), which has the useful property that its derivative with respect to latitude, $\partial G/\partial\phi$, gives the correct diapycnal flux of waters at latitude ϕ. Its derivative with respect to b, however, includes both the isopycnal component of the transport and the rate of volume change of waters with buoyancy between b and $b + \delta b$, north of ϕ. In addition, G will not be zero at the southern boundary of a closed basin if changes in V are nonzero; it is hence not a stream function in the non-divergent sense. So, the two stream functions ψ and G are complementary; the first provides the correct isopycnal transport below the surface with buoyancy b, and the second the diapycnal transport north of latitude ϕ.

In year 76 the inflation and deflation of layers only represents a relatively small contribution to the isopycnal flow, especially for potential densities exceeding $36.5\,\mathrm{kg\,m^{-3}}$ (Fig. 5.6c). Hence, the isopycnal (Fig. 5.6a) and transformation (Fig. 5.6e) stream functions are similar, providing a picture of a coherent pole-to-pole circulation, having a maximum of about $23\,\mathrm{Sv}$ at $53°\mathrm{N}$ and $\sigma_2 = 36.7\,\mathrm{kg\,m^{-3}}$. The near vertical contours between $60°\mathrm{N}$ and $65°\mathrm{N}$ reflect the corridor associated with diapycnal transformation and sinking of water to deeper layers in the Labrador Sea. The local maximum at $71°\mathrm{N}$ reflects overturning in the Nordic Seas. The relatively flat contours south and "below" the location of maximum overturning represent southward flow, which is of the same magnitude throughout the Atlantic, indicating that diffusion-driven diapycnal flow is relatively unimportant in the Atlantic basin.

The difference between year 116 and year 76 of the transformation stream function (Fig. 5.6f) indicates that the diapycnal transport north of $53°\mathrm{N}$ weakens by about $18\,\mathrm{Sv}$. This suggests that during the PERT experiment less and less water has access to the adiabatic pathway as a result of less isopycnals being shared between the Southern Ocean and northern North Atlantic, consistent with the reduction of buoyancy loss and ventilation rates over this area (not shown). The changes in convective activity between year 116 and year 76 are also reflected in the decrease of the maximum mixed layer density, shown as the grey lines in Fig. 5.6e,f.

The isopycnal transport is also reduced, weakening by about $15\,\mathrm{Sv}$ at $53°\mathrm{N}$, but only by about $10\,\mathrm{Sv}$ at the southern margin of the Atlantic (Fig. 5.6b). The difference between the change in isopyncal and diapycnal transports indicates a change in the inflation and deflation of layers of equal potential density (Fig. 5.6d), which is not accounted for by the adiabatic pole-to-pole framework (Wolfe and Cessi, 2009, 2011), in which steady-state conditions are assumed. Despite the reduction in distance between levels of equal potential density with $37.2\,\mathrm{kg\,m^{-3}} > \sigma_2 > 36.9\,\mathrm{kg\,m^{-3}}$, there is no change in diffusion driven diapycnal transport in this density range within the duration of the experiment (Fig. 5.6f). On the other hand, the upwelling through the isopycnal surfaces around $\sigma_2 = 36.7\,\mathrm{kg\,m^{-3}}$, occurring in the North Atlantic subtropical gyre, is slightly weakened, which appears compatible with the local inflation of density layers.

It turns out that the net reduction of the transformation of light to dense waters in the Atlantic is *not* accompanied by a reduction of dense to light transformation outside the Atlantic. In Fig. 5.7 we plot the global, South-Pole referenced transformation stream function
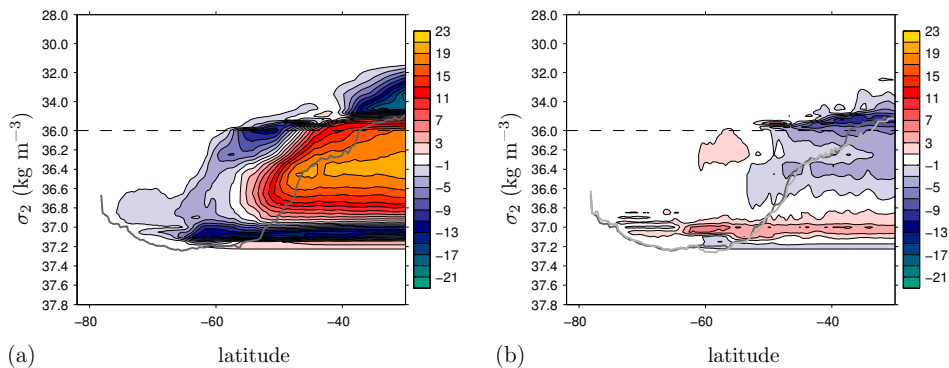
Figure 5.7: Global, South-Pole referenced transformation stream function G' (contour interval 2 Sv), with the results for year 76 of PERT presented in panel (a), and the difference between year 116 and year 76 in panel (b). As discussed in the text, G' shows the transport relative to $\phi = 90°$S. The dark and light grey lines indicate the year-round, global maximum density of the mixed layer in years 76 and 116, respectively.

G', which is defined in a similar way as G [Eq. (5.4)], except that it is zero at $\phi = 90°S$, rather than at $\phi = 90°$N. It shows that in year 76 (Fig. 5.7a) there is an "upwards" cross-isopycnal transport of about 20 Sv (and a "downwards" transport of 4 Sv) through the $\sigma_2 = 36.7 \, \text{kg m}^{-3}$ surface in the region south of where the Atlantic is confined by continents (34°S). In year 116 there is no change in the dense to light transformation through this isopycnal surface (Fig. 5.7b). For latitudes north of 34°S the difference between year 116 and year 76 of the global transformation stream function (not shown) is not significantly different from that calculated for the Atlantic (Fig. 5.6f), indicating that the changes in diapycnal transport in the Pacific are small. In fact, in a globally integrated sense, the reduction of North Atlantic dense water formation causes a decrease of the volume of dense waters, which is accommodated primarily within the Atlantic (Fig. 5.6d), but involving the other basins as well. It thus appears that, over the time scale of the experiments considered here, the concept of the adiabatic pole-to-pole circulation (Wolfe and Cessi, 2009, 2011) is only of limited value in quantitatively relating local changes in buoyancy forcing to (remote) modifications of the basin scale overturning circulation.

5.5 Evolution of the Atlantic salinity budget

In this section, we evaluate the effect of changes in AMOC strength on the basin-wide freshwater transport, which is the second aspect of the salt advection feedback that is discussed in this chapter. Based on a suggestion by Rahmstorf (1996), a framework was developed in subsequent studies (De Vries and Weber, 2005; Dijkstra, 2007; Huisman et al., 2010; Drijfhout et al., 2011), suggesting that the analogy to the box model of Stommel (1961, see Eq.(1.9)) could be drawn by considering the freshwater budget of the combined Atlantic and Arctic basins. We find that, while such an analogy appears relevant for the x1 configuration, the

description is incomplete for the $R_{0.1}$ case.

For POP, the freshwater budget is obtained by multiplying the salinity (S) equation by $-1/S_0$, where $S_0 = 35$ psu is a reference salinity, and integrating the result over the Atlantic and Arctic basins. Written in short, the result is

$$\text{EPR} = Q_t + M + R. \tag{5.5}$$

The left-hand-side of this equation is the total evaporation, minus precipitation and run-off,

$$\text{EPR} = \frac{r_0^2}{S_0} \int \int_A F_S \cos\phi \, d\lambda \, d\phi, \tag{5.6}$$

calculated as the integral of the virtual salt flux F_S (positive for a flux corresponding to evaporation) across the surface of the Atlantic and Arctic (subscript A). The first term on the right-hand-side of Eq. (5.5) represents the change in time of the freshwater content,

$$Q_t = \frac{r_0^2}{S_0} \frac{d}{dt} \int \int_A \left[\int_{-H}^0 S dz + \eta S_1 \right] \cos\phi \, d\lambda \, d\phi, \tag{5.7}$$

where H is the depth of the ocean, S_1 the upper layer salinity, and η the free surface elevation. The second term on the right-hand-side of Eq. (5.5) is net advection of freshwater,

$$M = \frac{-r_0}{S_0} \int \int_{\text{BS}} vS \cos\phi \, dz d\lambda + \frac{-r_0}{S_0} \int \int_{34°S} vS \cos\phi \, dz d\lambda, \tag{5.8}$$

consisting of contributions due to advection across Bering Strait (subscript BS) and the section between South America and South Africa at 34°S, respectively. Parameterized subgrid-scale transports are captured by the last term in Eq. (5.5), which is denoted by R because it is not calculated explicitly, but diagnosed as the residual in the freshwater equation.

For the $x1$ configuration, the mean value of EPR equals 0.37 Sv in REF, and is -0.13 Sv in PERT, as expected. The mean value of Q_t in the REF simulation is about 5×10^{-3} Sv, indicating that the integrated freshwater budget is close to steady state. In the PERT experiment, $Q_t > -0.5$ Sv (not shown), meaning that the overall freshening of the basin is smaller than what is expected solely from the freshwater perturbation. The main reason for this is that M decreases in time (Fig. 5.8a). In REF, the mean value of M is 0.33 Sv, while in PERT its yearly mean values decrease to 0.29 Sv after 45 years and further to 0.23 Sv after 100 years. The implication is that the change in M in the PERT simulation partly offsets the original perturbation. The residual term is relatively small (the mean value of R in REF is 0.03 Sv), and is only modestly affected by the freshwater perturbation (not shown).

In the following, let Δ denote a difference between PERT and REF, such that for a variable X, $\Delta X = X^{\text{PERT}} - X^{\text{REF}}$. Noting that $\Delta M < 0$ arises due to differences between PERT and REF in the velocity and salinity fields at Bering Strait and at the section at 34°S, the question is to what degree ΔM can be attributed to the change in overturning strength at 34°S. In order to analyze this issue, some further notation needs to be introduced. First, let $\hat{f}$ denote a section average of a function $f(\lambda, \phi, z, t)$ at $\phi = 34°S$,

$$\hat{f} = \left(\int_{34°S} dz d\lambda \right)^{-1} \int_{34°S} f \, dz d\lambda. \tag{5.9}$$
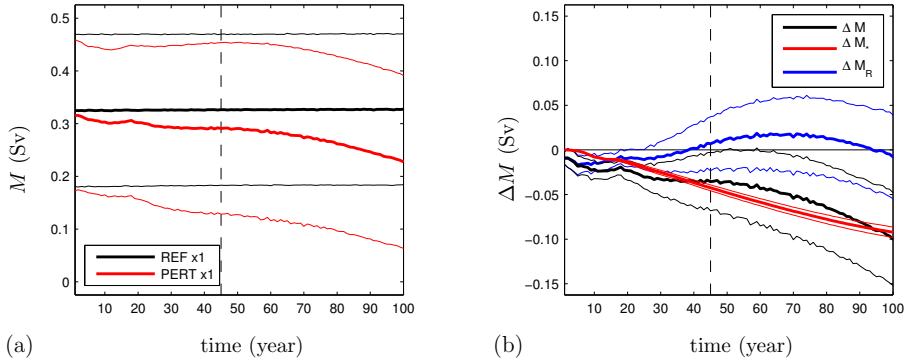
Figure 5.8: (a) Net advective contribution to the freshwater budget M (Eq. 5.8) for the x1 configuration. (b) Shown in black is ΔM, the difference between REF and PERT of net advection of freshwater presented in panel a. This difference is decomposed into a contribution ΔM_* due to the advection of the salinity of REF (S^{REF}) by the difference zonally integrated velocity ($\Delta \Phi_{34°S}$), and a remainder ΔM_R.

Second, we use $\langle f \rangle$ to indicate the zonal mean of f,

$$\langle f \rangle (z) = \left(\int_{\lambda_W}^{\lambda_E} d\lambda \right)^{-1} \int_{\lambda_W}^{\lambda_E} f d\lambda, \tag{5.10}$$

where the integral is evaluated at $\phi = 34°S$. Finally, the divergence-free transport per unit depth is defined as

$$\Phi_{34°S}(z) = r_0 \cos\phi \int_{\lambda_W}^{\lambda_E} \langle v \rangle (z) - \hat{v} \, d\lambda, \tag{5.11}$$

again evaluated at $\phi = 34°S$. Note that the integral over depth of $\Phi_{34°S}$ vanishes, so that $\Phi_{34°S}$ is only associated with net tracer transport if the zonal mean tracer concentration varies with depth. Because the section integrated transport in the Atlantic Ocean is relatively small (about 1 Sv) compared to the AMOC (Ψ) as defined in Eq. (5.1), $\Phi_{34°S}$ is roughly equal to the negative of the vertical derivative of Ψ at 34°S.

We now identify the part of ΔM that is associated with changes in the AMOC strength with

$$\Delta M_* = \int_{-H}^{0} -\Delta \Phi_{34°S}(z) \times \frac{\langle S^{\mathrm{REF}} \rangle (z)}{S_0} \, dz, \tag{5.12}$$

and denote the remainder by $\Delta M_R = \Delta M - \Delta M_*$. Based on this decomposition, it appears that the reduction of M in PERT can to a large degree be attributed to the change in AMOC strength, since the yearly mean values of ΔM_R are relatively small (Fig. 5.8b).

As suggested by Huisman et al. (2010), ΔM_* can be related to a characteristic of the unperturbed reference simulation, because

$$\Delta \Phi_{34°S}(z) \approx -\xi(t) \Phi_{34°S}^{\mathrm{REF}}(z), \tag{5.13}$$

103

with some $\xi(t) > 0$ being a function of time only. This relation also appears to hold true for the experiments described here (not shown). As a result, $\Delta M_* \approx -\xi(t) M_{\text{ov}}^{\text{REF}}$, where

$$M_{\text{ov}} = \frac{-r_0}{S_0} \int_{34°S} (\langle v \rangle - \hat{v}) \langle S \rangle \cos \phi \, \mathrm{d}z \mathrm{d}\lambda \tag{5.14}$$

is the freshwater transport associated with the AMOC. The mean value of M_{ov} in the REF simulation equals 0.14 Sv. The fact that it is positive is hence consistent with ΔM_* being negative. Based on this reasoning, and supported by further numerical model results, it has been suggested that the sign of M_{ov} serves as an indicator of AMOC stability (Rahmstorf, 1996; De Vries and Weber, 2005; Dijkstra, 2007; Huisman et al., 2010; Drijfhout et al., 2011; Hawkins et al., 2011), such that M_{ov} being positive indicates that the salt advection feedback is stabilizing the AMOC, while M_{ov} being negative means that the salt advection feedback is destabilizing the AMOC. Inverse modeling (Weijer et al., 1999) and direct observations (Bryden et al., 2011) suggest that the overturning circulation is exporting freshwater from the Atlantic, i.e. $M_{\text{ov}} < 0$.

We continue by investigating whether the salt advection feedback has a similar signature in the $R_{0.1}$ configuration. In the REF run the net evaporation across the Atlantic and Arctic basins (EPR) is about 0.32 Sv (Fig. 5.9a). As expected, EPR is about 0.5 Sv smaller in the PERT simulation, but it also shows gradual changes in time that can be attributed to the response of evaporation to temperature changes. In contrast to the $x1$ case, the effect of advection on the freshwater balance appears to be similar in both experiments (Fig. 5.9b). Possibly, there is a difference in M between PERT and REF, but is so, it is entirely masked by inter-annual variability. The freshwater tendency Q_t varies around zero in the unperturbed case, but roughly equals -0.5 Sv in the PERT experiment (Fig. 5.9c). For the $R_{0.1}$ configuration, the advective salt fluxes were not saved during run time. Therefore M is calculated from monthly averaged model output, which means that the contribution due to within-month variations of v and S is neglected. The resulting errors are part of the residual R. However, its mean value is small in both REF and PERT (Fig. 5.9d). In addition, the typical variations of R are similar in the two experiments. So, this analysis shows that the extra freshwater input in PERT is totally compensated by storage within the Atlantic and Arctic basins.

To evaluate the significance of the AMOC reduction in PERT for the net advection of freshwater we apply the same decomposition as in the above, $\Delta M = \Delta M_* + \Delta M_R$ (Fig. 5.10a). The variability in ΔM is clearly dominated by the remainder ΔM_R, and it has an amplitude that is significantly stronger than the mean of the AMOC contribution ΔM_*. The latter is of comparable magnitude as in the $x1$ case, but of opposite sign during most of the simulation, despite the fact that the forcing is similar in the two configurations. This means that the effect of the AMOC, if any, is to enhance the original freshwater perturbation. It should be noted that in the upper part of the water column $\langle S^{\text{REF}} \rangle (z)$ is slightly increasing in time. At the surface, its annual mean value increases by about 0.1 psu over the course of the simulation. However, this has hardly any impact on the evolution of ΔM_*; almost the same result is obtained when using the simulation-mean value of $\langle S^{\text{REF}} \rangle (z)$ rather than monthly averages.

According to the theory proposed by Huisman et al. (2010), the fact that ΔM_* is positive during most of the simulation should be reflected in M_{ov} being negative for the REF simulation. However, as illustrated in Fig. 5.10b, a complication arises, because M_{ov} is evolving over the course of the REF simulation. It is positive at the start of the run, but decreases to
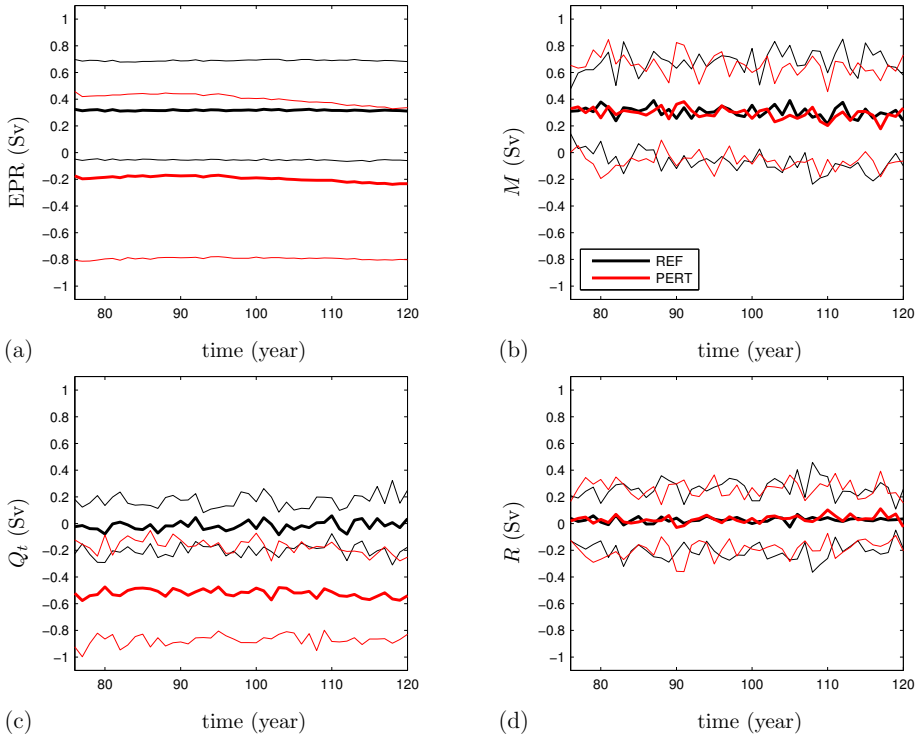
Figure 5.9: Contributions to the freshwater budget expressed by Eq. (5.5) for the $R_{0.1}$ configuration.

values around and below zero. This change occurs despite the absence of a clear trend in the AMOC strength at 34°S (Fig. 5.3b). If, instead of using monthly averages for $\langle S^{\text{REF}} \rangle (z)$, the simulation-mean value of $\langle S^{\text{REF}} \rangle (z)$ is used in the equation for M_{ov} [Eq. (5.14)], the result is almost constant in time and has a mean of 0.023, which is positive rather than negative. Whereas the increase in upper ocean salinities hardly influenced the evolution of ΔM_*, they are the main reason for the decrease of $M_{\text{ov}}^{\text{REF}}$. These results imply that in the $R_{0.1}$ config-uration, $\Delta \Phi_{34°S}(z)$ is not simply proportional to $\Phi_{34°S}^{\text{REF}}(z)$ [Eq. (5.11)]. In other words, the relation expressed by Eq. (5.13), which is an important element of the theory that supports the relevance of M_{ov} as a stability indicator, is not valid in this case.

In the PERT simulation, the change in upper ocean salinities is even stronger than in REF, with surface values of $\langle S^{\text{PERT}} \rangle$ increasing by about 0.2 Sv. This effect is more important than the reduction of the AMOC, which is reflected by ΔM_*, as discussed above. As a result, the reduction of M_{ov} in PERT is stronger than in REF. The conclusion regarding the fact that $\Delta M_{\text{ov}} < 0$ is hence somewhat counterintuitive: whereas the total effect of M_{ov} is to partly offset the original freshwater perturbation, this is due to the change in the zonal mean salinity profile, rather than the result of the reduction of the AMOC.

The impact of the freshwater perturbation is not limited to the overturning component
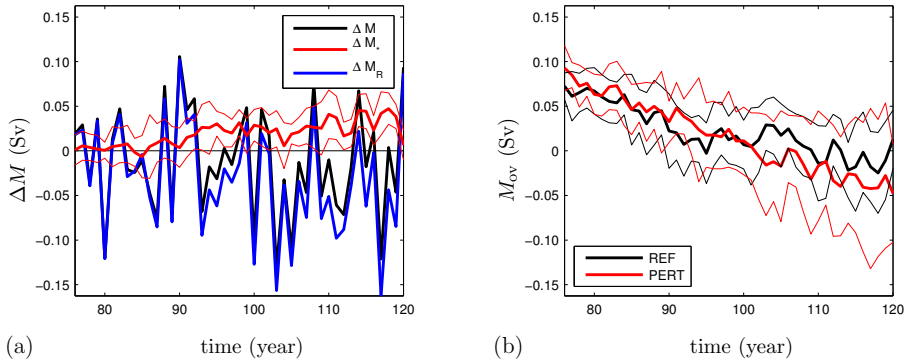
Figure 5.10: (a) Same as Fig. 5.8b, but for the $R_{0.1}$ configuration. For the black and blue lines, the thin lines indicating the 1-year root-mean-square deviation are omitted to avoid overloading the figure. (b) Overturning freshwater transport as in Eq. (5.14).

of the zonally integrated circulation, but also affects the section integrated horizontal transport. Because long term tendencies of area-integrated sea surface height (SSH) are negligible compared to the section integrated transport, its annual mean value is nearly independent of latitude and hence equal to the annual mean transport through Bering Strait (Fig. 5.11). The reduction of the Bering Strait transport in PERT is caused by an increase in SSH in the Arctic (not shown), which leads to a reduction of the pressure gradient across the strait. As in Hu et al. (2012), the changes in the SSH field result from dynamic processes that occur in response to the freshwater perturbation, which by itself does not represent a source of additional volume, as it is implemented as a virtual salt flux. [][t]

The divergence of freshwater advection associated with the section integrated transport is given by (Drijfhout et al., 2011):

$$M_{\Delta BS} = \frac{-r_0}{S_0} \int_{BS} v S \cos \phi \; \mathrm{d}z \mathrm{d}\lambda + \frac{-r_0}{S_0} \int_{34°S} \hat{v} \hat{S} \cos \phi \; \mathrm{d}z \mathrm{d}\lambda. \qquad (5.15)$$

Fig. 5.12a shows that the within-year root-mean-square deviations of $M_{\Delta BS}$ are much stronger than its yearly mean values, so that care must be taken in interpreting the difference between the two simulations. Because short-term changes in the salinity field are small (relative to S_0), the large intra-annual variability is mainly caused by the variations in the Bering Strait transport (Fig. 5.11) and the section-wide transport at 34°S, which are not fully correlated to each other on the time scale of one month. Because an imbalance between the two transports cannot persist indefinitely (a difference of 1 Sv roughly corresponds a sea level change of 1 mm day^{-1} in the Atlantic basin), the inter-annual variability of $M_{\Delta BS}$ is much smaller than the within-year variability. In the REF simulation there appears to be no indication of changes on the time scale of the experiment. The mean value of $M_{\Delta BS}$ in REF is 0.07 Sv, roughly consistent with a mean section integrated transport of 0.96 Sv and a mean salinity contrast between Bering Strait and 34°S of 2.8 psu. In contrast to the results for M_{ov}, the evolution of $M_{\Delta BS}$ is consistent with what is expected from the change of the velocity structure. The long-term reduction of Bering Strait transport (Fig. 5.11) in PERT indeed causes less freshwater
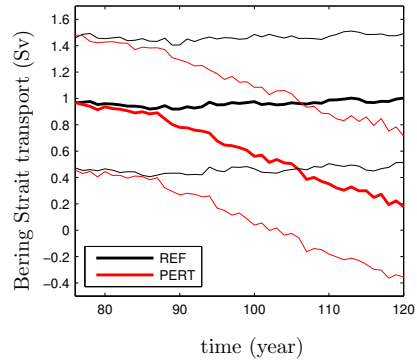
Figure 5.11: Northward transport through Bering Strait for the $R_{0.1}$ configuration.

to be deposited in the Atlantic, although the effect can only be distinguished from the inter-annual variability towards the end of the simulation (Fig. 5.12a). As in the results of Hu et al. (2012), the response of the section-wide transport to the enhanced GrIS melting thus appears to oppose the freshening induced directly by the perturbation.

So far, we have discussed two contributions to the net advection of freshwater, M [Eq. (5.8)]). As detailed in Drijfhout et al. (2011), a third contribution can be defined (denoted by M_{az}), which is related to zonal variations of velocity and salinity that arise from the gyre circulation and eddies, such that

$$M = M_{ov} + M_{\Delta BS} + M_{az}. \tag{5.16}$$

Here, the expressions for the contributions are given, respectively, by Eq. (5.14), Eq. (5.15), and by

$$M_{az} = \frac{-r_0}{S_0} \int_{34°S} v'S' \cos\phi \; dz d\lambda, \tag{5.17}$$

where we used $f' = f - \langle f \rangle$ to denote the deviation from the zonal mean of a function f. The changes of $M_{\Delta BS}$ in PERT and of M_{ov} both in REF and PERT, occurring over the course of the integration, are of comparable magnitude to the typical inter-annual variations of the total advective freshwater convergence M (Fig. 5.9b). Consistent with the finding that M seems to be constant in both experiments, Fig. 5.12b suggests (at least for PERT) that M_{az} is increasing in time to compensate for the decrease of the other two contributions. Compared to the long-term change, however, the inter-annual variability of M_{az} is rather strong. As a consequence, we have been unable to find a satisfactory explanation for this result, which should link the evolution of M_{az} to changes in the zonal structure of the velocity and salinity field at 34°S.

5.6 Summary and discussion

We presented results from two 45-year simulations of the strongly eddying global POP model, one reference simulation (REF) and one simulation in which an extreme integrated freshwater perturbation of 0.5 Sv due to Greenland Ice Sheet melting was prescribed (PERT). We
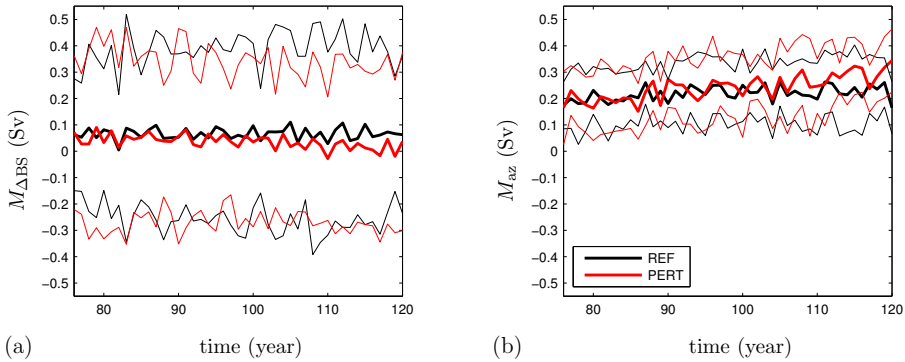
Figure 5.12: Net freshwater advection (a) associated with the section integrated transport [Eq. (5.15)], and (b) due to zonal variations of velocity and salinity [Eq. 5.17].

compared these to results from a corresponding set of simulations with POP configured at low horizontal resolution. Our objective was to evaluate whether the strong reduction of the basin-wide circulation that is induced by the perturbation, is governed by similar large-scale nonlinear processes in the two configurations of the model. Due to the large amplitude of the freshwater perturbation, the simulations should not be considered as a realistic scenario for present-day climate change, for which an 0.1 Sv perturbation would already be seen as catastrophic. However, 0.5 Sv may be considered as an upper bound of the total freshwater input associated with a typical Heinrich event during the last glacial period (Roche et al., 2004).

In particular, we focussed on the salt advection feedback, which is thought to be responsible for a strong sensitivity of the ocean to freshwater forcing and may lead to abrupt transitions due to the existence of multiple steady states (Bryan, 1986; Rahmstorf, 1996, 2000). One of the simplest representations of the salt advection feedback is provided by the two-box model of Stommel (1961), which suggests that the following three conditions are important for the feedback to operate: (1) the large-scale flow is proportional to a meridional density gradient; (2) the large-scale flow carries heat and freshwater, affecting that density gradient; and (3) the boundary conditions are such that temperature anomalies are damped out much quicker than salinity anomalies, so that the flow has a stronger control over the salinity gradient than over the temperature gradient. We framed the presentation of the results around the first two of these conditions.

Although counterexamples have been provided (De Boer et al., 2010), there are several results from coarse-resolution models that indicate that the strength of the AMOC is proportional to the North-South difference in density (Rahmstorf, 1996; Dijkstra, 2008) or pressure (Griesel and Maqueda, 2006). In agreement with these studies and condition (1), a positive correlation between yearly mean values of the AMOC strength and the potential density contrast ($\Delta\sigma_0$) was established for the $x1$ configuration. However, in the $R_{0.1}$ version of the model, the correlation was found to be of opposite sign. Therefore, we further analyzed the $R_{0.1}$ results, starting from the adiabatic pole-to-pole concept (Wolfe and Cessi, 2009, 2011). According to this theory, the steady-state strength of the (adiabatic part of the) large-scale overturning is determined by the degree of overlap in the density range that is ventilated in

the Southern Ocean and in the northern North Atlantic. In the PERT experiment the density range with outcropping isopycnals is reduced in the North Atlantic, both directly due to the enhanced runoff from Greenland, but also as a result of the shallowing of the mixed layer and the associated weakening of buoyancy loss in the Labrador Sea. As a result, the rate of light to dense transformation is strongly reduced in the region around 60°N (Fig. 5.6f). However, the local change in diapycnal transport does not correspond quantitatively to the change in isopycnal flow at other latitudes in the Atlantic (Fig. 5.6b). This is explained by the fact that, over the time scale of the experiment, no compensating reduction in dense to light transformation is established elsewhere in ocean. As a result, the amount of dense water is continuously decreasing, both inside and outside the Atlantic. Although eventually a new quasi-equilibrium could be reached under sustained freshwater forcing, none of the results presented show a sign of leveling off at the end of the 45-year integration.

Through comparison of the x1 and the $R_{0.1}$ simulations, we found that the changes in the basin-wide circulation lead to a very different response in net advective freshwater convergence in the Atlantic basin. In the $x1$ configuration, the results appeared to be consistent with condition (2), as illustrated in Fig. 5.8. In addition, they supported the relevance of M_{ov} as an indicator of the stability of the AMOC (Rahmstorf, 1996; Huisman et al., 2010). In the strongly eddying model, however, the effect of the AMOC on the freshwater budget was found to be small compared to typical inter-annual variations in the total net advection of freshwater (Figs. 5.9 and 5.10). Furthermore, the effect appeared inconsistent with the sign of the stability indicator M_{ov}. In addition to M_{ov}, the net freshwater advection is determined by the contribution associated with the section integrated transport ($M_{\Delta BS}$), and that due to zonal variations in salinity and velocity (M_{az}), but we were unable to establish a functional relationship between these contributions and the freshwater perturbation.

In the simulations described here and in Weijer et al. (2012) sea surface salinity is not restored to climatology, allowing the circulation to have a stronger impact on salinity than on temperature. The sea surface temperature (SST) field is not fixed, though. This means that, since bulk formulae are used to calculate evaporation, the surface freshwater flux may respond to changes in the circulation. This effect is indeed observed in the $R_{0.1}$ PERT experiment (Fig. 5.9a). Results from another coarse-resolution model suggest that atmospheric feedbacks modify the sensitivity of the circulation to freshwater perturbations only quantitatively (Den Toom et al., 2012). If, however, the basin scale salt advection feedback is insignificant in eddying models, feedbacks operating through atmospheric processes could be relatively important for the behavior of the coupled ocean-atmosphere system. It may therefore be necessary to incorporate a dynamical atmosphere to accurately assess climate system response to a strong freshwater anomaly from Greenland. Similarly, the incorporation of a dynamical ice model might lead to qualitatively different results than presented here.

What is clear at this point is that the AMOC response in strongly eddying models is quite different to that of models in which the effect of eddies is parameterized. This may have far reaching consequences regarding the existence of a multiple equilibria regime of the AMOC (Rahmstorf, 1996), the value of stability indicators based on the Atlantic freshwater budget (De Vries and Weber, 2005; Huisman et al., 2010; Drijfhout et al., 2011) and the theories of rapid climate transitions in the past (Alley et al., 2003).

6

Conclusions and outlook

The principal aim of this thesis is to advance our understanding of the large-scale ocean circulation. Because it is an important factor in determining (local) climate, detailed knowledge of its characteristics is needed for making reliable predictions of the future climate. Observations provide a picture of the typical pattern and variability in strength of the zonally integrated flow in each basin. However, field data are too scarce to conclude which processes are essential for the dynamics of the MOC. Therefore, a systematic analysis of numerical ocean-climate models is indispensable.

The ocean is expected to feature nonlinear behavior due to the interaction between the density distribution and the velocity field. Characteristic expressions of this interaction are a nonlinear dependence of the MOC on the vertical diffusion coefficient (Welander, 1971; Park and Bryan, 2000), and the enhanced sensitivity to changes in the surface freshwater flux as result of the salt-advection feedback (Stommel, 1961; Bryan, 1986). The main question is to what degree the behavior of the global ocean circulation is determined by these mechanisms. In order to eventually answer this question, it is necessary to test numerical model results for robustness to different representations of unresolved processes.

In chapter 2 we investigated a rather idealized model, in which the salt-advection feedback was disabled. Based on the notion that Southern Ocean wind stress may drive a global overturning circulation in absence of diapycnal mixing (Toggweiler and Samuels, 1995, 1998), it is tempting to assume that the overturning strength is to first order a linear function of wind stress, while the nonlinear effects due to the vertical advection-diffusion balance are only of secondary importance. Our results suggest, however, that the advection-diffusion balance is valid in both the Atlantic and Pacific basins, especially for the smallest values of the diffusivity, and independent of the presence of wind. The effect of wind was found to be important, but mainly for setting the depth of the pycnocline. A natural extension of this work would be to evaluate the sensitivity to vertical diffusivity in a model with mixed boundary conditions

for temperature and salinity. The results in chapter 2 also showed that the use of horizontal mixing of tracers instead of the more physically based parameterization of Redi (1982) and Gent and McWilliams (1990) may lead to the incorrect result that the scaling of the Atlantic and Pacific MOC is different (Dijkstra, 2008). This finding motivates to further investigate why the current version of THCM (THCM-B; De Niet et al., 2007) cannot be used efficiently with a more advanced scheme than horizontal mixing. Similar to the approach in chapter 4, it may be useful to define a low-order model for lateral mixing and investigate its behavior using numerical continuation techniques.

The research in chapter 3 was devoted to the peculiar behavior of the Convective Adjustment (CA) scheme, which is commonly used in ocean models to eliminate static instabilities. It has been claimed that convective dynamics may result in the presence of multiple equilibria (Welander, 1982), which are mainly thought to differ from each other in the local pattern of convection (Lenderink and Haarsma, 1994; Rahmstorf, 1995), although a global imprint has also been suggested (Hofmann and Rahmstorf, 2009). The results in this chapter do not rule out the possibility of a convective feedback. It is clear, however, that CA cannot be used to adequately represent such mechanism, as the scheme suffers from a serious numerical artifact that causes the number of multiple equilibria to depend on the vertical resolution. As long as no numerically sound, physically based alternative to CA is available, this issue prevents the use of THCM-B for studying the sensitivity of the ocean to freshwater in a global model configuration.

Multiple steady states due to the salt-advection feedback have been found in many ocean-climate models (Rahmstorf et al., 2005), but not yet in state-of-the-art global climate models such as used in the fourth assessment report (AR4) of the IPCC (Meehl et al., 2007). This is often thought to indicate that multiple equilibria are an artifact of the simpler models, an idea that is supported by the suggestion that atmospheric feedbacks effectively oppose the salt-advection feedback (Yin et al., 2006). However, the results in chapter 4 indicate that atmospheric feedbacks are too weak to remove the multiple equilibria regime. The use of the techniques from bifurcation analysis turned out to be very useful in this study, as it allowed to explicitly link the shift of one of the bifurcation points to the patterns of the forcing. Nonetheless, it should be noted here that the model that was used, THCM-C (Weijer et al., 2003), has several deficiencies as a result of which possible feedbacks acting through the wind field could not be taken into account properly. It may be valuable in this case to pursue conventional time-stepping methods for detecting multiple equilibria in hybrid, coupled ocean-atmosphere models that are not affected by these deficiencies. Given the fact that hybrid coupled models are very efficient (Cimatoribus et al., 2012), such approach should be feasible.

Observations indicate that the MOC is in fact a highly variable residual circulation of a strongly eddying fluid (Cunningham et al., 2007), rather than a relatively steady, coherent feature as in coarse resolution ocean-climate models. In a first attempt to address the importance of eddies for the sensitivity of the MOC to freshwater perturbations, Weijer et al. (2012) found that the eddy-resolving version of POP (Dukowicz and Smith, 1994) is more sensitive to enhanced runoff from Greenland than its coarse resolution counterpart. The results from the follow-up study presented in chapter 5 appear to indicate, however, that the salt-advection feedback is less important for the dynamics of the MOC in the eddying model than in lower resolution models. This rather counterintuitive finding requires further explo-

ration. It is possible that the diagnostic framework used in chapter 5 (Drijfhout et al., 2011) is not appropriate for use in strongly eddying models. Or maybe the salt-advection feedback is only significant over time scales longer than considered here. Or perhaps the salt-advection feedback only plays a local role. Due to the large computational cost involved in running eddy-resolving models, it may be advantageous to move to a smaller domain with a simple geometry (Wolfe and Cessi, 2009) to investigate these suggestions.

It appears attractive to think of the climate as a largely linear system, as witnessed for example by the popularity of the concept of *climate sensitivity* (Knutti and Hegerl, 2008), which is a number that expresses the equilibrium change in global air temperature as a result of doubling the carbon dioxide concentration. The notion of a linear climate seems to be supported by the absence of abrupt transitions in the projections of IPCC-AR4 (Meehl et al., 2007). Admittedly, it is not fully clear how the non-linear dynamics of the ocean are reflected in its behavior. However, based on our current knowledge of the dynamics of the ocean, the idea of a linear climate cannot be maintained. Provided that a systematic approach is followed, many of the open issues regarding the importance of nonlinear feedbacks for the large-scale circulation may be eventually solved as computational resources increase and more observations become available.

Bibliography

Alley, R. B., Marotzke, J., Nordhaus, W. D., Overpeck, J. T., Peteet, D. M., Pielke Jr., R. A., Pierre-humbert, R. T., Rhines, P. B., Stocker, T. F., Talley, L. D., and Wallace, J. M. (2003). Abrupt Climate Change. *Science*, 299:2005–2010.

Andersson, A., Fennig, K., Klepp, C., Bakan, S., Graßl, H., and Schulz, J. (2010). The Hamburg Ocean Atmosphere Parameters and Fluxes from Satellite Data – HOAPS-3. *Earth Syst. Sci. Data Discuss.*, 3(1):143–194.

Arzel, O., England, M. H., and Saenko, O. A. (2011). The impact of wind stress feedback on the stability of the atlantic meridional overturning circulation. *J. Climate*, 24(7):1965–1984.

Bernsen, E., Dijkstra, H. A., and Wubs, F. W. (2008). A method to reduce the spin-up time of ocean models. *Ocean Model.*, 20(4):380–392.

Bower, A. S., Lozier, M. S., Gary, S. F., and Boning, C. W. (2009). Interior pathways of the North Atlantic meridional overturning circulation. *Nature*, 459(7244):243–247.

Bryan, F. (1987). Parameter sensitivity of primitive equation ocean general circulation models. *J. Phys. Oceanogr.*, 17:970–985.

Bryan, F. O. (1986). High-latitude salinity effects and interhemispheric thermohaline circulations. *Nature*, 323:301–304.

Bryan, K. and Cox, M. (1967). A numerical investigation of the oceanic general circulation. *Tellus*, 19:54–80.

Bryden, H. L., King, B. A., and McCarthy, G. D. (2011). South Atlantic overturning circulation at 24°S. *J. Mar. Res.*, 69(1):38–55.

Cessi, P. (1996). Grid-scale instability of convective-adjustment schemes. *J. Mar. Res.*, 54:407–420.

Cessi, P. and Young, W. R. (1992). Multiple equilibria in two-dimensional thermohaline circulation. *J. Fluid. Mech.*, 241:291–309.

Cessi, P. and Young, W. R. (1996). Some unexpected consequences of the interaction between convective adjustment and horizontal diffusion. *Physica D*, 98(2-4):287–300.

Chang, P., Ji, L., and Li, H. (1997). A decadal climate variation in the tropical atlantic ocean from thermodynamic air-sea interactions. *Nature*, 385(6616):516–518.

Cimatoribus, A., Drijfhout, S., and Dijkstra, H. (2012). A global hybrid coupled model based on atmosphere-sst feedbacks. *Clim. Dynam.*, 38(3):745–760.

Clark, P. U., Pisias, N. G., Stocker, T. F., and Weaver, A. J. (2002). The role of the thermohaline circulation in abrupt climate change. *Nature*, 415(6874):863–869.

Colin de Verdière, A. (1988). Buoyancy driven planetary flows. *J. Mar. Res.*, 46:215–265.

Colin de Verdière, A., Ben Jelloul, M., and Sévellec, F. (2006). Bifurcation Structure of Thermohaline Millennial Oscillations. *J. Climate*, 19(22):5777–5795.

Cunningham, S. A., Kanzow, T., Rayner, D., Baringer, M. O., Johns, W. E., Marotzke, J., Longworth, H. R., Grant, E. M., Hirschi, J. J.-M., Beal, L. M., Meinen, C. S., and Bryden, H. L. (2007). Temporal Variability of the Atlantic Meridional Overturning Circulation at 26.5°N. *Science*, 317(5840):935–938.

Dalan, F., Stone, P. H., Kamenkovich, I. V., and Scott, J. R. (2005). Sensitivity of the ocean's climate to diapycnal diffusivity in an EMIC. Part I: equilibrium state. *J. Climate*, 18:2460–2481.

Danabasoglu, G., McWilliams, J. C., and Gent, P. R. (1994). The role of mesoscale tracer transports in the global ocean circulation. *Science*, 264:1123–1126.

De Boer, A. M., Gnanadesikan, A., Edwards, N. R., and Watson, A. J. (2010). Meridional Density Gradients Do Not Control the Atlantic Overturning Circulation. *J. Phys. Oceanogr.*, 40(2):368–380.

De Niet, A., Wubs, F., Van Scheltinga Terwisscha, A., and Dijkstra, H. A. (2007). A tailored solver for bifurcation analysis of ocean-climate models. *J. Comput. Phys.*, 227(1):654–679.

De Vries, P. and Weber, S. L. (2005). The Atlantic freshwater budget as a diagnostic for the existence of a stable shut down of the meridional overturning circulation. *Geophys. Res. Lett.*, 32(9):L09606.

Den Toom, M., Dijkstra, H. A., Cimatoribus, A. A., and Drijfhout, S. S. (2012). Effect of Atmospheric Feedbacks on the Stability of the Atlantic Meridional Overturning Circulation. *J. Climate*, 25(12):4081–4096.

Den Toom, M., Wubs, F. W., and Dijkstra, H. A. (2009). Corrigendum to "A tailored solver for bifurcation analysis of ocean-climate models"[J. Comput. Phys. 227 (2007) 654–679]. *J. Comput. Phys.*, 228(13):4962–4964.

Dijkstra, H., Frankcombe, L., and von der Heydt, A. (2008). A stochastic dynamical systems view of the Atlantic Multidecadal Oscillation. *Philos. T. R. Soc. Lond.*, 366(1875):2543–2558.

Dijkstra, H. A. (2005). *Nonlinear Physical Oceanography*, chapter 6, pages 267–368. Springer.

Dijkstra, H. A. (2006). The ENSO phenomenon: theory and mechanisms. *Adv. Geosci.*, 6:3–15.

Dijkstra, H. A. (2007). Characterization of the multiple equilibria regime in a global ocean model. *Tellus A*, 59(5):695–705.

Dijkstra, H. A. (2008). Scaling of the Atlantic meridional overturning circulation in a global ocean model. *Tellus A*, 60:749–760.

Dijkstra, H. A. and Ghil, M. (2005). Low-frequency variability of the large-scale ocean circulation: A dynamical systems approach. *Rev. Geophys.*, 43(3):RG3002.

Dijkstra, H. A., Te Raa, L., and Weijer, W. (2004). A systematic approach to determine thresholds of the ocean's thermohaline circulation. *Tellus A*, 56(4):362–370.

Dijkstra, H. A. and Weijer, W. (2005). Stability of the global ocean circulation: Basic bifurcation diagrams. *J. Phys. Oceanogr.*, 35(6):933–948.

Dixon, K. W., Delworth, T. L., Spelman, M. J., and Stouffer, R. J. (1999). The influence of transient surface fluxes on north atlantic overturning in a coupled gcm climate change experiment. *Geophys. Res. Lett.*, 26(17):2749–2752.

Drijfhout, S., Weber, S., and van der Swaluw, E. (2011). The stability of the MOC as diagnosed from model projections for pre-industrial, present and future climates. *Clim. Dynam.*, 37:1575–1586.

Drijfhout, S. S., Maier-Reimer, E., and Mikolajewicz, U. (1996). Tracing the conveyor belt in the Hamburg large-scale geostrophic ocean general circulation model. *J. Geophys. Res.*, 101(C10):22563–22575.

Dukowicz, J. K. and Smith, R. D. (1994). Implicit free-surface method for the Bryan-Cox-Semtner ocean model. *J. Geophys. Res.*, 99(C4):7991–8014.

Enfield, D. B., Mestas-Nuñez, A. M., and Trimble, P. J. (2001). The Atlantic Multidecadal Oscillation and its relation to rainfall and river flows in the continental U.S. *Geophys. Res. Lett.*, 28:2077–2080.

Fekete, B. M., Vörösmarty, C. J., and Grabs, W. (2000). Global, composite runoff fields based on observed river and simulated water balances. Technical report, Global Runoff Data Centre.

Flament, P. (2002). A state variable for characterizing water masses and their diffusive stability: spiciness. *Prog. Oceanogr.*, 54(1-4):493–501.

Ganachaud, A. and Wunsch, C. (2000). Improved estimates of global ocean circulation, heat transport and mixing from hydrographic data. *Nature*, 408(6811):453–457.

Ganopolski, A. and Rahmstorf, S. (2001). Rapid changes of glacial climate simulated in a coupled climate model. *Nature*, 409(6817):153–158.

Gent, P. R. and McWilliams, J. C. (1990). Isopycnal mixing in ocean circulation models. *J. Phys. Oceanogr.*, 20:150–155.

Gerdes, R., Hurlin, W., and Griffies, S. (2006). Sensitivity of a global ocean model to increased run-off from Greenland. *Ocean Model.*, 12(3-4):416–435.

Gerdes, R., Koberle, C., and Willebrand, J. (1991). The influence of numerical advection schemes on the results of ocean general circulation models. *Clim. Dynam.*, 5:211226.

Gnanadesikan, A. (1999). A simple predictive model for the structure of the oceanic pycnocline. *Science*, 283:2077–2079.

Goosse, H. and Fichefet, T. (1999). Importance of ice-ocean interactions for the global ocean circulation: A model study. *J. Geophys. Res.*, 104(C10):23337–23355.

Gordon, A. L. (1986). Inter-ocean exchange of thermocline water. *J. Geophys. Res.*, 91:5037–5046.

Griesel, A. and Maqueda, M. (2006). The relation of meridional pressure gradients to North Atlantic deep water volume transport in an ocean general circulation model. *Clim. Dynam.*, 26:781–799.

Hasselmann, K. (1976). Stochastic climate models Part I. Theory. *Tellus*, 28(6):473–485.

Hawkins, E., Smith, R. S., Allison, L. C., Gregory, J. M., Woollings, T. J., Pohlmann, H., and de Cuevas, B. (2011). Bistability of the Atlantic overturning circulation in a global climate model and links to ocean freshwater transport. *Geophys. Res. Lett.*, 38(10).

Hofmann, M. and Rahmstorf, S. (2009). On the stability of the Atlantic meridional overturning circulation. *P. Natl. Acad. Sci. USA*, 106:20584–20589.

Hu, A., Meehl, G. A., Han, W., Timmermann, A., Otto-Bliesner, B., Liu, Z., Washington, W. M., Large, W., Abe-Ouchi, A., Kimoto, M., Lambeck, K., and Wu, B. (2012). Role of the Bering Strait on the hysteresis of the ocean conveyor belt circulation and glacial climate stability. *P. Natl. Acad. Sci.*

USA, 109(17):6417–6422.

Hu, A., Meehl, G. A., Han, W., and Yin, J. (2009). Transient response of the MOC and climate to potential melting of the Greenland Ice Sheet in the 21st century. *Geophys. Res. Lett.*, 36(10):L10707.

Hu, D. (1996). On the sensitivity of thermocline depth and meridional heat transport to vertical diffusivity in OGCMs. *J. Phys. Oceanogr.*, 26:1480–1494.

Hughes, G. O., Hogg, A. M. C., and Griffiths, R. W. (2009). Available potential energy and irreversible mixing in the meridional overturning circulation. *J. Phys. Oceanogr.*, 39(12):3130–3146.

Huisman, S. E., den Toom, M., Dijkstra, H. A., and Drijfhout, S. (2010). An Indicator of the Multiple Equilibria Regime of the Atlantic Meridional Overturning Circulation. *J. Phys. Oceanogr.*, 40(3):551–567.

Hurrell, J. W., Hack, J. J., Shea, D., Caron, J. M., and Rosinski, J. (2008). A New Sea Surface Temperature and Sea Ice Boundary Dataset for the Community Atmosphere Model. *J. Climate*, 21(19):5145–5153.

Jones, H. J. and Marshall, J. (1993). Convection with rotatation in a neutral ocean: a study of open ocean deep convection. *J. Phys. Oceanogr.*, 23:1009–1039.

Jungclaus, J. H., Haak, H., Esch, M., Roeckner, E., and Marotzke, J. (2006). Will Greenland melting halt the thermohaline circulation? *Geophys. Res. Lett.*, 33(17):L17708.

Kanzow, T., Cunningham, S. A., Rayner, D., Hirschi, J. J.-M., Johns, W. E., Baringer, M. O., Bryden, H. L., Beal, L. M., Meinen, C. S., and Marotzke, J. (2007). Observed Flow Compensation Associated with the MOC at 26.5°N in the Atlantic. *Science*, 317(5840):938–941.

Keller, H. B. (1977). Numerical solution of bifurcation and nonlinear eigenvalue problems. In Rabinowitz, P. H., editor, *Applications of Bifurcation Theory*, pages 359–384. Academic Press, New York, U.S.A.

Klinger, B. A., Drijfhout, S., Marotzke, J., and Scott, J. R. (2003). Sensitivity of basinwide meridional overturning to diapycnal diffusion and remote wind forcing in an idealized atlantic-southern ocean geometry. *J. Phys. Oceanogr.*, 33:249–266.

Knutti, R. and Hegerl, G. C. (2008). The equilibrium sensitivity of the Earth's temperature to radiation changes. *Nature Geosci*, 1(11):735–743.

Knutti, R., Stocker, T. F., and Wright, D. G. (2000). The effects of subgrid-scale parameterizations in a zonally averaged ocean model. *J. Phys. Oceanogr.*, 30(11):2738–2752.

Kuhlbrodt, T., Griesel, A., Montoya, M., Levermann, A., Hofmann, M., and Rahmstorf, S. (2007). On the driving processes of the Atlantic meridional overturning circulation. *Rev. Geophys.*, 45:RG2001.

Large, W. G. and Yeager, S. (2004). Diurnal to decadal global forcing for ocean and sea-ice models: the data sets and flux climatologies. Technical report, National Center for Atmospheric Research, Boulder, CO, U.S.A.

Latif, M., Roeckner, E., Mikolajewicz, U., and Voss, R. (2000). Tropical stabilization of the thermohaline circulation in a greenhouse warming simulation. *J. Climate*, 13(11):1809–1813.

Lazar, A., Madec, G., and Delecluse, P. (1999). The deep interior downwelling, the Veronis effect, and mesoscale tracer transport parameterizations in an OGCM. *J. Phys. Oceanogr.*, 29:2945–2961.

Ledwell, J. R., Watson, A. J., and Law, C. S. (1993). Evidence for slow mixing across the pycnocline

from an open-ocean tracer-release experiment. *Nature*, 364:701–703.

Lenderink, G. and Haarsma, H. (1994). Variability and multiple equilibria of the thermohaline circulation associated with deep-water formation. *J. Phys. Oceanogr.*, 24:1480–1493.

Levitus, S., R., B., and T., B. (1994). *World Ocean Atlas 1994*, volume 3: Salinity of *NOAA Atlas NESDIS*. US Department of Commerce, Washington DC, USA.

Lineikin, P. (1955). On the determination of the thickness of the baroclinic layer in the sea. *Dokl. Akad. Nauk USSR*, 101:461–464.

Lumpkin, R. and Speer, K. (2007). Global Ocean Meridional Overturning. *J. Phys. Oceanogr.*, 37(10):2550–2562.

Maltrud, M., Bryan, F., and Peacock, S. (2010). Boundary impulse response functions in a century-long eddying global ocean simulation. *Environ. Fluid. Mech.*, 10(1–2):275–295.

Marotzke, J. (1990). *Instabilities and multiple equilibria of the thermohaline circulation*. PhD thesis, Inst. Meeresk. Kiel.

Marotzke, J. (1991). Influence of convective adjustment on the stability of the thermohaline circulation. *J. Phys. Oceanogr.*, 21(6):903–907.

Marotzke, J. (1997). Boundary mixing and the dynamics of three-dimensional thermohaline circulations. *J. Phys. Oceanogr.*, 27:1713–1728.

Marotzke, J. and Scott, J. R. (1999). Convective mixing and the thermohaline circulation. *J. Phys. Oceanogr.*, 29(11):2962–2970.

Marotzke, J. and Willebrand, J. (1991). Multiple equilibria of the global thermohaline circulation. *J. Phys. Oceanogr.*, 21(9):1372–1385.

Marsh, R., Desbruyeres, D., Bamber, J. L., de Cuevas, B. A., Coward, A. C., and Aksenov, Y. (2010). Short-term impacts of enhanced Greenland freshwater fluxes in an eddy-permitting ocean model. *Ocean Sci.*, 6(3):749–760.

Marsh, R., Nurser, A., Megann, A., and New, A. (2000). Water mass transformation in the Southern Ocean of a global isopycnal coordinate GCM. *J. Phys. Oceanogr.*, 30(5):1013–1045.

Meehl, G. A., Stocker, T. F., Collins, W. D., Friedlingstein, P., Gaye, A. T., Gregory, J. M., Kitoh, A., Knutti, R., Murphy, J. M., Noda, A., Raper, S. C. B., Watterson, I. G., J., W. A., and Zhao, Z.-C. (2007). Global climate projections. In *Climate Change 2007: The Physical Science Basis. Contribution of Working Group I to the Fourth Assessment Report of the Intergovernmental Panel on Climate Change [Solomon, S., D. Qin, M. Manning, Z. Chen, M. Marquis, K.B. Averyt, M. Tignor and H.L. Miller (eds.)]*. Cambridge University Press, Cambridge, United Kingdom and New York, NY, USA.

Mernild, S. H., Liston, G. E., Hiemstra, C. A., and Christensen, J. H. (2010). Greenland Ice Sheet Surface Mass-Balance Modeling in a 131-Yr Perspective, 1950–2080. *J. Hydrometeorol.*, 11(1):3–25.

Munk, W. (1966). Abyssal recipes. *Deep-Sea Res.*, 13:707–730.

Munk, W. and Wunsch, C. (1998). Abyssal recipes II: Energetics of tidal and wind mixing. *Deep-Sea Res. (1 Oceanogr. Res. Pap.)*, 45:1977–2010.

Murray, R. J. (1996). Explicit generation of orthogonal grids for ocean models. *J. Comput. Phys.*,

126:251–273.

Nikurashin, M. and Vallis, G. (2011). A Theory of Deep Stratification and Overturning Circulation in the Ocean. *J. Phys. Oceanogr.*, 41(3):485–502.

Nikurashin, M. and Vallis, G. (2012). A Theory of the Interhemispheric Meridional Overturning Circulation and Associated Stratification. *J. Phys. Oceanogr.* in press.

Pacanowski, R. and Griffies, S. (2000). MOM 3.0 Manual. Technical report, Geophysical Fluid Dynamics Laboratory/NOAA. Available online at http:www.gfdl.noaa.gov.

Park, Y. and Bryan, K. (2000). Comparison of thermally driven circulations from a depth-coordinate model and an isopycnal-layer model. Part I: Scaling-law sensitivity to vertical diffusivity. *J. Phys. Oceanogr.*, 30:590–605.

Philander, S. G. H. (1990). *El Niño, La Niña and the Southern Oscillation*. Academic Press. 289pp.

Polzin, K. L., Toole, J. M., Ledwell, J. R., and Schmitt, R. W. (1997). Spatial variability of turbulent mixing in the abyssal ocean. *Science*, 276:93–96.

Rahmstorf, S. (1995). Multiple convection patterns and thermohaline flow in an idealized ogcm. *J. Climate*, 8:3028–3039.

Rahmstorf, S. (1996). On the freshwater forcing and transport of the Atlantic thermohaline circulation. *Clim. Dynam.*, 12(12):799–811.

Rahmstorf, S. (1999). Rapid transitions of the thermohaline ocean circulation - a modelling perspective. In Abrantes, F. and Mix, A. C., editors, *Reconstructing ocean history: a window into the future*, pages 139–149. Kluwer Academic/Plenum Publisher.

Rahmstorf, S. (2000). The thermohaline circulation: a system with dangerous thresholds? *Climatic Change*, 46:247–256.

Rahmstorf, S., Crucifix, M., Ganopolski, A., Goosse, H., Kamenkovich, I., Knutti, R., Lohmann, G., Marsh, R., Mysak, L. A., Wang, Z., and Weaver, A. J. (2005). Thermohaline circulation hysteresis: A model intercomparison. *Geophys. Res. Lett.*, 32(23).

Redi, M. H. (1982). Oceanic isopycnal mixing by coordinate rotation. *J. Phys. Oceanogr.*, 12:1154–1158.

Rignot, E. and Kanagaratnam, P. (2006). Changes in the Velocity Structure of the Greenland Ice Sheet. *Science*, 311(5763):986–990.

Rignot, E., Velicogna, I., van den Broeke, M., Monaghan, A., and Lenaerts, J. (2011). Acceleration of the contribution of the Greenland and Antarctic ice sheets to sea level rise. *Geophys. Res. Lett.*, 38.

Robinson, A. and Stommel, H. (1959). The oceanic thermocline and the associated thermohaline circulation. *Tellus*, 11:295–308.

Roche, D., Paillard, D., and Cortijo, E. (2004). Constraints on the duration and freshwater release of Heinrich event 4 through isotope modelling. *Nature*, 432(7015):379–382.

Saad, Y. (1996). *Iterative Methods for Sparse Matrices*. PWS Publishing Co., Boston. 184pp.

Schmidt, G. A. and Mysak, L. A. (1996). The stability of a zonally averaged thermohaline circulation model. *Tellus A*, 48:158–178.

Schmittner, A., Latif, M., and Schneider, B. (2005). Model projections of the north atlantic thermohaline

circulation for the 21st century assessed by observations. *Geophys. Res. Lett.*, 32(23).

Severijns, C. A. and Hazeleger, W. (2009). The efficient global primitive equation climate model SPEEDO. *Geoscientific Model Development Discussions*, 2:1115–1155.

Seydel, R. (1988). *From Equilibrium to Chaos - Practical Bifurcation and Stability Analysis*. Elsevier Science. 367pp.

Sijp, W. P., Bates, M., and England, M. H. (2006). Can isopycnal mixing control the stability of the thermohaline circulation in ocean climate models? *J. Climate*, 19:5637–5651.

Sijp, W. P. and England, M. H. (2009). The control of polar haloclines by along-isopycnal diffusion in climate models. *J. Climate*, 22:486–498.

Sleijpen, G. L. G. and Van der Vorst, H. A. (2000). A jacobi–davidson iteration method for linear eigenvalue problems. *SIAM Rev.*, 42(2):267–293.

Stammer, D. (2008). Response of the global ocean to Greenland and Antarctic ice melting. *J. Geophys. Res.*, 113(C6):C06022.

Stommel, H. (1961). Thermohaline convection with two stable regimes of flow. *Tellus*, 13(2):244–230.

Stouffer, R. J., Yin, J., Gregory, J. M., Dixon, K. W., Spelman, M. J., Hurlin, W., Weaver, A. J., Eby, M., Flato, G. M., Hasumi, H., Hu, A., Jungclaus, J. H., Kamenkovich, I. V., Levermann, A., Montoya, M., Murakami, S., Nawrath, S., Oka, A., Peltier, W. R., Robitaille, D. Y., Sokolov, A., Vettoretti, G., and Weber, S. L. (2006). Investigating the causes of the response of the thermohaline circulation to past and future climate changes. *J. Climate*, 19(8):1365–1387.

Thies, J., Wubs, F., and Dijkstra, H. A. (2009). Bifurcation analysis of 3D ocean flows using a parallel fully-implicit ocean model. *Ocean Model.*, 30(4):287–297.

Thual, O. and Mcwilliams, J. C. (1992). The catastrophe structure of thermohaline convection in a two-dimensional fluid model and a comparison with low-order box models. *Geophys. Astro. Fluid.*, 64(1):67–95.

Toggweiler, J. and Samuels, B. (1998). On the ocean's large scale circulation in the limit of no vertical mixing. *J. Phys. Oceanogr.*, 28:1832–1852.

Toggweiler, J. R. and Samuels, B. (1995). Effect of Drake Passage on the global thermohaline circulation. *Deep-Sea Res. (1 Oceanogr. Res. Pap.)*, 42:477–500.

Toole, J. M., Polzin, K. L., and Schmitt, R. W. (1994). Estimates of diapycnal mixing in the abyssal ocean. *Science*, 264:1120–1123.

Trenberth, K. E., Olson, J. G., and Large, W. G. (1989). A global ocean wind stress climatology based on ECMWF analyses. Technical report, National Center for Atmospheric Research, Boulder, CO, USA.

Tziperman, E. and Gildor, H. (2002). The stabilization of the thermohaline circulation by the temperature–precipitation feedback. *J. Phys. Oceanogr.*, 32(9):2707–2714.

Vallis, G. K. (2000). Large-scale circulation and production of stratification: Effects of wind, geometry, and diffusion. *J. Phys. Oceanogr.*, 30:933–954.

Van Aken, H. (2007). *The Oceanic Thermohaline Circulation: An Introduction*. Springer. 326pp.

Vellinga, M. (1997). *Bifurcations and dynamics of the ocean's thermohaline circulation*. PhD thesis,

Utrecht University. [Available from Institute for Marine and Atmospheric research Utrecht, Utrecht University, Princetonplein 5, 3584 CC Utrecht, The Netherlands].

Vellinga, M. (1998). Multiple equilibria in ocean models as a side effect of convective adjustment. *J. Phys. Oceanogr.*, 28(4):621–633.

Vellinga, M. and Wood, R. A. (2002). Global climatic impacts of a collapse of the atlantic thermohaline circulation. *Climatic Change*, 54(3):251–267.

Vellinga, M., Wood, R. A., and Gregory, J. M. (2002). Processes governing the recovery of a perturbed thermohaline circulation in hadcm3. *J. Climate*, 15(7):764–780.

Vellinga, M. and Wu, P. (2004). Low-latitude freshwater influence on centennial variability of the atlantic thermohaline circulation. *J. Climate*, 17(23):4498–4511.

Veronis, G. (1975). The role of models in tracer studies. In *Numerical Models of Ocean Circulation*, pages 133–146. Natl. Acad. Sci.

Von der Heydt, A. and Dijkstra, H. A. (2007). Localization of Multidecadal Variability. Part I: Cross-Equatorial Transport and Interbasin Exchange. *J. Phys. Oceanogr.*, 37:2401–2414.

Walin, G. (1982). On the relation between sea-surface heat flow and thermal circulation in the ocean. *Tellus*, 34(2):187–195.

Warren, B. A. (1983). Why is no deep water formed in the North Pacific? *J. Mar. Res.*, 41(2):327–347.

Weaver, A. J. and Sarachik, E. S. (1990). On the importance of vertical resolution in certain ocean general circulation models. *J. Phys. Oceanogr.*, 20:600–609.

Weijer, W., De Ruijter, W. P. M., Dijkstra, H. A., and Van Leeuwen, P. J. (1999). Impact of interbasin exchange on the Atlantic overturning circulation. *J. Phys. Oceanogr.*, 29(9):2266–2284.

Weijer, W. and Dijkstra, H. A. (2001). A bifurcation study of the three-dimensional thermohaline ocean circulation: The double hemispheric case. *J. Mar. Res.*, 59:599–631.

Weijer, W., Dijkstra, H. A., Öksüzoğlu, H., Wubs, F. W., and de Niet, A. C. (2003). A fully-implicit model of the global ocean circulation. *J. Comput. Phys.*, 192(2):452–470.

Weijer, W., Maltrud, M. E., Hecht, M. W., Dijkstra, H. A., and Kliphuis, M. A. (2012). Response of the atlantic ocean circulation to greenland ice sheet melting in a strongly-eddying ocean model. *Geophys. Res. Lett.*, 39(9).

Welander, P. (1959). An advective model of the ocean thermocline. *Tellus*, 11:309–318.

Welander, P. (1971). The thermocline problem. *Philos. T. R. Soc. Lond.*, 270A:415–421.

Welander, P. (1982). A simple heat-salt oscillator. *Dynam. Atmos. Oceans*, 6:233–242.

Wolfe, C. L. and Cessi, P. (2009). Overturning Circulation in an Eddy-Resolving Model: The Effect of the Pole-to-Pole Temperature Gradient. *J. Phys. Oceanogr.*, 39(1):125–142.

Wolfe, C. L. and Cessi, P. (2011). The Adiabatic Pole-to-Pole Overturning Circulation. *J. Phys. Oceanogr.*, 41(9):1795–1810.

Wright, D. G. and Stocker, T. F. (1992). Sensitivities of a zonally averaged global ocean circulation model. *J. Geophys. Res.*, 97(C8):12707–12730.

Wubs, F. W., de Niet, A. C., and Dijkstra, H. A. (2006). The performance of implicit ocean models on

b- and c-grids. *J. Comput. Phys.*, 211(1):210–228.

Wunsch, C. (2005). Thermohaline loops, Stommel box models, and the Sandström theorem. *Tellus A*, 57(1):84–99.

Yin, J., Schlesinger, M. E., Andronova, N. G., Malyshev, S., and Li, B. (2006). Is a shutdown of the thermohaline circulation irreversible? *J. Geophys. Res.*, 111.

Zhang, G. J., Ramanathan, V., and McPhaden, M. J. (1995). Convection-evaporation feedback in the equatorial pacific. *J. Climate*, 8(12):3040–3051.

Zhang, R. (2010). Latitudinal dependence of Atlantic meridional overturning circulation (AMOC) variations. *Geophys. Res. Lett.*, 37:L16703.

Zika, J. D., England, M. H., and Sijp, W. P. (2012). The Ocean Circulation in Thermohaline Coordinates. *J. Phys. Oceanogr.*, 42(5):708–724.

Publications

Den Toom, M., F. W. Wubs, and H. A. Dijkstra (2009). Corrigendum to "A tailored solver for bifurcation analysis of ocean-climate models" [J. Comput. Phys. 227 (2007) 654-679]. *J. Comput. Phys.*, 228(13):4962-4964.

Huisman, S. E., M. den Toom, H. A. Dijkstra, and S. S. Drijfhout (2010). An Indicator of the Multiple Equilibria Regime of the Atlantic Meridional Overturning Circulation. *J. Phys. Oceanogr.*, 40(3):551-567.

Den Toom, M., and H. A. Dijkstra (2011). Scaling of the strength of the meridional overturning with vertical diffusivity in an idealized global geometry. *Tellus A*, 63(2):354-370.

Den Toom, M., H. A. Dijkstra, and F. W. Wubs (2011). Spurious multiple equilibria introduced by convective adjustment. *Ocean Model.*, 38(1-2):126-137.

Den Toom, M., H. A. Dijkstra, A. A. Cimatoribus, and S. S. Drijfhout (2012). Effect of Atmospheric Feedbacks on the Stability of the Atlantic Meridional Overturning Circulation. *J. Climate*, 25: 4081-4096.

Cimatoribus, A. A., S. S. Drijfhout, M. den Toom, and H. A. Dijkstra (2012). Sensitivity of the Atlantic meridional overturning circulation to South Atlantic freshwater anomalies. *Clim. Dynam.*, 39(9-10):2291-2306.

Den Toom, M., H. A. Dijkstra, W. Weijer, M. W. Hecht, M. E. Maltrud, and E. van Sebille (2013). Sensitivity of a Strongly Eddying Global Ocean to North Atlantic Freshwater Perturbations. *J. Phys. Oceanogr.*, submitted.

Dankwoord

Henk, vanaf het eerste college Mechanica II wist ik dat ik van jou veel zou kunnen leren. Ik ben dankbaar dat jij je daar altijd voor hebt ingezet. Je droeg steeds uitdagende problemen aan en wees me op mogelijkheden om me verder te ontwikkelen. Ik ben blij dat ik veel vrijheid kreeg om mijn eigen pad te kiezen, maar dat je ingreep als mijn werk dreigde te verzanden in details. Ik zal je enthousiasme en eindeloze bron van nieuwe ideeën gaan missen.

Fred, met jou heb ik met veel plezier samengewerkt. Met name in het begin van mijn promotietraject heb ik dankbaar gebruik gemaakt van je kennis van numerieke wiskunde. De analyse in het artikel waarop hoofdstuk 3 gebaseerd is, is door jouw weloverwogen inbreng sterk verbeterd. Jonas, jou wil ik graag bedanken voor de hulp die kreeg bij het draaien van THCM. De ontvangst in Groningen door jullie beiden was altijd bijzonder hartelijk.

Sybren, jouw no-nonsense aanpak wetenschap was voor mij prettig ontnuchterend en dwong me goed na te denken over de betekenis van mijn resultaten. Andrea, you have been an inspiring colleague: you have a broad range of interests, work hard (but stay relaxed), and are always full of ideas. I would like to thank both of you for the successful collaboration within the "THC gang", which resulted in the article presented in chapter 4. Selma, jij hoorde ook een beetje bij deze "bende". Met veel plezier denk ik terug aan onze samenwerking, die in een mooie publicatie resulteerde. Ik heb je positieve energie gemist na je vertrek.

Wilbert, bedankt voor je oprechte interesse in mijn werk. Je bijdrage aan het manuscript dat ten grondslag ligt aan hoofdstuk 4, was bijzonder waardevol. Erik, ook jouw positief kritische commentaar heeft het verhaal verbeterd. Michael, zonder jouw technische ondersteuning hadden we nooit tot zo'n mooi resultaat kunnen komen. I also would like to thank Matthew Hecht and Mat Maltrud for help with the manuscript and for technical assistance.

Will, Anna, Leo en Huib, doordat jullie op wat grotere afstand stonden, leidden discussies menigmaal tot nieuwe inzichten. En Huib, bedankt voor het delen van je kritische commentaar na het lezen van dit proefschrift. Dave, thank you for your interest in my work. I am grateful for someone as knowledgeable as you to join the defence committee.

Werner, met jou heb ik - denk ik - het langst een kamer gedeeld. Ik heb genoten van je humor en maakte graag gebruik van je tips and tricks. Collega's en oud-collega's, dankzij jullie heb ik op het IMAU een geweldige tijd gehad.

Desiree en Willem, het was heerlijk dat ik zo af en toe het leven als onderzoeker met jullie kon beschouwen onder het genot van een glas wijn. Hoewel de frequentie af zal nemen nu de afstand is toegenomen, hoop ik dat we dit kunnen blijven doen. Marcel, met een goed Belgisch biertje kan het ook! Ik kijk met plezier terug op onze "collegiale werkoverleggen".

Pa, ma, ik ben dankbaar voor jullie onvoorwaardelijke steun. Lieve Agnes, van jou heb ik de afgelopen vijf jaar het meest geleerd. Het afronden van dit boekje is een mooie prestatie, maar echt trots ben ik op onze mooie dochter Naomi.

Curriculum vitae

Matthijs den Toom was born in Ridderkerk, the Netherlands, on 26 July 1984. In 2006, he received bachelor degrees in Earth Sciences and Physics from Utrecht University, where he continued to earn a master degree in Meteorology, Physical Oceanography and Climate in 2008. He then successfully applied for a grant within the Toptalent programme of the Netherlands Organisation for Scientific Research (NWO) to pursue a PhD in oceanography under supervision of prof. Henk Dijkstra. Matthijs completed his thesis in 2012 and subsequently worked as a post-doctoral researcher on the application of high performance computing in ocean modeling. As of 2013 he works as researcher at Deltares, where he is specializing in operational water management.